

SHAPE ESTIMATION OF TRANSPARENT OBJECTS BY USING  
POLARIZATION ANALYSES  
偏光解析による透明物体の形状計測

BY

DAISUKE MIYAZAKI  
宮崎 大輔

A DOCTORAL DISSERTATION

SUBMITTED TO  
THE GRADUATE SCHOOL OF  
THE UNIVERSITY OF TOKYO  
IN PARTIAL FULFILLMENT OF THE REQUIREMENTS  
FOR THE DEGREE OF DOCTOR OF INFORMATION  
SCIENCE AND TECHNOLOGY IN COMPUTER SCIENCE

THESIS SUPERVISOR: KATSUSHI IKEUCHI 池内 克史  
PROFESSOR OF COMPUTER SCIENCE

DECEMBER 2004



## ABSTRACT

Techniques developed in the field of computer graphics and virtual reality are applied in many situations today, with the result that methods of measuring three-dimensional shapes of real objects are seen to be more and more important. However, few methods are proposed to measure three-dimensional shapes of transparent objects such as those made of glass and acrylic. In this thesis, I propose three methods for estimating the surface shapes of transparent objects by using polarization analysis.

There is an ambiguity problem that results from using polarization data obtained by observing reflected light from one view. The first method resolves the ambiguity problem by the knowledge established in the research field of thermodynamics. The polarization analysis of reflected light in the visible light domain results in an ambiguity because two candidates for surface normal will be suggested. However, correct surface normal can be chosen by polarization analysis of thermal radiation in an infrared light domain.

The second method resolves the ambiguity by using theory established in the research field of differential geometry. This method resolves the ambiguity problem, first, by observing the reflected visible light of a transparent object from two different views, and second, by analyzing the difference of the degree of polarization at the geometrical invariant of the object's surface. I mathematically prove the validity of the algorithm that the geometrical invariant can be calculated from the polarization data even if the object's shape is not known.

The third method is an iterative method which uses the method called the polarization raytracing method. By giving an initial value for the surface shape of the transparent object, it estimates the true surface shape by updating the shape through minimizing the difference between the input polarization data and the rendered polarization data calculated by polarization raytracing.

Each method is evaluated and compared with similar methods used by other researchers. Future uses for these methods and future research work are also discussed.

## 論文要旨

コンピュータグラフィクスやバーチャルリアリティの技術が様々な場面で応用されるにしたがって、現実物体の3次元形状を計測する手法の重要性が高まってきた。しかしながら、ガラスやアクリルといった透明な物体の3次元形状を計測する手法はわずしか提案されていない。本論文では、偏光解析をもとに透明物体の表面形状を計測する三つの手法を提案する。

反射光を一つの方向から観測して得られた偏光データから透明物体の表面形状をもとめようとする曖昧性の問題が発生する。一つ目の手法では、熱力学の知識をもちいて曖昧性を除去した。可視領域における反射光の偏光解析では曖昧性が残り、表面法線として2つの候補が出てきてしまう。しかし、赤外領域における熱放射光の偏光解析により、正しい表面法線を選ぶことができる。

二つ目の手法では微分幾何学の知識をもちいて曖昧性を除去した。この手法は、透明物体の反射光を可視領域において2つの方向から観測し、物体表面上の幾何学的不変量における偏光度の変化を解析することにより、曖昧性を除去する。この際、物体形状が分からなくとも、偏光データから幾何学的不変量をもとまることを数学的に証明し、アルゴリズムの妥当性を示した。

三つ目の手法は、偏光レイトレーシング法と呼ばれる手法を用いた反復計算手法である。これは、透明物体の表面形状として、ある初期値が与えられたときに、入力となる偏光データと偏光レイトレーシング法でレンダリングした偏光データとの差を小さくするように形状を更新することにより真の形状をもとめる手法である。

本論文では、これらの手法の実験による評価と、他の研究者による手法との比較もおこなった。また、将来的な応用範囲と残された課題についても議論した。

## ACKNOWLEDGEMENTS

I offer my sincere thanks to my advisor, Katsushi Ikeuchi, for sharing his vast knowledge through discussions and for giving me much useful advice and guidance. I appreciate the pleasant environment provided by all the members of the Ikeuchi laboratory. This environment enabled me to work at the top of my potential. Especially, I thank Megumi Saito, Masataka Kagesawa, and Yoichi Sato for helping me with my research: they were generous with their knowledge. I also appreciated the discussions with laboratory members that helped my research proceed successfully. Discussions with Imari Sato and Robby T. Tan were particularly helpful in guiding my thinking. And I had very pleasant times and interesting conversations with laboratory members such as Kentaro Hashimoto and Toru Takahashi. Many other people in the laboratory made it a pleasant place to work. I enjoyed the life in the lab more than I could possibly have expected.

Finally, I want to thank my parents and my two younger brothers. I would never have experienced this wonderful opportunity without their support.

# CONTENTS

<b>1</b>	<b>Introduction</b>	<b>9</b>
1.1	Background . . . . .	9
1.2	Related Work . . . . .	10
1.2.1	Computer Vision . . . . .	10
1.2.2	Other Fields . . . . .	14
1.3	Thesis Overview . . . . .	15
<b>2</b>	<b>Polarization Analysis</b>	<b>17</b>
2.1	Fresnel Reflection . . . . .	17
2.1.1	POI Angle . . . . .	18
2.1.2	Incident Angle . . . . .	20
2.2	Polarization Raytracing . . . . .	23
2.2.1	Mueller Calculus . . . . .	23
2.2.2	Mueller Matrix . . . . .	24
2.2.3	Phase Shift . . . . .	26
2.2.4	Degree of Polarization . . . . .	26
2.2.5	Illumination Distribution . . . . .	27
<b>3</b>	<b>Shape Estimation of Transparent Objects by using Polarization Analysis and Thermal Radiation</b>	<b>28</b>
3.1	Introduction . . . . .	28
3.2	Assumptions . . . . .	28
3.3	Thermal Radiation . . . . .	30
3.4	Kirchhoff's Law . . . . .	32
3.5	Emitted Light . . . . .	33
3.6	Degree of Polarization of Thermal Radiation . . . . .	33
3.7	Summary . . . . .	35

<b>4</b>	<b>Shape Estimation of Transparent Objects by using Polarization Analysis and Differential Geometry</b>	<b>39</b>
4.1	Introduction . . . . .	39
4.2	Assumptions . . . . .	41
4.3	Brewster Segmentation . . . . .	43
4.4	Corresponding Point . . . . .	48
4.5	Difference of Degree of Polarization . . . . .	55
4.6	Summary . . . . .	57
<b>5</b>	<b>Shape Estimation of Transparent Objects by using Polarization Raytracing</b>	<b>60</b>
5.1	Introduction . . . . .	60
5.2	Assumptions . . . . .	61
5.3	Inverse Polarization Raytracing . . . . .	62
5.4	Summary . . . . .	65
<b>6</b>	<b>Evaluations</b>	<b>69</b>
6.1	Experimental Setup . . . . .	70
6.1.1	Experimental Setup of Visible Light . . . . .	70
6.1.2	Experimental Setup of Infrared Light . . . . .	72
6.2	Measurement . . . . .	72
6.2.1	Measurement of a Non-rotated Object in a Visible Light Domain . . . . .	72
6.2.2	Measurement of Thermal Radiation . . . . .	73
6.2.3	Measurement of Rotated Object . . . . .	73
6.2.4	Measurement of Multiple Internal Interreflection . . . . .	74
6.3	Experimental Results . . . . .	75
6.3.1	Experimental Results of Thermal Radiation Method . . . . .	75
6.3.2	Experimental Results of Differential Geometry Method . . . . .	77
6.3.3	Experimental Results of the Inverse Polarization Raytracing Method . . . . .	85
6.3.4	Comparison to Other Research . . . . .	106
6.4	Summary . . . . .	111
<b>7</b>	<b>Conclusion</b>	<b>116</b>
7.1	Summary . . . . .	116
7.2	Contribution . . . . .	117
7.3	Discussion . . . . .	119
7.3.1	Comparison between Three Proposed Methods . . . . .	119
7.3.2	Comparison with Other Methods . . . . .	121

7.4	Future Work . . . . .	123
<b>A</b>	<b>Theory of Optics</b>	<b>126</b>
A.1	Maxwell's Equations . . . . .	126
A.2	Electric Field and Magnetic Field . . . . .	129
A.3	Poynting Vector and Intensity . . . . .	130
A.4	Fresnel Formulae . . . . .	131
A.5	Derivation of Intensity Ratio . . . . .	136
A.6	Graph of Intensity Ratio . . . . .	136
<b>B</b>	<b>Gaussian Geometry</b>	<b>138</b>
B.1	Gaussian Mapping . . . . .	138
B.2	Gaussian Curvature . . . . .	141
B.3	Surface Classes . . . . .	142
B.4	Folding Point . . . . .	144
<b>C</b>	<b>Geometrical Properties in Brewster Segmentation</b>	<b>147</b>
C.1	Local and Global Folding Curve . . . . .	147
C.2	B-N Region . . . . .	147
C.3	Integral Curvature . . . . .	149
C.3.1	B-B Region . . . . .	150
C.3.2	Northern Hemisphere . . . . .	152
<b>D</b>	<b>English-Japanese Dictionary of Technical Terms</b>	<b>154</b>
	<b>Bibliography</b>	<b>162</b>

# LIST OF FIGURES

1.1	(a) Photograph of transparent heart-shaped glass and (b) the estimated shape of this object. . . . .	10
2.1	Reflection, refraction, and transmission. . . . .	19
2.2	Reflected and transmitted light observed by the camera. . . . .	20
2.3	Polar coordinates of surface normal. . . . .	21
2.4	Relation between the degree of polarization and the incident angle ( $n = 1.5$ ). . . . .	22
2.5	Calculation example of rotation Mueller matrix for reflection. . . . .	25
3.1	Energy distribution of blackbody. . . . .	31
3.2	DOP of (a)reflected light (visible light) ( $n = 1.5$ ), and (b)thermal radiation (infrared light) ( $n = 1.5$ ). . . . .	34
4.1	Coordinates of surface normal. . . . .	40
4.2	Gaussian mapping and regions. . . . .	45
4.3	A photograph of the bell-shaped object. . . . .	46
4.4	(a) A gray image of obtained degree of polarization of the bell-shaped object and (b) the result of Brewster segmentation. . . . .	46
4.5	Gaussian mapping of B-B region. . . . .	49
4.6	Gaussian mapping of bell-shaped surface. . . . .	49
4.7	(a) Folding curve and 4 points on object surface, (b) folding curve and 4 points on Gaussian sphere mapped from (a). . . . .	51
4.8	Object rotation. . . . .	52
4.9	Corresponding point. . . . .	53
4.10	Gaussian mapping of slide-shaped surface. . . . .	54
4.11	Graph of derivative of DOP ( $n = 1.5$ ). . . . .	56
6.1	Experimental setup for visible light. . . . .	71
6.2	Experimental setup for infrared light. . . . .	72

6.3	Error characteristics of the spherical object. . . . .	76
6.4	The resulting shape of the shellfish-shaped object. . . . .	77
6.5	Simulation result of the object No.1: (a) Boundaries of each region, (b) the resultant 3D-shape. . . . .	78
6.6	Simulation result of the object No.2: (a) Boundaries of each region, (b) the resultant 3D-shape. . . . .	79
6.7	Simulation result of object No.3: (a) Boundaries of each region, (b) the result 3D-shape. . . . .	79
6.8	The result of the real hemisphere object: (a) Circle for the theoretical shape and plotted dots for the obtained shape, (b) the resultant 3D-shape. . . . .	80
6.9	The graph of the DOP of the hemisphere object: (a) Raw data plotted, (b) modified data plotted. . . . .	81
6.10	(a) Photograph of transparent heart-shaped glass and (b) the obtained shape of this object. . . . .	82
6.11	A photograph of the bell-shaped object. . . . .	82
6.12	(a) A gray image of obtained degree of polarization of the bell-shaped object and (b) the result of Brewster segmentation. . . . .	83
6.13	A rendered image of the obtained shape of the bell-shaped object. . . . .	83
6.14	Rendering example of the estimated bell-shaped object. . . . .	84
6.15	The result of the real bell-shaped object. . . . .	84
6.16	Result of measuring a transparent mountain-shaped object: (a) Real image, (b) region segmentation result, and (c) and (d) rendered image. . . . .	86
6.17	DOP image; (a) rendered by polarization raytracing, (b) obtained from real object, and (c) rendered by assuming that the internal interreflection does not occur. . . . .	87
6.18	Simulation result of a triangle: (a)Initial state (true height times 1.8), (b)–(e)result after 10, 20, 30, 40 loops, respectively. . . . .	88
6.19	Simulation result of a triangle: (a)Initial state (true height times 1.6), (b)–(d)result after 10, 20, 30 loops, respectively. . . . .	88
6.20	Simulation result of a triangle: (a)Initial state (true height times 1.4), (b)–(d)result after 10, 20, 30 loops, respectively. . . . .	89
6.21	Simulation result of a triangle: (a)Initial state (true height times 1.2), (b)–(d)result after 10, 20, 30 loops, respectively. . . . .	89
6.22	Simulation result of a triangle: (a)Initial state (true height times 0.8), (b)–(d)result after 10, 20, 30 loops, respectively. . . . .	90

6.23	Simulation result of a triangle: (a)Initial state (true height times 0.6), (b)–(d)result after 10, 20, 30 loops, respectively. . . . .	91
6.24	Simulation result of a triangle: (a)Initial state (true height times 0.4), (b)–(d)result after 10, 20, 30 loops, respectively. . . . .	91
6.25	Simulation result of a triangle: (a)Initial state (true height times 0.2), (b)–(d)result after 10, 20, 30 loops, respectively. . . . .	92
6.26	Simulation result of a triangle: (a) Initial state (one of the solutions calculated by Saito’s method), (b)–(d) result after 10, 20, 30 loops, respectively. . . . .	92
6.27	Simulation result of triangle: (a) Initial state (one of the solution calculated by Saito’s method), (b)–(d) result after 10, 20, 30 loops, respectively. . . . .	93
6.28	Simulation result of a hexagon: (a) Initial state, (b)(c) result after 3, 30 loops, respectively. . . . .	93
6.29	Simulation result of bell shape: (a)Initial state, (b)–(l)result after 2, 4, . . . , 22 loops, respectively. . . . .	94
6.30	Trajectory of the light ray of concave object. . . . .	95
6.31	Simulation result of concave shape: (a) Initial state, (b)(c) result after 5, 20 loops, respectively. . . . .	96
6.32	3D hemispherical object result: (a) Initial state, (b) result after 10 loops. . . .	96
6.33	Estimation result: (a) Result of Saito’s method, (b)(c)(d) result after 5, 25, and 50 loops with proposed method, respectively. . . . .	97
6.34	Error for each loop. . . . .	98
6.35	DOP: (a) Real data, (b) computed data by polarization raytracing, (c) computed data by assuming only one reflection, (d) error between (a) and (b). . .	99
6.36	DOP and error: (a) DOP, (b) error; (1)–(5)result after 0, 2, 5, 10, 50 loops, respectively. . . . .	101
6.37	Estimated shape of bell-shaped acrylic object by using the inverse polarization raytracing method: (a) initial value, (b)(c)(d) estimated after 1, 5, and 20 loops, respectively. . . . .	102
6.38	Photograph of transparent jelly: (a) photograph of transparent jelly, (b)(c)(d) showing the situation where the touch sensor destroys the jelly and cannot measure the shape of the jelly. . . . .	103
6.39	True shape of jelly. . . . .	104
6.40	Estimated shape of jelly. . . . .	105
6.41	3D heart object result: (a) Initial state, (b) result after 10 loops, (c) raytracing image. . . . .	107

6.42	Results of Hata's method: (1)–(4)Result of hexagon shape, concave shape, bell shape, triangle shape, respectively, (a) initial shape, (b) result after 50 loops.	109
6.43	Comparison between Hata's method and proposed method: (1) Result of Hata's method, (2) result of proposed method; (a) Initial shape, (b)(c)(d) result after 1, 2, 50 loops, respectively.	110
A.1	Electric vector.	131
A.2	Magnetic vector.	132
A.3	Amplitude reflectivity and amplitude transmissivity.	135
A.4	Graphs of intensity ratios.	137
B.1	Gaussian mapping.	139
B.2	Three examples of Gaussian mapping.	140
B.3	Normal section.	141
B.4	Surfaces classified by Gaussian curvature.	143
B.5	Gaussian mapping of some patches.	145
C.1	Gaussian mapping of bell-shaped surface.	148
C.2	The integration of the outer curve calculated in a counterclockwise trajectory, and the integral of the inner curve calculated in a clockwise trajectory: (a) a B-B region enclosed by two Brewster curves that are also ovals and level curves; (b) a B-B region enclosed by two Brewster curves that are also level curves and are in similarity.	150
C.3	Viewing vector $\mathbf{v}$ , curvature(acceleration) vector $\mathbf{k}$ , normal curvature vector $\mathbf{k}_n$ , geodesic curvature vector $\mathbf{k}_g$ , and Brewster angle $\theta_B$ .	152

# LIST OF TABLES

7.1	Advantage and disadvantage of three methods. . . . .	120
7.2	Comparison between other methods. . . . .	124
B.1	Surface classes and curvatures . . . . .	144

# CHAPTER 1

## INTRODUCTION

### 1.1 Background

In the field of computer vision, few methods have been proposed for estimating the shape of transparent objects, because of the difficulty of dealing with the internal interreflection, which may be defined as reciprocal reflection between two reflecting surfaces. Due to this phenomenon, the light not only reflects at the surface of the transparent object but also transmits into the object and causes multiple reflections and transmissions inside it. This thesis presents three methods for estimating the surface shape of transparent objects by analyzing the polarization of transparent objects. Figure 1.1(a) is a picture of a heart-shaped piece of glass and Figure 1.1(b) is the shape of the object estimated by one of my methods.

Recently, techniques for 3D modeling of objects through observation have been extensively investigated. Such 3D modeling has a wide range of applications, including virtual reality and object recognition. Geometry is one of the most important aspects of 3D modeling since realistic images can be generated from geometrical models obtained by measuring the shape of an object.

Many techniques to measure the shape of an object have been developed in the field of optical engineering. These techniques can be classified into two categories: point and surface types. A point type method, such as a laser range sensor, measures the shape of an object by projecting a spotlight, often a laser beam, over the object's surface, and by measuring the returned timing or the returned direction. A surface method, such as moiré topography, determines the shape of an object by projecting a planar light and measuring the interference of the light with the surface.

The computer vision community has extensively developed additional techniques [Hor86, BB82, IS01]. Shape-from-shading, for example, analyzes shading information in an image



Figure 1.1: (a) Photograph of transparent heart-shaped glass and (b) the estimated shape of this object.

---

with a reflectance map in order to relate image brightness to surface normals. Photometric stereo obtains information from three images, taken from the same position, under three different illumination conditions. Binocular stereo and motion analysis use image differences in a series of images taken from different positions.

Most of these methods are, however, designed to obtain the shape of opaque surfaces and are based on analysis of the diffuse (body) reflection component of an object's surface. Models of transparent objects, which have only specular (surface) reflection, cannot be created using these techniques. Few extant methods attempt to determine the shapes of objects through specular reflection.

## 1.2 Related Work

### 1.2.1 Computer Vision

#### Specularity

With regard to specular reflection, Ikeuchi [Ike81] proposed to determine the reflectance of a metal surface using photometric stereo. When exposed to three extended light sources, a metal surface generates different illumination distributions over the surface. The application of the photometric stereo method to these illumination distributions allows the shape of a metal surface to be determined. Sanderson et al. [SWN88] and Nayar et al. [NSWS90] determined the surface normal of metallic objects by illuminating the object by many tiny light sources. Nayar et al. [NIK90] extended the method by using continuous illumination distribution, re-

ferred to as a photometric sampler. Their method determines not only surface shape but also surface reflectance parameters. Sato et al. [SI94] analyzed color images in a similar setting, and determined the shape and reflectance of shiny objects. Hata [Hat92] also proposed a similar method; however, he used a colorful continuous illumination distribution, using the hue as a clue for determining the shape of metallic objects. Nakano et al. [NWK88] solved the interreflection problem of projecting a laser beam and determined the shape of shiny objects using shape from a structured light method. Recently, Park and Kak [PK04] also determined the shape of shiny objects using shape from a structured light method by solving the interreflection problem with a different approach. Oren and Nayar [ON97] proposed a method to determine metallic surface shape by analyzing specular reflections obtained by moving the camera. Zheng et al. [ZFA97] estimated the shape of a metallic object by analyzing the EPI of highlights. Bhat and Nayar [BN98] used trinocular stereo for determining the shape of shiny objects.

These methods, however, only measure the shape of opaque specular objects, not transparent objects.

### **Polarization**

Polarization is a phenomenon in which the light oscillates in one direction. Much research has been done in various fields of science and industry [Shu62]. Some researchers discovered that some of the insects such as bees can detect the polarization state of the light. Polarization is used in polarizing sunglasses, 3D stereoscopic glasses, liquid crystal displays, and so on.

By analyzing the polarization phenomenon, Schechner et al. [SSK00] decomposed the reflected scene and the transmitted scene that was originally combined with a glass plate. Wolff and Boulton [WB91] separated the specular reflection component and the diffuse reflection component of the image by polarization analysis. Nayar et al. [NFB97] improved this method by combining the polarization analysis and the color analysis. Also, Lin and Lee [LL97] proposed a similar method, observing from two views. Umeyama and Godin [UG04] separated the two components by polarization analysis and ICA (independent component analysis). In the field of computer graphics, polarizing filter is also used to separate the specular reflection component and the diffuse reflection component to estimate the parameters of BRDF (Bidirectional Reflectance Distribution Function) [Tak02, HNNI02, DHT+00, TOS+03]. Schechner et al. [SNN03] used polarization to improve the quality of the image taken in hazy weather. Clark et al. [CTW97] and Wallace et al. [WLTC99] improved the laser range finder by polarization analysis to estimate the shape of opaque objects. Wolff, Boulton, and Chen [Wol90, WB91, CW98] used polarization analysis to classify material into metal or dielectric. Sandus [San65], Nicodemus [Nic65, Nic70], Jordan et al. [JL94, JLJ96] and Wolff et al.

[WLT98] analyzed the degree of polarization in the infrared wavelengths. There are roughly four kinds of methods to calculate the polarization state of the light: (1) a simple calculation method using Fresnel formulae [BW59, Shu62, Hec02], (2) a method using coherence matrix [BW59], (3) Mueller calculus [Shu62, Hec02], and (4) Jones calculus [Shu62, Hec02]. Some commercial raytracing software [Lig, ZEM, Opt] simulates the polarization state by using these methods. Kagalwala and Kanade [KK98] used a method called Jones calculus to simulate the structure of the Nomarski DIC (differential interference contrast) microscope. Koshikawa and Shirai [KS87] used a method called Mueller calculus to estimate the surface normal of specular polyhedrons. Wolff and Kurlander [WK90] extended the method using coherence matrix, while Chipman [Chi95], Gu and Yeh [GY93] extended the Jones calculus method. Wolff et al. [WMPA97], Fujikake et al. [FTA+98], Harnett and Craighead [HC02], and Furuuchi Chemical Corporation [Fur] developed a polarization camera with liquid crystal [WMPA97, FTA+98, HC02] or PLZT [Fur], which is controllable from a computer.

Recently, research to estimate the shape of the object by using polarization has increased. Kosikawa and Shirai [KS87] proposed to use the degree of polarization, employing circularly polarized light sources to determine the surface normal of specular polyhedrons. They used Mueller calculus to calculate the polarization state of the light. Wolff and Boulton [WB91] indicated that the surface normal of the object surface is constrained by analyzing the polarization of the object, and estimated the surface normal of a planer glass from two views. Rahmann [Rah99] estimated the orientation of a flat object and the position of the light source by polarization analysis of single view. Rahmann also [Rah00] addressed the potential of recovering the shape of specular surfaces from polarization. Later, Rahmann and Canterakis [RC01] estimated the shape of specular objects from two or more views. Also, they proved that the quadratic shape of specular objects can be estimated from two views [Rah03]. Drbohlav and Šára [DS01] estimated the shape of diffuse objects by combining the polarization analysis and the photometric stereo. Miyazaki et al. [MTHI03] estimated the shape and reflectance of specular objects and the illuminant direction from one view. Saito et al. [SSIK99] employed the analysis of the degree of polarization and developed a method with which the surface of a transparent object could be determined; however, the degree of polarization provided two candidates of surface normal, and they did not solve this ambiguity. Unfortunately, because these methods do not consider internal interreflections, they do not provide sufficient accuracy for estimating the shape of transparent objects.

## **Transparency**

Many methods have been developed to deal with transparent objects.

An inverse problem of alpha blending is called alpha estimation or matting [SB96, MTKO02,

SG98]. Recently, a method called environment matting [ZWCS99, CZH+00, HS01, MPZ+02, WFZ02, PD03] has been developed for graphics applications of rendering transparent objects. The method first surrounds a transparent object with multiple light sources such as CRT screens, and observes the object through changing the illumination distribution. Next, the method observes which pixel is changed and how it is changed when varying amounts of light are used to illuminate the object from varying directions. From this information, an image of a transparent object under any kind of illumination distribution can be rendered.

When one watches at a planar glass such as a window, one can see both the reflection of the foreground scene and the transmission of the background scene. Some researchers attempted to separate the two scenes by observing the composite image of the two scenes. Farid and Adelson [FA99] separated the two scenes by ICA (independent component analysis). Schechner and Shamir [SSK00] used the polarization analysis to this reflection separation problem. Schechner et al. [SKB00] also solved the reflection separation problem by changing the focus of the camera. Szeliski et al. [SAA00] solved the problem by analyzing the motion of the scene. Later, Levin et al. [LZW04] used a database to separate the reflection.

Nikolaev and Nayar [NN96] developed a transparent robot arm, which helps the robot to recognize what he/she is grasping. Osadchy et al. [OJR03] used the specularly of transparent objects for object recognition.

These methods, however, do not totally provide information about the shape of the transparent object.

Some methods that estimate the 3D shape of transparent objects have been proposed. Murase [Mur92] estimated the shape of a water surface by analyzing the undulation of the water surface. Hata et al. [HSKK96] estimated the surface shape of transparent objects by analyzing the deformation of the light projected onto the transparent objects. Ohara et al. [OMOT03] estimated the depth of the edge of a transparent object by using shape-from-focus. Ben-Ezra and Nayar [BN03] estimated the parameterized surface shape of transparent objects by using structure-from-motion. Saito et al. [SSIK99] employed the analysis of the degree of polarization and developed a method with which the surface of a transparent object could be determined; however, the degree of polarization provided two candidates of surface normal, and they did not solve this ambiguity. None of these methods are capable of estimating arbitrary shapes of transparent objects.

## 1.2.2 Other Fields

### Computer Graphics

In the field of computer graphics, a method called raytracing has been developed for rendering a realistic image of transparent objects. However, only a few people take interest in the inverse problem of raytracing.

In the field of acoustics, people use the raytracing method to calculate the sound received in the room where the sound source is set in the room. Some researchers estimate the position of a sound source by solving the inverse problem of raytracing from detecting the sound that came from the sound source or came by reflecting sound on the wall in the room.

However, few researchers developed a method to estimate the shape of transparent objects by solving the inverse problem of raytracing method.

### Optics

SEM (scanning electron microscopy) and the optical probe method estimate the shape of the object very precisely. However, there are problems: the device is expensive, it can only measure planar or near-planar objects, and the measurement is not realtime. Autocollimation also has problems: can only measure near-planar objects, and it cannot measure realtime. And interferometry has similar problems: it cannot measure the shape of smooth transparent object, and it can only measure near-planar object. These methods do not consider the internal interreflection of a transparent object.

### Haptic Devices

Some devices that measure the shape of an object by touching it have been developed by some industrial companies; however, these devices are expensive and only concentrate on small and nearly flat objects. In the field of robotics, some researchers use a robot arm for measuring a non-flat object by touch sensors [AM90, IJ04]. These researchers are trying hard not to break the target object and to decrease the number of touching points at the object surface to reduce the measuring time. To reduce the measuring time, the robot must touch effective points such as the inflection of the curved surface or the end of the principal axes of ellipsoid. Humans effectively determine such interest points by observing the object; hence, observing the object is very important and helps the robot to determine where to touch. Therefore, a method for estimating the shape of the object from observation is required for haptic measurement devices.

In addition, there is a problem in haptic devices that they cannot estimate the shape of the object in realtime.

## Ultrasonic Waves

There are many devices to measure the shape of objects by using ultrasonic waves. However, these devices are sensitive to the interreflections between the target object and the surrounding equipments; hence, they do not provide a precise enough shape of the object.

## Painting

Painting the transparent object in order to make it opaque makes the shape measurement possible by existing methods that measure the shape of opaque objects. However, it narrows the application field such as measuring the shape of a water surface, measuring the parts of industrial products, measuring important cultural assets, measuring a jellyfish, and so on.

## 1.3 Thesis Overview

Saito et al. [SSIK99] employed analysis of the degree of polarization and developed a method with which to measure the surface of a transparent object. Employing an extended light source originally developed by Nayar et al. [NIK90], they illuminated a transparent object and were able to obtain specular reflection components over the entire visible surface. Then, by measuring the DOP (degree of polarization), they determined surface normals. Unfortunately, however, the DOP provides two solutions corresponding to one DOP. Therefore, the method can be applied to measuring a limited class of objects or to surface inspection where rough surface normal is predetermined; it cannot be applied to a general class of objects.

In this thesis, I propose to disambiguate these two solutions by two methods. One is to introduce the DOP of the thermal radiation, and the other is to introduce the polarization analysis by considering the differential-geometrical property of the object's surface. But Saito's method and these two methods do not consider the effect of internal interreflection. Hence, I propose another method to estimate the surface shape of transparent objects more precisely by considering both reflection and transmission.

The first method [MSSI02] (Chapter 3), using thermal radiation, solves the ambiguity problem of Saito's method and obtains a unique surface normal of a transparent object. This method first obtains the DOP of the reflected light in the visible light domain, which was likewise obtained in Saito's method. One DOP measured corresponds to two surface normals. The DOP of thermal radiation in the infrared light domain provides a single surface normal to one DOP. Therefore, by simultaneously measuring the DOP in the infrared light domain, the surface normal can be uniquely determined. The measurement in the infrared light domain cannot be used directly because the DOP is relatively low in some areas, and it is therefore better to use this measurement solely for judgment purposes.

The second method [MKI04] (Chapter 4), using differential geometry, solves the ambiguity problem of Saito's method and obtains a unique surface normal of transparent object, which is also done in the first method. This method obtains two sets of polarization data from two different views, as is done in the binocular stereo method. I did not set two cameras to capture these views. For the purpose of experimental setup convenience, the camera was fixed and the object is tilted only slightly to obtain two sets of data from two different views. This method first obtains the DOP, which was likewise obtained in Saito's method. One DOP measured corresponds to two surface normals. The DOP of a novel view disambiguates this problem. By comparing the DOP at the same surface point (corresponding point) of each piece of polarization data, the unique surface normal is determined.

The third method [MI05] (Chapter 5), using polarization raytracing, solves the internal interreflection problem of Saito's method, the first method, and the second method. This method computes a more accurate shape by considering both reflection and transmission of the light ray. The internal interreflection of transparent objects is simulated by using a method called polarization raytracing. Polarization raytracing is a combination of conventional raytracing, which calculates the trajectory of light rays, and Mueller calculus, which calculates the polarization state of the light. First, I set an initial value of the shape of the transparent object. Then, the method minimizes the difference between the input polarization data and the rendered polarization data calculated by polarization raytracing, by changing the shape. Finally, after the iterative computation is converged, the shape of the object is obtained. The surface shape of the transparent object is estimated more precisely than the other two methods.

The thesis is organized as follows. In Chapter 2, I present the background theory of polarization and then develop an underlying algorithm to determine surface normal up to two possible incident angles, using polarization. I describe the first method in Chapter 3, a method that obtains surface shape using the degree of polarization in both visible and infrared light domains. I describe the second method in Chapter 4, a method for disambiguating the possibility in the incident angle by rotating the object. The purpose of this method is the same as that of the first method, though the approach is different. I describe the third method in Chapter 5, a method which solves the inverse problem of the polarization raytracing method. This method improves the quality of the measurement result compared to the first method and the second method, by considering the multiple reflections occurring inside the transparent object. In Chapter 6, I describe the apparatus of these three methods and the experimental results of them. Chapter 7 concludes the thesis.

## CHAPTER 2

# POLARIZATION ANALYSIS

### 2.1 Fresnel Reflection

Light reflected from the surface of most types of objects can be separated into two major components: surface reflection and body reflection. Incident light partially reflects immediately from the surface and partially penetrates the object. The light that penetrates an opaque object randomly reflects at pigments inside the object and is emitted into the air. The light that immediately reflects into the air is called the surface reflection and the light that penetrates and is then reflected back into the air is called the body reflection [TS67, Sha85]. Since I focus on transparent objects in this thesis, I will deal only with surface reflection.

In this section, I present a brief overview of the basic equation of reflection and refraction [BW59, Hec02] (Appendix A). In Figure 2.1, let us consider the case in which a light hits the interface surface between two materials, the refractive indices of which are denoted as  $n_1$  and  $n_2$ , respectively. One part of the light is reflected from the interface surface, while another part penetrates the surface and is refracted when it enters the second material. Because I assume that both materials are transparent, I can ignore the component to be absorbed. The plane including the surface normal and the incident light ray is called the POI (plane of incidence). I denote the incident light, the reflected light, and the transmitted light as the subscripts  $a$ ,  $r$ , and  $t$ , respectively, and identify the parallel and perpendicular components to the POI as  $\parallel$  and  $\perp$ , respectively. The incident, reflecting, and transmitting angles are defined as  $\theta_1$ ,  $\theta'_1$ , and  $\theta_2$ , respectively, as shown in Figure 2.1. Since I focus on optically smooth transparent objects, the incident angle and the reflecting angle will be the same  $\theta_1 = \theta'_1$ .  $\theta_1$  and  $\theta_2$  is related by Snell's law,

$$n_1 \sin \theta_1 = n_2 \sin \theta_2 . \quad (2.1)$$

I define the parallel and perpendicular intensity reflectivities,  $R_{\parallel}$  and  $R_{\perp}$ , respectively, as

$$\begin{aligned} R_{\parallel} &= \frac{I_{r\parallel}}{I_{a\parallel}} = \frac{\tan^2(\theta_1 - \theta_2)}{\tan^2(\theta_1 + \theta_2)} \\ R_{\perp} &= \frac{I_{r\perp}}{I_{a\perp}} = \frac{\sin^2(\theta_1 - \theta_2)}{\sin^2(\theta_1 + \theta_2)} \end{aligned} \quad (2.2)$$

where  $I_{a\parallel}$  is the component parallel to the POI of the incident light, and  $I_{r\parallel}$  is that of the reflected light.  $I_{a\perp}$  is the component perpendicular to the POI of the incident light, and  $I_{r\perp}$  is that of the reflected light. From the above equation, an incident angle to make  $R_{\parallel} = 0$  can be obtained. This incident angle is referred to as the Brewster angle,  $\theta_B$ . The Brewster angle is obtained by substituting  $\theta_1 + \theta_2 = \pi/2$  (namely,  $R_{\parallel} = 0$ ) into Snell's equation as

$$\tan \theta_B = \frac{n_2}{n_1}. \quad (2.3)$$

Generally, natural light is unpolarized and becomes polarized once it goes through a polarization material or it is reflected from a surface, and I am interested in measuring the degree of polarization of reflected light. The interfaces of smooth, transparent objects cause less diffuse reflection or absorption as opposed to those of opaque objects, and the incident and reflecting angles are the same. Therefore, once the reflecting angle and the POI angle are known, I can determine the surface normal with respect to the viewer, as shown in Figure 2.2. Here, the plane of incidence is the one on which the light source and surface normal lie. Since I analyze only smooth, transparent objects, the viewer vector is included in the plane of incidence. I will denote the POI angle and the reflecting angle as  $\psi$  and  $\theta$ , respectively, and determine these two angles by using the degree of polarization of reflected light.

### 2.1.1 POI Angle

As shown in Equation (2.2), the intensity of the reflected light varies depending on the direction of oscillation in the plane of oscillation; therefore, a difference can be observed when the polarization filter is rotated in front of a CCD (charge-coupled device) camera. The variance is described as a sinusoidal function of rotation angles. I will denote the maximum and minimum brightness in the observed intensities as  $I_{\max}$  and  $I_{\min}$ . Given that the sum of the maximum and minimum brightness is the total brightness of the reflected light  $I_{\text{spec}}$ ,

$$I_{\max} = \frac{R_{\perp}}{R_{\parallel} + R_{\perp}} I_{\text{spec}}, \quad I_{\min} = \frac{R_{\parallel}}{R_{\parallel} + R_{\perp}} I_{\text{spec}}. \quad (2.4)$$

By this equation, the direction parallel to the plane of incidence provides the minimum brightness  $I_{\min}$ . Namely, by measuring the angle where the minimum brightness is observed,

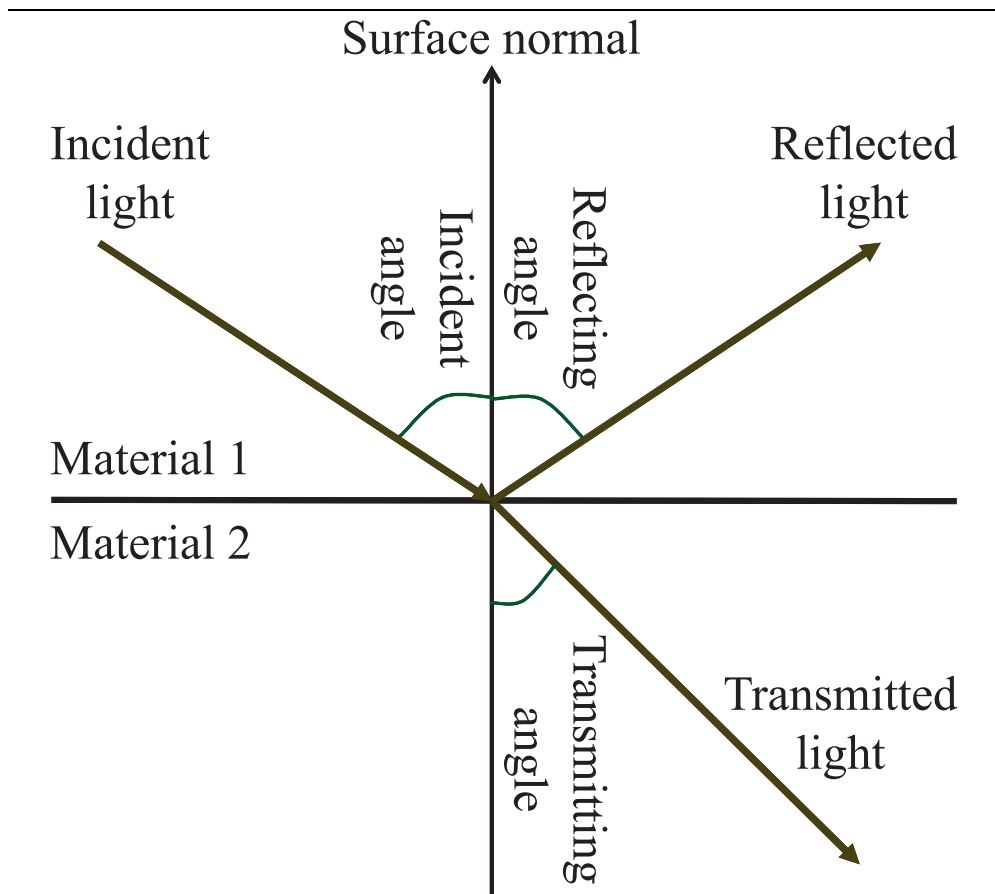


Figure 2.1: Reflection, refraction, and transmission.

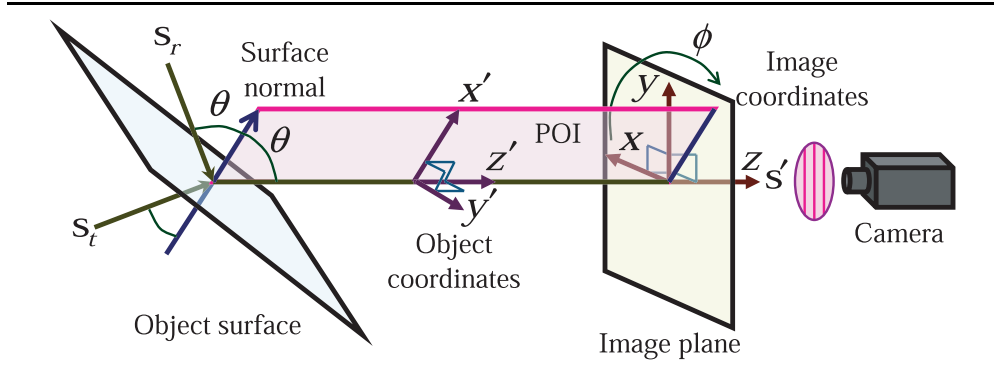


Figure 2.2: Reflected and transmitted light observed by the camera.

I can determine the POI angle  $\psi$  ( $0 \leq \psi < 2\pi$ ). The POI angle is determined as the angle between  $+x$ -axis and POI, from  $+x$ -axis to  $+y$ -axis, as shown in Figure 2.2. There are two possible POI angles,  $\psi_{LO}$  and  $\psi_{HI}$ , which are definable as  $\psi_{HI} = \psi_{LO} + \pi$ , where  $0 \leq \psi_{LO} < \pi$  and  $\pi \leq \psi_{HI} < 2\pi$ . Surface normal can be represented in polar coordinates with zenith angle  $\theta$  and azimuth angle  $\phi$  as in Figure 2.3. Azimuth angle  $\phi$  equals to  $\psi_{LO}$  or  $\psi_{HI}$ .

Since I assume that the object is a closed, smooth object, I can determine the surface normal at the occluding boundary; the surface normal heads for the outside of the shape of the projection of the object at the occluding boundary. By using the  $\phi$  at the occluding boundary as an initial condition, I propagate the constraint of  $\phi$  throughout the surface and, finally, determine the value of  $\phi$ , whether it is  $\phi = \psi_{LO}$  or  $\phi = \psi_{HI}$ , over the entire surface, assuming that all local parts of the surface are not concave in the direction of the camera.

### 2.1.2 Incident Angle

The definition of the DOP (degree of polarization) is,

$$\rho = \frac{I_{\max} - I_{\min}}{I_{\max} + I_{\min}}. \quad (2.5)$$

The degree of polarization is 0 when the light is unpolarized, whereas it is 1 when the light is linearly polarized. The linearly polarized light is observed when the incident angle and the reflecting angle are at the Brewster angle.

By substituting Equation (2.4) and (2.2) into Equation (2.5) with Snell's law, I can repre-

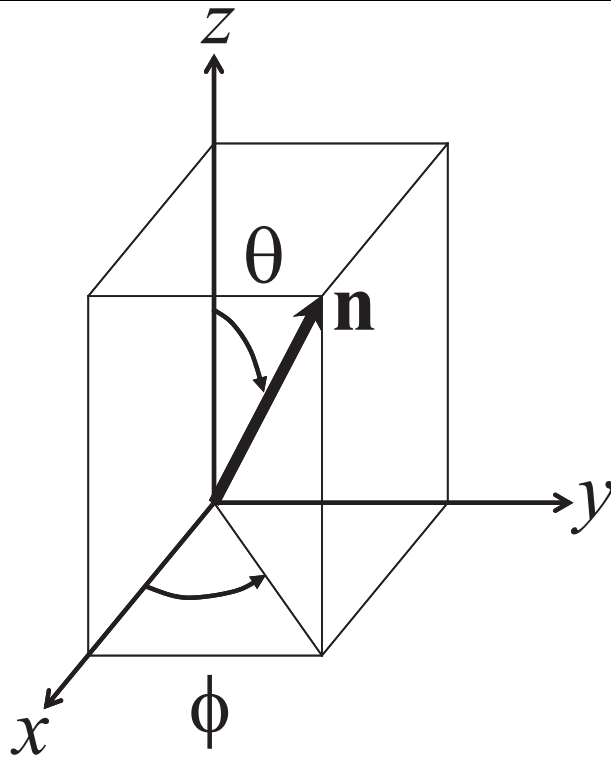


Figure 2.3: Polar coordinates of surface normal.

---

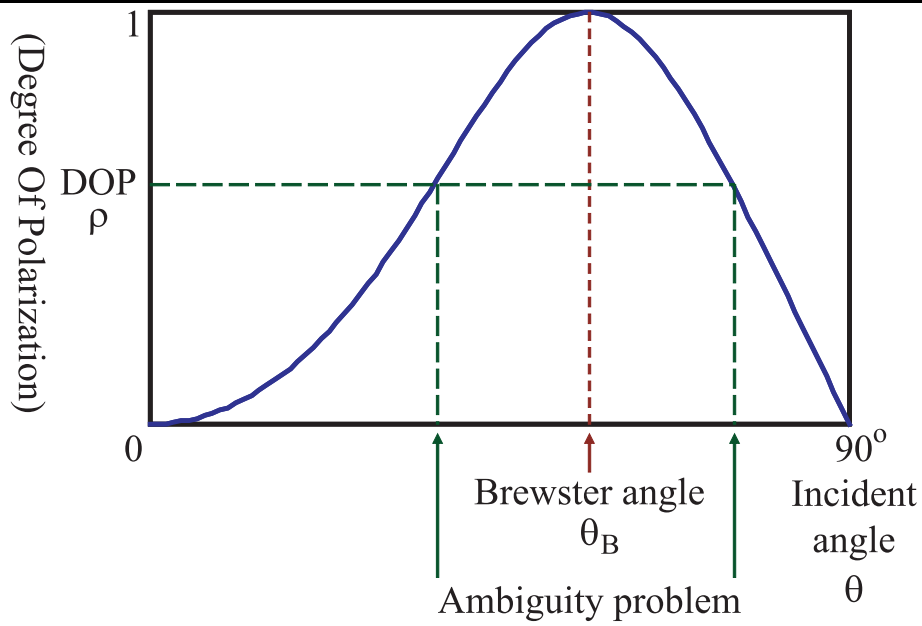


Figure 2.4: Relation between the degree of polarization and the incident angle ( $n = 1.5$ ).

sent the degree of polarization  $\rho$  as

$$\rho = \frac{2 \sin^2 \theta \sqrt{n^2 - \sin^2 \theta - n^2 \sin^2 \theta + \sin^4 \theta}}{n^2 - \sin^2 \theta - n^2 \sin^2 \theta + 2 \sin^4 \theta}. \quad (2.6)$$

The degree of polarization is a function of the refractive index  $n (= n_2/n_1)$  and the incident angle  $\theta (= \theta_1)$  ( $0 \leq \theta \leq \pi/2$ ). Therefore, by obtaining the degree of polarization from the data, I can determine the incident angle  $\theta$ , given the refractive index  $n$ .

Figure 2.4 shows the relationship between the degree of polarization and the incident angle. Here, the horizontal and vertical axes denote the incident angle and the degree of polarization, respectively. I can obtain the incident angle from the observed degree of polarization even if I do not know the intensity of the light source. The function has an extremum at the Brewster angle. From this function, an observed degree of polarization provides two possible incident angles, except at the Brewster angle. It is necessary to have a method to resolve this ambiguity. In this thesis, I propose to solve this problem by two methods, one by considering the polarization of far infrared light (Chapter 3), and the other by comparing two sets of polarization data through rotating the object (Chapter 4).

## 2.2 Polarization Raytracing

### 2.2.1 Mueller Calculus

A conventional raytracing method renders a 2D image from 3D geometrical shape data of transparent objects or other kind of objects. In this thesis, I call the raytracing method which considers the polarization effect the polarization raytracing method.

The algorithm of the polarization raytracing method can be divided into two parts. For the first part, the calculation of the propagation of the ray, I employ the same algorithm used in the conventional raytracing method. For the second part, the calculation of the polarization state of the light, the direct implementation of Section 2.1 is possible; however, there are more effective methods to calculate the polarization: Mueller calculus [Shu62, Hec02], Jones calculus [Shu62, Hec02], and the method that uses the coherence matrix [BW59, Hec02]. In this thesis, I employ Mueller calculus, because of its simplicity of description, along with its ease of understanding and implementation. These three methods have almost identical functions; thus, all discussions presented in this thesis are also applicable to other calculi. I will present a brief overview of Mueller calculus in the following pages; however, I will leave the details to the literature [Shu62].

In Mueller calculus, the polarization state of the light is represented as Stokes vector  $\mathbf{s} = (s_0, s_1, s_2, s_3)^T$ . The Stokes vector is a 4D vector. Its first component  $s_0$  represents the intensity of the light; its second component  $s_1$  represents the horizontal power of the linear polarization; its third component  $s_2$  represents the  $+45^\circ$ -oblique power of the linear polarization; and its fourth component  $s_3$  represents the power of the right circular polarization. The Mueller matrix  $\mathbf{M}$ , which is  $4 \times 4$  matrix, represents how the object changes the polarization state of the light.

The operation of Mueller calculus is a linear operation. The following is the example of Mueller calculus. Suppose the light that has a Stokes vector  $\mathbf{s}$  reflects or transmits at a certain object. Mueller matrix  $\mathbf{M}$  represents how the object changes the polarization state of the light. Then, the resultant Stokes vector  $\mathbf{s}'$  of the light after reflection/transmission is calculated as  $\mathbf{s}' = \mathbf{M}\mathbf{s}$ . Next, suppose the light with Stokes vector  $\mathbf{s}$  reflects/transmits successively at object 1 and 2. Here, Mueller matrices  $\mathbf{M}_1$  and  $\mathbf{M}_2$  represent how the light changes at object 1 and 2, respectively. Then, the resultant Stokes vector  $\mathbf{s}'$  is calculated as  $\mathbf{s}' = \mathbf{M}_2\mathbf{M}_1\mathbf{s}$ . The Stokes vector  $\mathbf{s}'$  of the light, which is a composition of the light with Stokes vector  $\mathbf{s}_1$  and the light with Stokes vector  $\mathbf{s}_2$ , is calculated as  $\mathbf{s}' = \mathbf{s}_1 + \mathbf{s}_2$ .

## 2.2.2 Mueller Matrix

First, I introduce a method for calculating the polarization state of the reflected light and the transmitted light when the POI angle is  $0^\circ$ ; after that, I introduce a method for the case when the POI angle is not  $0^\circ$ .

Mueller Matrices of reflection  $\mathbf{R}$  and transmission  $\mathbf{T}$  when the POI angle is  $0^\circ$  are represented as follows:

$$\mathbf{R} = \begin{pmatrix} (R_{\parallel} + R_{\perp})/2 & (R_{\parallel} - R_{\perp})/2 & 0 & 0 \\ (R_{\parallel} - R_{\perp})/2 & (R_{\parallel} + R_{\perp})/2 & 0 & 0 \\ 0 & 0 & \sqrt{R_{\parallel}R_{\perp}} & 0 \\ 0 & 0 & 0 & \sqrt{R_{\parallel}R_{\perp}} \end{pmatrix} \quad (2.7)$$

$$\mathbf{T} = \begin{pmatrix} (T_{\parallel} + T_{\perp})/2 & (T_{\parallel} - T_{\perp})/2 & 0 & 0 \\ (T_{\parallel} - T_{\perp})/2 & (T_{\parallel} + T_{\perp})/2 & 0 & 0 \\ 0 & 0 & \sqrt{T_{\parallel}T_{\perp}} & 0 \\ 0 & 0 & 0 & \sqrt{T_{\parallel}T_{\perp}} \end{pmatrix}. \quad (2.8)$$

Therefore, if I have a light ray with the Stokes vector  $\mathbf{s}$  impinged on an object, then the Stokes vector of reflected light will be  $\mathbf{R}\mathbf{s}$ , when the POI angle is  $0^\circ$ . The same thing can also be said of the transmitted light.

Figure 2.2 illustrates the case when the POI angle is  $\psi$ . Figure 2.5 explains how to calculate the reflected light for this case. I always multiply the reflection matrix  $\mathbf{R}$  by the Stokes vector whose POI angle is transformed to  $0^\circ$ . So, I first rotate the incident Stokes vector  $\mathbf{s}$  with the angle  $-\psi$ . After that, I multiply  $\mathbf{R}$  by the transformed Stokes vector. Finally, the Stokes vector is rotated again with the angle  $\psi$  in order to restore the original coordinates. The resulting Stokes vector  $\mathbf{s}'$  is as follows:

$$\mathbf{s}' = \mathbf{C}(\psi)\mathbf{R}\mathbf{C}(-\psi)\mathbf{s}, \quad (2.9)$$

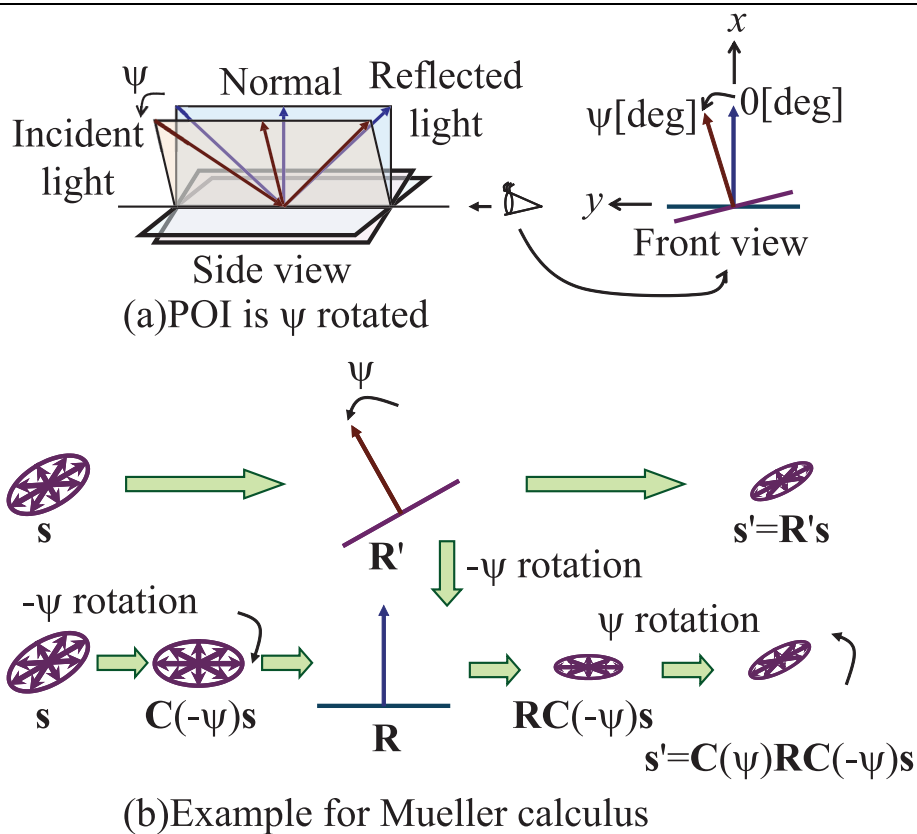
where rotation matrix  $\mathbf{C}$  is given as:

$$\mathbf{C}(\psi) = \begin{pmatrix} 1 & 0 & 0 & 0 \\ 0 & \cos 2\psi & -\sin 2\psi & 0 \\ 0 & \sin 2\psi & \cos 2\psi & 0 \\ 0 & 0 & 0 & 1 \end{pmatrix}. \quad (2.10)$$

As for the case in Figure 2.2, observed light is a composition of reflected light and transmitted light. Therefore, the Stokes vector  $\mathbf{s}'$  of the observed light is calculated as follows:

$$\mathbf{s}' = \mathbf{C}(\psi)\mathbf{R}\mathbf{C}(-\psi)\mathbf{s}_r + \mathbf{C}(\psi)\mathbf{T}\mathbf{C}(-\psi)\mathbf{s}_t, \quad (2.11)$$

where Stokes vectors of the incident light are represented as  $\mathbf{s}_r$  and  $\mathbf{s}_t$ , and where  $\mathbf{s}_r$  and  $\mathbf{s}_t$  represent the lights that are set in the origin of the reflection and transmission, respectively.




---

Figure 2.5: Calculation example of rotation Mueller matrix for reflection.

---

### 2.2.3 Phase Shift

If an incident angle is larger than the critical angle, then the light does not transmit and totally reflects. This phenomenon is called total reflection and occurs when the light is inside the object. Critical angle is defined in following equation:

$$\sin \theta_C = \frac{n_2}{n_1}. \quad (2.12)$$

Here,  $n_1$  and  $n_2$  are the refractive indices of two materials, where  $n_1 > n_2$ ; for example,  $n_1$  and  $n_2$  might be the refractive indices of the object and the air, respectively. The phase of the reflected light shifts when the total reflection occurs. Therefore, for the total reflection, the following matrix  $\mathbf{D}$  is used instead of the reflection Mueller matrix  $\mathbf{R}$ :

$$\mathbf{D}(\delta) = \begin{pmatrix} 1 & 0 & 0 & 0 \\ 0 & 1 & 0 & 0 \\ 0 & 0 & \cos \delta & \sin \delta \\ 0 & 0 & -\sin \delta & \cos \delta \end{pmatrix}, \quad (2.13)$$

where  $\delta$  is the amount of the phase shift, calculated by using the following formula:

$$\tan \frac{\delta}{2} = \frac{\cos \theta \sqrt{\sin^2 \theta - n^2}}{\sin^2 \theta}, \quad (2.14)$$

where  $\theta$  is the incident angle and  $n = n_2/n_1$ , where  $n_1$  and  $n_2$  are the refractive indices of the object and the air, respectively.

When the incident angle is less than the Brewster angle, the phase of the reflected light will be inverted; thus, the matrix  $\mathbf{D}(180^\circ)$  should be multiplied from the left to the reflection Mueller matrix. The Brewster angle is defined in Equation (2.3).

### 2.2.4 Degree of Polarization

Because the linear polarizer is used in this research, the fourth parameter  $s_3$  of the Stokes vector cannot be determined. The relationship between the Stokes vector  $(s_0, s_1, s_2)^T$  and  $I_{\max}$ ,  $I_{\min}$ ,  $\psi$  is:

$$\begin{pmatrix} s_0 \\ s_1 \\ s_2 \end{pmatrix} = \begin{pmatrix} 1 & 0 & 0 \\ 0 & \cos 2\psi & -\sin 2\psi \\ 0 & \sin 2\psi & \cos 2\psi \end{pmatrix} \begin{pmatrix} I_{\min} + I_{\max} \\ I_{\min} - I_{\max} \\ 0 \end{pmatrix}, \quad (2.15)$$

where  $I_{\max}$  and  $I_{\min}$  are defined in Section 2.1, and  $\psi$  is a POI angle also defined in Section 2.1. The DOP represents how much the light is polarized and is defined as follows:

$$\hat{\rho} = \frac{\sqrt{s_1^2 + s_2^2 + s_3^2}}{s_0}. \quad (2.16)$$

However, linear polarizer can only calculate the following degenerated DOP:

$$\rho = \frac{I_{\max} - I_{\min}}{I_{\max} + I_{\min}} = \frac{\sqrt{s_1^2 + s_2^2}}{s_0} . \quad (2.17)$$

For the remainder of this thesis, I refer to the ratio calculated by Equation (2.17) as DOP.

## 2.2.5 Illumination Distribution

In this thesis, I assume that all light sources are unpolarized. In Chapter 5, I assume that the intensity of the illumination is known.

## CHAPTER 3

# SHAPE ESTIMATION OF TRANSPARENT OBJECTS BY USING POLARIZATION ANALYSIS AND THERMAL RADIATION

In this chapter, I explain the method to solve the ambiguity problem by introducing thermal radiation.

### **3.1 Introduction**

Chapter 2 explained how to calculate surface normal from polarization data. However, there exists an ambiguity problem of determining the zenith angle  $\theta$  from the DOP (degree of polarization)  $\rho$ , since the correspondence between  $\rho$  and  $\theta$  is not one-to-one but one-to-two. Fortunately, the correspondence between the DOP and the zenith angle will be one-to-one if we obtain the DOP of the thermal radiation observed in the infrared light domain. In this chapter, I explain how to obtain the correct surface normal by disambiguating  $\theta$  by analyzing the thermal radiation by using the knowledge in thermodynamics and optics.

First, Section 3.2 shows some assumptions for the method, and Section 3.3 introduces the basic theory of thermal radiation. Next, Section 3.4 and 3.5 derives the DOP of thermal radiation by two different approaches. Finally, Section 3.6 explains the method to determine the surface normal by solving the ambiguity problem using the DOP derived in Section 3.4 and 3.5.

### **3.2 Assumptions**

There are several assumptions I use to successfully apply the method:

- 1 The object is observed as an orthographic projection to the image plane of the camera.
- 2 The object is transparent and solid.
- 3 The refractive index is known and constant for any part of the object.
- 4 The object's surface is optically smooth (not microscopically rough).
- 5 The object's surface is geometrically smooth and closed ( $C^1$  surface).
- 6 No self-occlusion exists. There is no "jump" in the height of the object's surface.
- 7 The entire frontal surface is included in the camera field of view.
- 8 While observing the reflected light in the visible light domain, the light that is directly reflected from the object's surface should be observed. The light that is reflected two or more times or is transmitted should not be observed.
- 9 While observing the thermal radiation in the infrared light domain, the light that is directly radiated from the object's surface should be observed. The light that is reflected at the object's surface should not be observed.
- 10 The disambiguation method of the azimuth angle  $\phi$  shown in Section 2.1.1 can be applied.

Assumption 1 is not the limitation of the method but of the polarizer. The polarizer shows the best performance if the light strikes the polarizer orthogonally. The method itself can be improved for the perspective projection.

In fact, assumption 2 is not mandatory. The method is also effective for opaque objects that have a highly specular surface. Also, by using a realtime capture system [WMPA97, FTA+98, HC02], the method can be applied to non-solid objects.

Assumptions 5 and 6 imply that the surface normal can be calculated by differentiating the height of the object's surface.

Several kinds of concave objects violate assumption 8 and produce a less precise shape of the object. From assumption 10, objects that have complete concave parts — a surface that is always concave for any direction, such as dimples — cannot be modeled automatically by the proposed method.

There are more internal interreflections in transparent objects than in opaque objects. According to my way of thinking, a method that can measure the shape of transparent objects is robustly applicable to any opaque object. Therefore, to prove the robustness of the method, I applied the method to transparent objects.

### 3.3 Thermal Radiation

Heat energy can propagate through space. This phenomenon is referred to as heat propagation. A blackbody can completely absorb the heat energy radiated. According to Kirchhoff's law, the ratio between radiant and incoming heat energy is independent of the object; rather, it is dependent only on the temperature of the object. A blackbody, which completely absorbs energy, can also radiate more energy than any other objects that have the same temperature.

From the Planck radiation law, radiation energy,  $w$ , from the blackbody at the temperature  $T$  and the wavelength  $\lambda$  is

$$w = \frac{2hc^2}{\lambda^5} \frac{1}{\exp(hc/\lambda kT) - 1} \quad , \quad (3.1)$$

where  $h = 6.6262 \times 10^{-34} [J \cdot s]$  is the Planck constant,  $c = 2.997925 \times 10^8 [m/s]$  is the speed of light, and  $k = 1.38066 \times 10^{-23} [J/K]$  is the Boltzmann constant. The energy distribution of the blackbody expressed as Equation (3.1) is shown in Figure 3.1. From the figure, it is apparent that the extremes of distributions shift along the temperature increment, and in the area of room temperature, they exist in the infrared region. Therefore, it is appropriate to employ infrared measurement for measuring the radiation energy of a blackbody at room temperature.

By integrating  $w$  in Equation (3.1) through all wavelengths, the Stephan-Boltzman law will be derived,

$$W = \sigma T^4 \quad , \quad (3.2)$$

where  $\sigma$  is the Stephan-Boltzmann constant and  $\sigma = 5.6705 \times 10^{-8} [W/m^2 \cdot K^4]$ . Given that any object has a positive temperature, any object should radiate energy.

In the two following sections, I describe how I derive the DOP (degree of polarization) in infrared light, by using two approaches. In Section 3.4 I describe how the DOP is derived by using Kirchhoff's law from the theory of thermodynamics, and in Section 3.5 I explain how the DOP is derived by considering the light emitted from inside the objects from the theory of optics. As a result, both of the derived DOP values will be the same equation.

First, I will describe the unified theory of the polarization in infrared light, which does not depend on whether the object is transparent, translucent, or opaque. To actualize this idea, let us assume that, in a sense, all objects can be considered to be opaque; the light that hits the interface surface of objects can only be reflected or be absorbed. The light that transmits into a transparent object will then be referred to as the light that is absorbed into it. The light transmitted into a transparent object escapes into the air from somewhere on the surface of the object. Let us say that such escaped light is the light thermally emitted from the object.

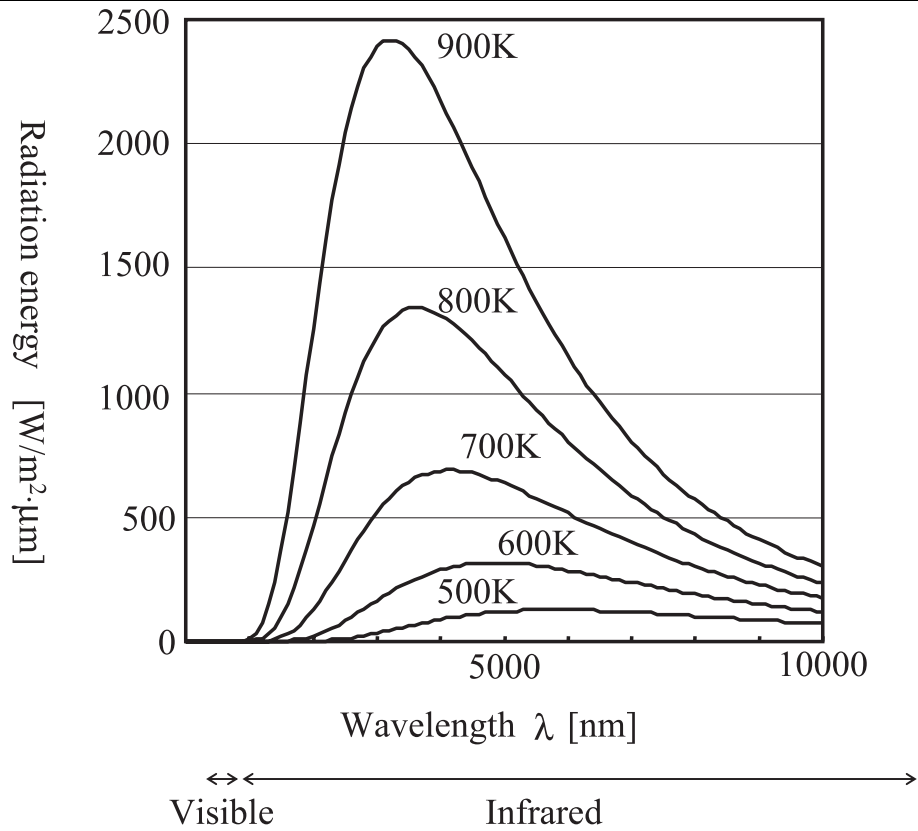


Figure 3.1: Energy distribution of blackbody.

---

This assumption that all objects can be considered to be opaque is used in Section 3.4. This assumption holds when the system is in thermal equilibrium, given that all light is expected to have the same amount of energy and to radiate in all directions.

### 3.4 Kirchhoff's Law

By considering the state when the system is in thermal equilibrium, and by using Kirchhoff's law, I can explain the polarization of thermal radiation [JL94, JLJ96, WLT98, Nic65, Nic70].

A typical object emits a lower amount of radiation energy than that emitted from a blackbody. The ratio of the amount of radiation energy of a typical object in relation to that from a blackbody is referred to as the emissivity, and is denoted as  $\varepsilon$ .

Let us assume that infrared light strikes a smooth surface. Its parallel and perpendicular intensity to the plane of incidence are denoted as  $I_{a\parallel}$  and  $I_{a\perp}$ , respectively. When the infrared light strikes a surface with the incident angle  $\theta$ , the intensity of parallel and perpendicular components of reflected light are given as  $R_{\parallel}I_{a\parallel}$  and  $F_{\perp}I_{a\perp}$ , respectively.

From the law of the conservation of energy, the difference between the incoming and reflected intensities,  $(1 - R_{\parallel})I_{a\parallel}$  and  $(1 - R_{\perp})I_{a\perp}$ , is the amount of energy absorbed by the body. By denoting this ratio as absorptance  $\alpha$ , since Kirchhoff's law provides  $\varepsilon = \alpha$ , I obtain

$$\begin{aligned}\varepsilon_{\parallel}(T, \lambda, \theta) &= 1 - R_{\parallel} \\ \varepsilon_{\perp}(T, \lambda, \theta) &= 1 - R_{\perp} .\end{aligned}\tag{3.3}$$

Let us denote the intensity of thermal radiation from the perfect blackbody as  $W$ . Then, the intensity of thermal radiation from the object is  $\varepsilon W$ , and its polarization can be written by using Equation (3.3):

$$\begin{aligned}\rho_{\text{IR}} &= \frac{I_{\text{max}} - I_{\text{min}}}{I_{\text{max}} + I_{\text{min}}} = \frac{\varepsilon_{\parallel}W - \varepsilon_{\perp}W}{\varepsilon_{\parallel}W + \varepsilon_{\perp}W} \\ &= \frac{R_{\perp} - R_{\parallel}}{2 - R_{\parallel} - R_{\perp}}\end{aligned}\tag{3.4}$$

where  $\rho_{\text{IR}}$  is the degree of polarization in infrared light. I use a different notation ( $\rho_{\text{IR}}$ ) to distinguish this condition from that in the visible light. By substituting Equation (2.2) for Equation (3.4), I can derive the relationship between the degree of polarization,  $\rho_{\text{IR}}$ , and the emitting angle,  $\theta$ .

### 3.5 Emitted Light

Let us explain the polarization phenomenon of thermal radiation by considering the light emitted from inside the object [San65]. Thermal radiation emitted from inside the object is transmitted through the interface surface and radiated into the air.

For the explanation in this section, suppose material 1 to be the object and material 2 to be the air, as shown in Figure 2.1. In this case,  $\theta_2 > \theta_1$ . The refractive index of the object relative to the air will be  $n = n_1/n_2$ .  $\theta_2$  is the emitting angle, and I will derive the degree of polarization as a function of  $\theta = \theta_2$ .

I can define the parallel and perpendicular intensity ratios of transmission,  $T_{\parallel}$  and  $T_{\perp}$ , as

$$\begin{aligned} T_{\parallel} &= \frac{I_{t\parallel}}{I_{a\parallel}} = \frac{\sin 2\theta_1 \sin 2\theta_2}{\sin^2(\theta_1 + \theta_2) \cos^2(\theta_1 - \theta_2)} \\ T_{\perp} &= \frac{I_{t\perp}}{I_{a\perp}} = \frac{\sin 2\theta_1 \sin 2\theta_2}{\sin^2(\theta_1 + \theta_2)} \end{aligned} \quad (3.5)$$

where  $I_{t\parallel}$  is the component parallel to the POI (plane of incidence) of the transmitted light, and  $I_{t\perp}$  is the component perpendicular to the POI of the transmitted light. Therefore,  $I_{\max}$  and  $I_{\min}$  will be written by using the total energy of the emitted light,  $W$ , as

$$I_{\max} = \frac{T_{\parallel}}{T_{\parallel} + T_{\perp}} W, \quad I_{\min} = \frac{T_{\perp}}{T_{\parallel} + T_{\perp}} W. \quad (3.6)$$

By substituting Equation (3.6) and (3.5) into Equation (2.5) with Snell's law, I can represent the degree of polarization of thermal radiation  $\rho_{\text{IR}}$  as

$$\begin{aligned} \rho_{\text{IR}} &= \frac{I_{\max} - I_{\min}}{I_{\max} + I_{\min}} = \frac{T_{\parallel} - T_{\perp}}{T_{\parallel} + T_{\perp}} \\ &= \frac{(n - 1/n)^2 \sin^2 \theta}{2 + 2n^2 - (n + 1/n)^2 \sin^2 \theta + 4\sqrt{n^2 - \sin^2 \theta} - n^2 \sin^2 \theta + \sin^4 \theta}. \end{aligned} \quad (3.7)$$

### 3.6 Degree of Polarization of Thermal Radiation

$R_{\parallel} + T_{\parallel} = 1$  and  $R_{\perp} + T_{\perp} = 1$  holds, thus the resulting  $\rho_{\text{IR}}$  in both Section 3.4 (Equation (3.4)) and Section 3.5 (Equation (3.7)) are the same. This is because both explanations deal with the same phenomenon, though the approach is different; one is based on the energy conservation law (Kirchhoff's law), the other on the mechanism of the phenomenon.

Figure 3.2(b) shows the relation between the DOP,  $\rho_{\text{IR}}$ , and the emitting angle,  $\theta$ .

The refractive index of the graph shown in Figure 3.2(b) is 1.5. Because the refractive index is affected by the wavelength, the refractive index of infrared light is slightly different from that of visible light. For example, the refractive index of a certain glass is approximately

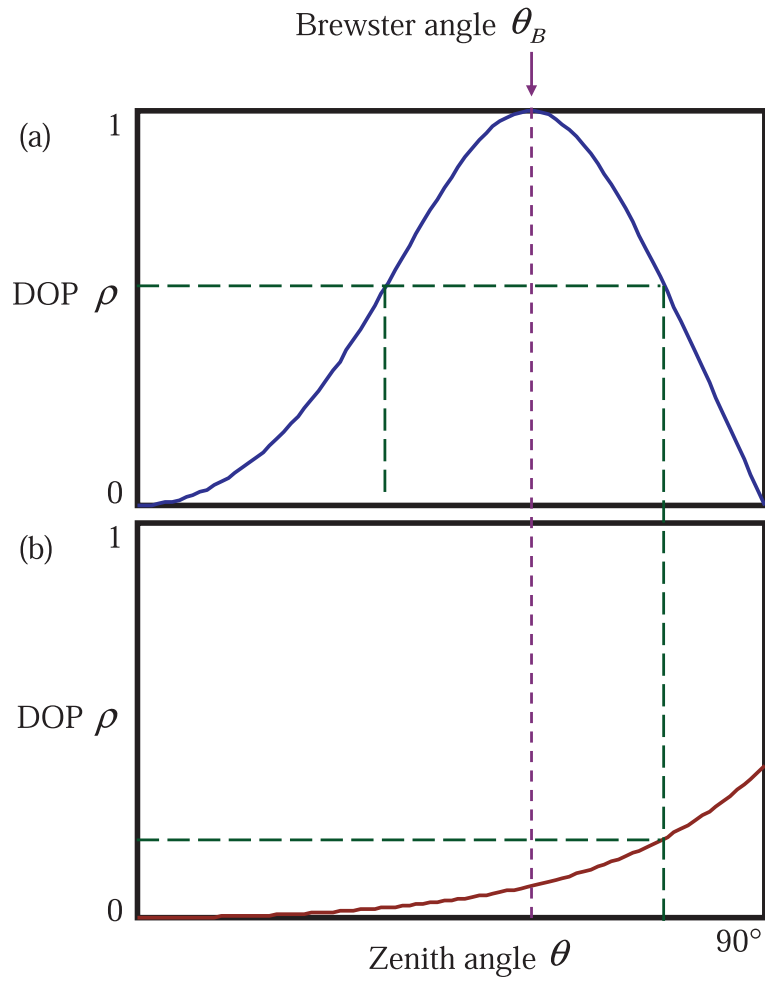


Figure 3.2: DOP of (a)reflected light (visible light) ( $n = 1.5$ ), and (b)thermal radiation (infrared light) ( $n = 1.5$ ).

---

1.52 when the wavelength is approximately 500nm (visible light), and the refractive index of that glass is approximately 1.49 when the wavelength is approximately  $2\mu\text{m}$  (infrared light). I use the same refractive index in infrared light as that in visible light because the difference is negligible.

As shown in Figure 3.2(b), the relation is a one-valued function; there is a 1-to-1 correspondence between the DOP and the emitting angle. Therefore, once I measure the DOP in an infrared light, I can uniquely determine the emitting angle. For the sake of comparison, Figure 3.2(a) represents the visible light condition. In this function, as mentioned, one DOP value corresponds to two emitting angles.

Unfortunately, however, the DOP in emitted infrared light is much smaller than that in reflected visible light; at the maximum, around an emitting angle of 90 degrees, it is still 40 percent. In the smaller area, the DOP is less than 10 percent. In order to obtain such a small DOP, It is required to measure  $I_{\text{max}}$  and  $I_{\text{min}}$  precisely. It is impractical to perform such a highly accurate measurement using an ordinary CCD camera with a 256 gray level.

In order to overcome this difficulty, I propose to use both visible and infrared light. By using visible light, I can achieve a highly accurate measurement with ambiguity. By using the infrared light, I discriminate between the two sides. First I determine the DOP in the infrared region at the Brewster angle. Using this DOP as the threshold value, I can determine to which side, with respect to the Brewster angle, the emitting angle belongs, as indicated by the dotted purple line in Figure 3.2.

### 3.7 Summary

In this chapter, I proposed a method to measure the surface shape of transparent objects by analyzing the polarization in visible light domain and in infrared light domain. Only analyzing the degree of polarization of reflected light in visible light domain results in an ambiguity, since the relationship between the degree of polarization and the zenith angle is not one-to-one. This ambiguity problem can be solved by analyzing the degree of polarization of thermal radiation in infrared light domain, since the relationship between the degree of polarization and the zenith angle is one-to-one. Surface normal of the surface of transparent objects is determined by the degree of polarization of visible light by solving the ambiguity with the degree of polarization of infrared light. Finally, by integrating the surface normal map, the height map will be computed.

The experimental setup to obtain polarization data in visible light domain is presented in Section 6.1.1, and the experimental setup to obtain polarization data in infrared light domain is presented in Section 6.1.2. Implementation detail to obtain polarization data in visible light

domain is presented in Section 6.2.1, and implementation detail to obtain polarization data in infrared light domain is presented in Section 6.2.2. Experimental results of applying the method proposed in this chapter are presented in Section 6.3.1.

Target objects for the method proposed in this chapter must obey the assumptions suggested in Section 3.2. I will discuss what kinds of objects are measurable and what kinds of objects are not measurable in more details below.

- The method assumes that internal interreflection does not occur. The light ray from the light source, first, hits the object's surface and then strikes the camera. Multiple reflection neither inside nor outside the object is considered. Therefore, if internal interreflection occurs, that is, if multiple reflections inside the transparent object occur or the reflections outside the transparent object occur between the surface patches of the object's surface, the measurement result will be polluted by some noise. Also, if external interreflection occurs, that is, if multiple reflections occur between the transparent object and the experimental setup, the measurement result will be polluted by some noise. The third method described in Chapter 5 — the method that considers internal interreflection by using a polarization raytracing method — solves the problem of internal interreflection. The object and the light sources are placed far apart from each other as is shown in Section 6.1.1, and this reduces the interference of the external interreflection. The object and the camera are also set apart as is shown in Section 6.1.1 and 6.1.2 to reduce the influence of the external interreflection. The object is set on top of a black pipe to reduce the light coming from the rear surface of the object in order to realize the assumption that the light hits at the frontal surface only once.

It might seem that failure to consider internal interreflection is a shortcoming of the method described in this chapter. This is true in the sense of precision, but it is not true in the sense of applicability. Since the method assumes that the camera observes only the reflection at the object's surface and does not consider the transmission, the method does not constrict the internal structure of the target object. Therefore, the method is applicable to not only transparent objects but also translucent objects, opaque objects, metallic objects, hollow transparent objects, and birefringent transparent objects. A birefringent transparent object is an object whose refractive index of the object slightly differs for each direction. Hollow transparent objects include bottles, glasses, ornaments with an air bubble inside them, etc., but the frontal surface shape is estimated and neither the rear surface shape nor the shape of the bubble is estimated. Since the method assumes that the camera observes the specular reflection of the object's surface, the method cannot be applied to perfect diffuse objects (Lambertian surfaces) and perfect absorbers. The method also assumes that the object's surface is optically smooth;

thus, the method is only applicable to perfect specular objects.

If the object's shape is too complex and the interference of the internal interreflection is too strong, the method will provide an erroneous result. The method can be applied to shallow concave objects because some of these objects still obey the assumption that the light reflected at the surface only once is observed; however, the method cannot be applied to deep concave objects because some of these objects violate this assumption and cause multiple reflection at the concave part. If the object's surface has a "dimple" — concavity in convexity, a part of a surface that is concave when observed from any direction — the method cannot be applied since the azimuth angle  $\phi$  is not estimated by the method shown in Section 2.1.1. In this chapter, I discussed how to estimate the zenith angle  $\theta$ ; however, the surface normal is represented by two angles, zenith angle  $\theta$  and azimuth angle  $\phi$ , in polar coordinates. Azimuth angle  $\phi$  is estimated by the method shown in Section 2.1.1. This method first estimates the azimuth angle  $\phi$  at the occluding boundary, because the surface normal at the occluding boundary is known by using the derivation that the surface normal heads outward from the object and orthogonally to the camera direction due to the assumption that the object is geometrically smooth and closed. After that, the method propagates the determination of the azimuth angle  $\phi$  from the occluding boundary to the inner part of the object area by using a smoothness constraint. Since I assume that the object is geometrically smooth, this method seems to be always successful in estimating the azimuth angle; however, dimples at the object's surface causes failure to estimate the azimuth angle due to the fact that the azimuth angle will be just the opposite at the boundary of the dimple; the azimuth angle has a singularity at this boundary.

- The method assumes that the object's surface must be a  $C^1$  surface (geometrically smooth surface), because the surface normal must be calculated. If the object has a discontinuous part, the method cannot be applied. Theoretically, the method cannot be applied to a  $C^0$  surface (continuous surface), because the surface normal cannot be calculated at the non-smooth area. However, in practice, some of the  $C^0$  object's shape can be estimated by the method proposed in this chapter.
- The method assumes that the refractive index of the object is known. Therefore, if the refractive index is unknown, the object's shape cannot be estimated. However, the method can be applied to an object whose refractive index varies from part to part if such variation of the refractive index is known.
- The experimental setup shown in Section 6.1.1 and 6.1.2 cannot obtain the polarization data in realtime; however, there exist some measurement systems that can obtain the

polarization data in realtime [WMPA97, FTA+98, HC02]. But this method must observe the object from same direction with two different cameras; thus, even if I update the measurement system into a realtime one, the method cannot estimate the shape of deforming objects.

- The method observes the thermal radiation of the object itself by heating up the object. As is described in Section 6.1.2 and 6.2.2, the temperature of the object is increased up to 30–40 degrees Celsius. Such temperature does not deform a solid object's shape much; however, objects that melt at this temperature, such as ice or jelly, cannot be measured by this system.

To summarize: Transparent solid objects are measurable if they have optically smooth surfaces and  $C^1$  closed surfaces, if their refractive index is known, if they do not melt by heating up to 30–40 degrees Celsius, and if they have no deep concave part, though some noise will be caused by internal interreflection. Also, translucent objects, opaque objects, metallic objects, hollow transparent objects, and birefringent transparent objects are measurable. Some objects that have a shallow concave part are measurable. Some of the objects whose surface is  $C^0$ , such as a cube, diamond, or pyramid, are measurable. Objects whose refractive index varies from part to part are measurable if we know the refractive index in any part of the object.

The following are the examples of the objects that are unmeasurable by the method proposed in this chapter:

- Objects that have optically rough surfaces, such as a perfect diffuse object
- Objects that have a deep concave part or dimples (concavity in convexity)
- Objects that have discontinuous parts
- Objects whose refractive index is unknown
- Objects that deform from time to time, such as liquid, jelly, or soap bubbles
- Objects that melt when heated up to 30–40 degrees, such as ice or jelly

## CHAPTER 4

# SHAPE ESTIMATION OF TRANSPARENT OBJECTS BY USING POLARIZATION ANALYSIS AND DIFFERENTIAL GEOMETRY

In this chapter, I introduce the method of solving the ambiguity by rotating the object.

### 4.1 Introduction

Chapter 2 explained how to calculate surface normal from polarization data. In that chapter, I indicated that there exists an ambiguity problem: the surface normal cannot be uniquely determined from several possible surface normals obtained by the measurement. Surface normal  $\mathbf{n}$  is represented by zenith angle  $\theta$  ( $0^\circ \leq \theta \leq 90^\circ$ ) and azimuth angle  $\phi$  ( $0^\circ \leq \phi < 360^\circ$ ) as in Figure 4.1. The degree of polarization  $\rho$  and the POI (plane of incidence) angle  $\psi$  are obtained from polarization data. As I discussed in Section 2.1.1, I can determine the azimuth angle  $\phi$  from the POI angle  $\psi$ . Also, as I discussed in Section 2.1.2, the zenith angle  $\theta$  can be determined from the degree of polarization  $\rho$ , though there is an ambiguity problem. Chapter 3 explained how to disambiguate the ambiguity of  $\theta$  by analyzing the degree of polarization of not only the reflected light in visible light domain but also the thermal radiation in infrared light domain. In this chapter, I explain how to disambiguate the ambiguity of  $\theta$  and to obtain the correct surface normal by rotating the object and analyzing the differential-geometrical property of the surface, observing the object in visible light domain, which is a different approach from the method in Chapter 3 but has the same purpose.

To satisfy this requirement, I propose to tilt (rotate) the object at a small angle. Tilting the

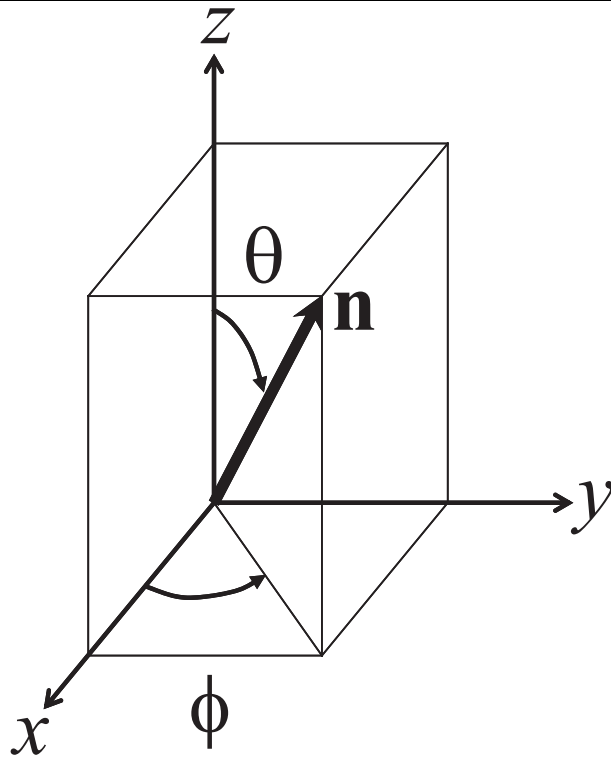


Figure 4.1: Coordinates of surface normal.

---

object with respect to the camera coincides with observing the object from different directions. The ambiguity is solved by comparing the DOP (degree of polarization) of two sets of data obtained coming from two different directions. The DOP of the two sets of data must be compared at the identical point. That is, the method must find the points of the two data sets that represent the same point on the object's surface. For this purpose, I introduce the geometrical property of the object surface. I find two points where the invariant value of the surface is identical, and utilize those two points as corresponding (matching) points.

The structure of the remainder of this chapter is as follows. In Section 4.2, I state the assumptions of my method to successfully apply the proposed method. If the reader of this thesis is not familiar to the fundamental theory of Gaussian geometry, please read the Appendix B or the literature [Car76, Hor86].

In Section 4.3, I segment the data of the DOP in some regions, and also indicate how I disambiguate each region. I describe the method of finding the corresponding point by considering its geometrical property, in Section 4.4. Also, I furnish proof that I can obtain the invariant value of the geometrical property from the DOP data.

Finally, I point out that I can uniquely determine the zenith angle (incident angle)  $\theta$  by calculating the difference of the DOP between the corresponding points (Section 4.5).

Consequently, I finally obtain conclusions as follows:

1. I segment the DOP data in the B-O region, the B-N region, and the B-B region (Section 4.3).
2. I can straightforwardly disambiguate the B-O region and the B-N region as shown in Section 4.3.
3. For the B-B region, I find the point where the DOP is minimum and the surface normal is parallel to the rotation direction, and utilize that point as a corresponding point (Section 4.4).
4. I calculate the difference of the DOP between those two corresponding points, and solve the ambiguity from the sign of this difference (Section 4.5).

## 4.2 Assumptions

There are several assumptions I use to successfully apply the method:

- 1 The object is observed as an orthographic projection to the image plane of the camera.
- 2 The object is transparent and solid.

- 3 The refractive index is known and constant for any part of the object.
- 4 The object's surface is optically smooth (not microscopically rough).
- 5 The object's surface is geometrically smooth and closed ( $C^2$  surface).
- 6 No self-occlusion exists. There is no "jump" in the height of the object surface.
- 7 The entire frontal surface is included in the camera field of view.
- 8 The light that is directly reflected from the object's surface should be observed. The light that is reflected two or more times or is transmitted should not be observed.
- 9 The disambiguation method of the azimuth angle  $\phi$  shown in Section 2.1.1 can be applied.
- 10 The light caused by internal interreflection is unpolarized and uniform for all the points on the object's surface.
- 11 Hints for region segmentation are given by the human operator.
- 12 The class of regions does not change even if I rotate the object at a small angle.
- 13 Proper rotation direction is given by the human operator.
- 14 The object still obeys all these assumptions even if I rotate the object at a small angle.

Assumption 1 is not the limitation of the method but of the polarizer. The polarizer shows the best performance if the light strikes orthogonally into the polarizer. The method itself can be improved for the perspective projection.

In fact, assumption 2 is not mandatory. The method is also effective for opaque objects that have a highly specular surface. Also, by using a realtime capture system [WMPA97, FTA+98, HC02], the method can also be applied to non-solid objects.

Assumptions 5 and 6 imply that the surface curvature can be calculated by differentiating the height of the object surface 2 times.

Several kinds of concave objects violate assumption 8 and produce a less precise shape of the object. From assumption 9, objects that have complete concave parts — a surface that is always concave for any direction, for example, dimples — cannot be modeled automatically by the proposed method.

I rotate the object to obtain the polarization data observed from two different views. The proposed method assumes that there are no internal interreflections and that the rotation angle of the object is infinitesimal. However, under certain conditions, internal interreflections cannot be avoided. From assumption 10, I subtract the intensity caused by internal interreflection

from the input data to reduce the interference of internal interreflection. I consider that such modification empirically produces more satisfactory data than does input raw data; however, such assumptions are theoretically not always true.

The proposed method needs to apply a region segmentation method to the input polarization data and to classify the region after segmentation. If the object is complicated and is rotated at a large angle, the class of the region will often change and will thus violate assumption 12. In addition, if the region changes in topology — for example, if it splits, vanishes, or regenerates — then such a measurement also violates the assumption.

There are more internal interreflections in transparent objects than in opaque objects. According to my theory, a method that can measure the shape of transparent objects is robustly applicable to any opaque objects. Therefore, to prove the robustness of the method, I applied the method to transparent objects.

### 4.3 Brewster Segmentation

I have explained how to obtain the DOP of the light reflected on the object surface in Chapter 2. Now, I segment the DOP data into some regions bounded by the Brewster angle  $\theta_B$ . Points of the Brewster angle have no ambiguity and the DOP  $\rho$  is equal to 1.

I assume that the object is projected orthographically to the camera. In addition, I assume that the surface shape observed from the camera causes no self occlusion; thus, the surface is a regular surface and can be represented as  $z = f(x, y)$ .

Since I assume that the object is a closed, smooth object, the curve connected by points of the Brewster angle will form a closed curve. This curve is sometimes thick, sometimes thin, and sometimes a combination of both. I denote a point where the zenith angle is equal to the Brewster angle as the “Brewster point” and the closed curve consisting of Brewster points as the “Brewster curve.” I define the segmentation by Brewster curves as “Brewster segmentation.”

Now I want to determine the incident angle (zenith angle)  $\theta$ ; however, the correspondence between the DOP  $\rho$  and the incident angle  $\theta$  is 1 to 2; thus, I have to disambiguate this ambiguity to determine the correct incident angle (Figure 2.4). The incident angle of all points in the region, segmented through the Brewster segmentation, is either greater than the Brewster angle or smaller than the Brewster angle. Therefore, I can uniquely determine all the incident angles in the region if I can disambiguate only one point in the region. The graph described in Figure 2.4 indicates that the correspondence between  $\theta$  and  $\rho$  is 1 to 1 at  $0^\circ \leq \theta \leq \theta_B$ , and also 1 to 1 at  $\theta_B \leq \theta \leq 90^\circ$  (details are written in p.57). Therefore, if I know whether the incident angle  $\theta$  is greater or smaller than the Brewster angle  $\theta_B$ , I can

determine the value of  $\theta$  uniquely from the value of  $\rho$ .

The coordinates are defined as Figure 4.1, where the camera is placed at the  $z$  axis. I define  $\theta$  as the angle between surface normal and  $z$  axis,  $\phi$  as the angle, from  $x$  axis to  $y$  axis, between  $x$  axis and the projected vector of surface normal to  $x$ - $y$  plane. Therefore, the zenith angle  $\theta$  of the surface normal  $\mathbf{n}$  equals the incident angle  $\theta$  ( $0^\circ \leq \theta \leq 90^\circ$ ), and the azimuth angle  $\phi$  of the surface normal  $\mathbf{n}$  is calculated from the POI angle  $\psi$  ( $0^\circ \leq \psi < 360^\circ$ ) with the method described in Section 2.1.1.

Now, let us consider the surface regions segmented with regard to the Brewster angle with a Gaussian sphere representation [Hor86, Car76]. The regions generated by Brewster segmentation can be grouped into three classes (Figure 4.2):

1. B-E region — a region enclosed within a Brewster curve and an occluding boundary (mapped to the equator on the Gaussian sphere),
2. B-N region — a region enclosed only with a Brewster curve and containing a surface normal toward the viewer direction (mapped to the north pole on the Gaussian sphere),
3. B-B region — a region enclosed only with one or more Brewster curves and neither containing the occluding boundary nor the surface normal facing the viewer.

‘B’ represents the capital letter B of the Brewster curve, ‘E’ represents the capital letter E of the equator, and ‘N’ represents the capital letter N of the north pole. The north pole is that of the Gaussian sphere, the direction where the camera is placed. The equator is that of the Gaussian sphere, the great circle where the occluding boundary is mapped with Gaussian mapping.

The result of the Brewster segmentation of the object depicted in Figure 4.3 is shown in Figure 4.4. Figure 4.4(a) is a gray image of the DOP, where  $\rho = 0$  is represented as black and  $\rho = 1$  is represented as white. Figure 4.4(b) is the result of the Brewster segmentation of Figure 4.4(a). There are two Brewster curves and one occluding boundary and one each of the B-E region, the B-B region, and the B-N region.

The DOP of the points of the Brewster curve is 1; thus, there is no ambiguity and the zenith angle (incident angle)  $\theta$  can be determined uniquely. The surface normal of the points of the occluding boundary faces out from the object and is perpendicular to the direction of the view, and the zenith angle  $\theta$  is  $90^\circ$ . There exist no data outside the occluding boundary. The zenith angle  $\theta$  of the points that map onto the North Pole is  $0^\circ$ , while the azimuth angle  $\phi$  is undefined at those points. Therefore, segmenting regions by B-curve, E-curve, and N-curve is considered to be the most efficient segmentation.

The B-E region is the region that includes the occluding boundary whose zenith angle  $\theta$  equals  $90^\circ$ . On the Gaussian sphere, the B-E region is enclosed within a small circle mapped

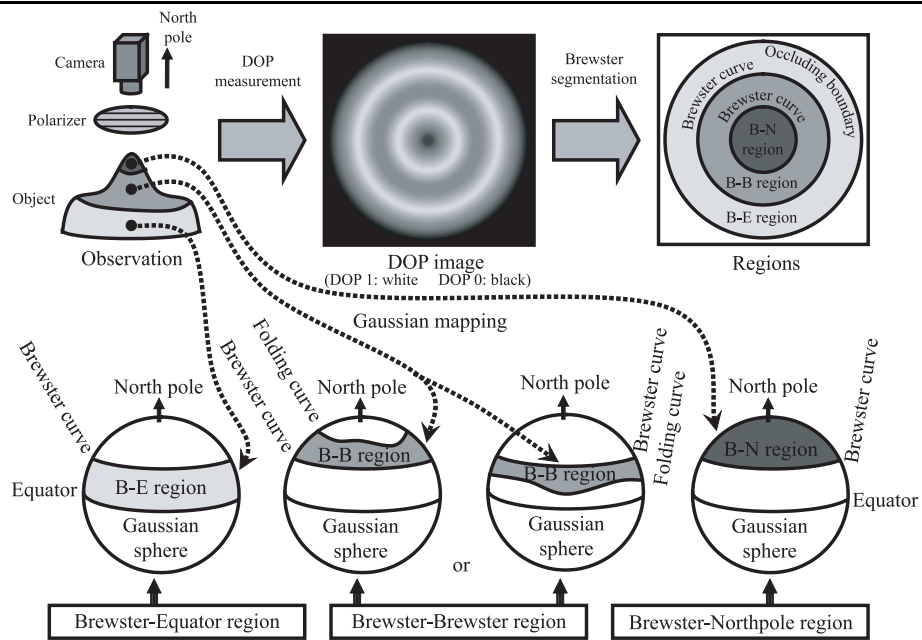


Figure 4.2: Gaussian mapping and regions.

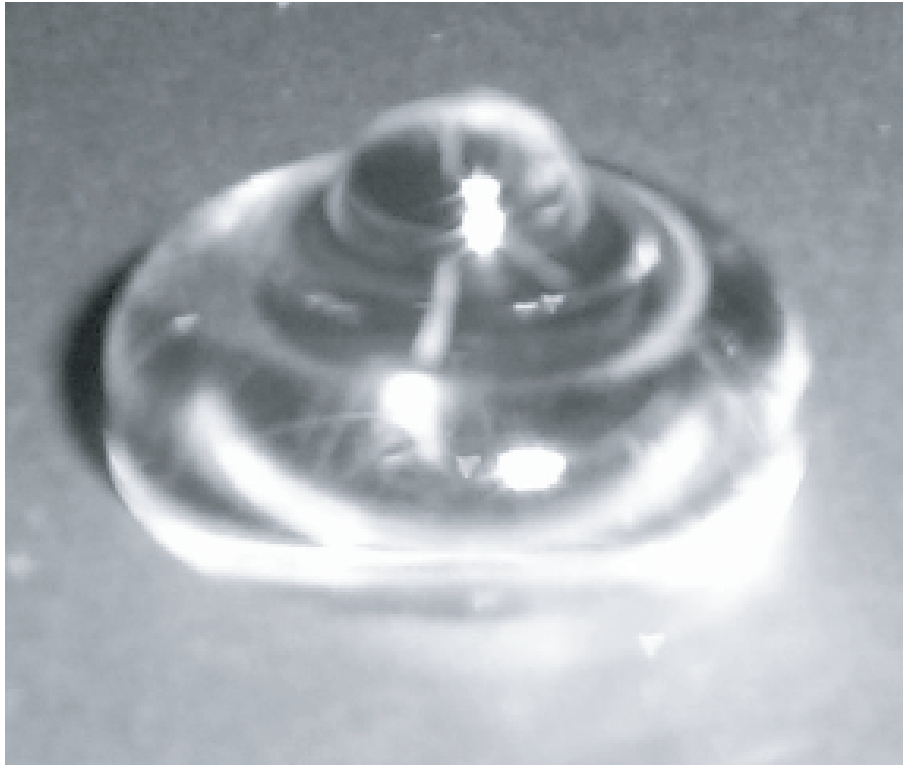
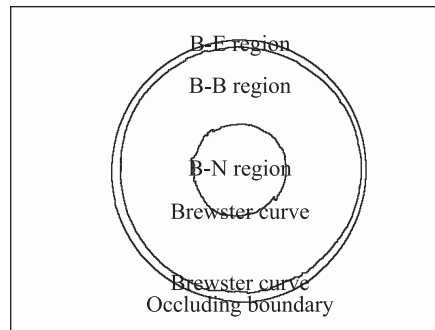


Figure 4.3: A photograph of the bell-shaped object.



(a)



(b)

Figure 4.4: (a) A gray image of obtained degree of polarization of the bell-shaped object and (b) the result of Brewster segmentation.

---

from the Brewster curve and an equator mapped from the occluding boundary. The zenith angle of all the points of the B-E region is located between the Brewster angle and the occluding angle,  $90^\circ$ . The graph described in Figure 2.4 indicates that the correspondence between  $\theta$  and  $\rho$  is one to one at this region,  $\theta_B \leq \theta \leq 90^\circ$ ; thus, I can uniquely determine the incident angle from an observed DOP,  $\rho$ .

The B-N region is the region that includes the point(s) mapped onto the North Pole on the Gaussian sphere. As shown in Figure 2.4, the region is mapped to a spherical cap on the Gaussian sphere, enclosed by a small circle mapped from the Brewster curve. The North Pole is located at the center of this spherical cap. The zenith angle of all the points in this region is in the range of  $0^\circ \leq \theta \leq \theta_B$ . From the graph in Figure 2.4, I can also conclude that, in this range, the correspondence between  $\theta$  and  $\rho$  is one-to-one, and I can also determine the zenith angle from the observed DOP.

The B-B region is defined as the region that includes neither the occluding boundary nor the North Pole points and is bounded by one or more Brewster curves. In the following sections, I will propose a method for disambiguating B-B regions.

I assume that, even if I tilt the object in an infinitesimal angle in any direction, the class of the region never changes through such object rotations. Specifically, I assume that the number of regions does not change through any object rotations, and also that regions deform and translate only infinitesimally. In addition, I assume that the self-occlusion never occurs even if I tilted the object at an infinitesimal angle.

To satisfy the above assumptions, I consequently assume that there are no points where the zenith angle  $\theta$  is equal to  $90^\circ$  except for the occluding boundary. Therefore, the only region that has the points where the zenith angle  $\theta$  is equal to  $90^\circ$  is the B-E region, and there are no regions that have the points where the zenith angle  $\theta$  is equal to  $90^\circ$  except for the B-E region. As a result, if there is a point where the DOP  $\rho$  equals 0, the zenith angle  $\theta$  of that point will always be  $0^\circ$  except for the occluding boundary. The B-N region is defined to have a point where the zenith angle  $\theta$  equals  $0^\circ$ ; thus, only the B-N region has a point where the DOP  $\rho$  equals 0 except for the B-E region. I specified that the region that is neither the B-E region nor the B-N region is the B-B region; thus, the zenith angle  $\theta$  of the points in the B-B region equals neither  $0^\circ$  nor  $90^\circ$ .

By calculating the background subtraction image, the occluding boundary can be calculated; thus, the B-E region is easily determined. The B-N region is determined only by searching the point where the degree of polarization equals zero. The region that is neither the B-E region nor the B-N region is the B-B region. Therefore, the obtained DOP data can be easily classified into B-E region, B-N region, and B-B region even if I do not solve the ambiguity.

The B-E region includes the occluding boundary whose zenith angle  $\theta$  equals  $90^\circ$ ; thus,

I can disambiguate this region and determine the zenith angle to be in the range of  $\theta_B \leq \theta \leq 90^\circ$ . The B-N region includes the points that will be mapped onto the North Pole of the Gaussian sphere, whose zenith angle  $\theta$  equals  $0^\circ$ ; thus, I can disambiguate this region and determine the zenith angle to be in the range of  $0^\circ \leq \theta \leq \theta_B$ . In the following sections, I will discuss only the method of disambiguating the B-B region.

Further discussions of the geometrical properties in Brewster segmentation are presented in Appendix C.

## 4.4 Corresponding Point

There are two possibilities for the existence of the B-B region on the Gaussian sphere. The B-B region is either on the northern side of the Brewster curve or on the southern side of the Brewster curve. The B-B region mapped onto the Gaussian sphere is bounded by one Brewster curve and one or more extra curves (Figure 4.5). By considering the points in the B-B region on the Gaussian sphere, I find that there is one extreme point — northernmost or southernmost — in each azimuth angle. I denote the set of these points to be a global folding curve or simply a folding curve. Along this curve, the original surface is folded and is mapped two or more times between the folding curve and the Brewster curve.

Consider mapping a local part of a surface onto a Gaussian sphere; if points of the surface map only onto one side of a curve on the Gaussian sphere and do not map onto the other side of such a curve, we define such a curve as a “local folding curve” or simply a “folding curve”. A global folding curve is also a local folding curve. Figure 4.6 illustrates the Gaussian mapping of a part of a bell-shaped surface having a local folding curve.

Now, I will prove that the folding curve is a geometrical invariant; Gaussian curvature at the folding curve will be zero.

**Theorem** *Any folding curve on an object’s surface is a parabolic curve on that object’s surface. That is to say, at any surface point on a folding curve, the Gaussian curvature at the surface point vanishes.*

**Proof.** A surface normal can be represented in gradient space, a space constructed by gradients  $p$  and  $q$ :

$$p = \frac{\partial H}{\partial x}, \quad q = \frac{\partial H}{\partial y} \quad (4.1)$$

where  $H = H(x, y)$  denotes the height of the object surface. A folding curve is an extremum not only in a Gaussian sphere, but also in gradient space,  $p = p(x, y)$  and  $q = q(x, y)$ .

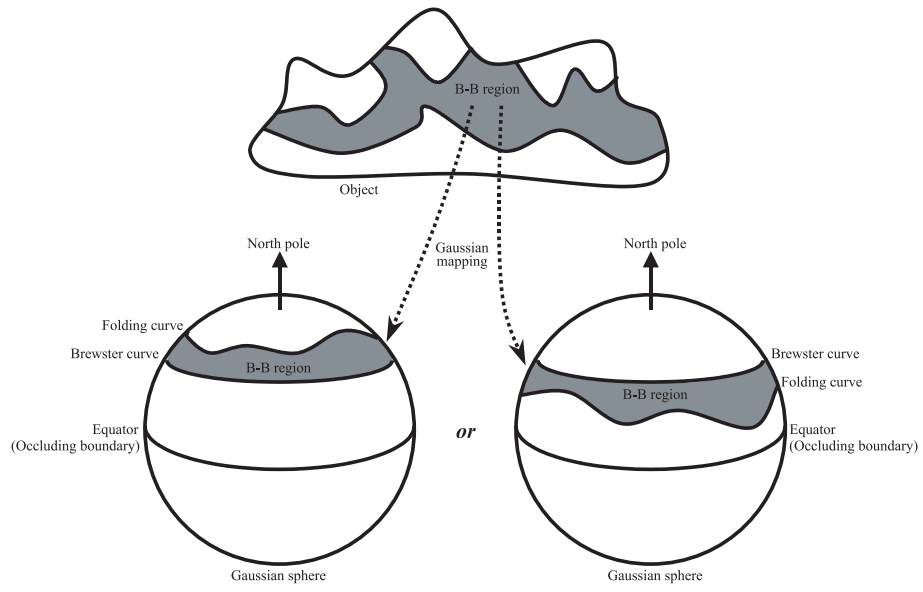


Figure 4.5: Gaussian mapping of B-B region.

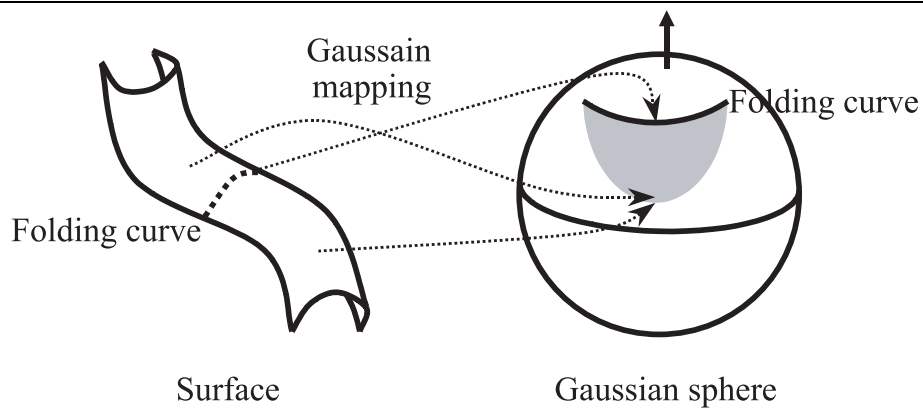


Figure 4.6: Gaussian mapping of bell-shaped surface.

Therefore, one or both of the following equations hold:

$$\frac{\partial p}{\partial x} = \frac{\partial p}{\partial y} = 0 \quad (4.2)$$

$$\frac{\partial q}{\partial x} = \frac{\partial q}{\partial y} = 0. \quad (4.3)$$

Hessian  $\mathcal{H}$  and Gaussian curvature  $K$  are related by the following equation [Car76]:

$$\text{sgn} K = \text{sgn} \det \mathcal{H} \quad (4.4)$$

where Hessian is defined as:

$$\mathcal{H} = \begin{pmatrix} \frac{\partial^2 H}{\partial x^2} & \frac{\partial^2 H}{\partial x \partial y} \\ \frac{\partial^2 H}{\partial y \partial x} & \frac{\partial^2 H}{\partial y^2} \end{pmatrix}. \quad (4.5)$$

Since (4.2) or (4.3) holds, from (4.1)-(4.5),  $K = 0$  is finally obtained.  $\square$

I also proved the theorem from a different point of view.

**Proof.** This proof is explained with Figure 4.7. Figure 4.7(a) represents an object's surface, and Figure 4.7(b) represents a Gaussian sphere that corresponds to Figure 4.7(a). Vertical curves depicted in these figures represent folding curves. I locate  $p$  and  $r$  on the folding curve of the object's surface. I also locate  $s$  on one side of the folding curve, and  $q$  on the other side of the folding curve.  $p$ ,  $q$ ,  $r$  and  $s$  are located separately and do not overlap. I denote the points on the Gaussian sphere as  $p'$ ,  $q'$ ,  $r'$ ,  $s'$ , which correspond to the points on the object surface,  $p$ ,  $q$ ,  $r$ ,  $s$ .  $p'$  and  $r'$  will be located on the folding curve of the Gaussian sphere. From the definition of a local folding curve,  $q'$  and  $s'$  map onto the same side of a folding curve. The area of triangle  $prq$ ,  $psr$ , and  $p'r'q'$  will become positive; however, the area of triangle  $p's'r'$  becomes negative. Gaussian curvature  $K$  of  $p$  can be calculated from the limit taken by approaching  $q$ ,  $r$  and  $s$  to  $p$ .

$$K = \lim_{r, q \rightarrow p} \frac{\Delta p'r'q'}{\Delta prq} \geq 0 \quad (4.6)$$

$$K = \lim_{s, r \rightarrow p} \frac{\Delta p's'r'}{\Delta psr} \leq 0 \quad (4.7)$$

As a result, Gaussian curvature  $K$  at  $p$  will be 0. Even if the location of  $p'$  and  $r'$  is the opposite location to that shown in Figure 4.7(b), namely, even if  $p'$  is located to the left and  $r'$  is located to the right, I can also give a proof that is the same as this proof. Even if  $p$  or  $r$  is not a curve but a surface, I can also give a proof similar to this proof. In the case of  $p' = r'$ ,  $p' = q'$ ,  $p' = s'$ ,  $r' = q'$ ,  $r' = s'$  or  $q' = s'$ , I can give a proof more easily than this proof.  $\square$

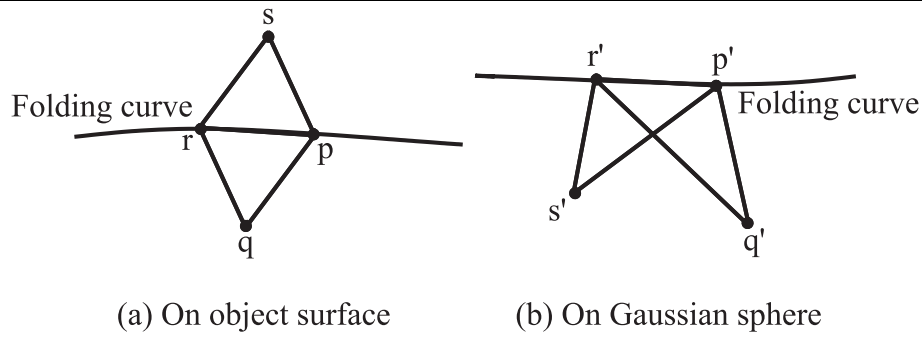


Figure 4.7: (a) Folding curve and 4 points on object surface, (b) folding curve and 4 points on Gaussian sphere mapped from (a).

A parabolic curve is a curve where Gaussian curvature is zero and Gaussian curvature of the object's surface does not change through rotation of the object. Therefore, I can conclude that the folding curve is intrinsic to an object and invariant from the viewer direction [Car76].

I obtain one set of DOP data for input data. However, one set of data is not enough for resolving the ambiguity in the B-B region; thus, I have to obtain extra data: I tilt (rotate) the object at a small angle and obtain an additional set of DOP values (Figure 4.8). I find identical points (corresponding points or matching points) of those two sets of data and compare the DOP values of the two sets of data at identical points in order to solve the ambiguity in the B-B region.

I will solve the ambiguity in the B-B region by comparing the data of the DOP of the object placed unrotated and that of the object rotated at a small angle. For comparison, I should find identical points (corresponding points) of two sets of DOP data. By adopting the geometrical property of the object's surface, I investigate an invariant property of the object's surface unchangeable through the object's rotation. I compare the DOP at two points where the invariant property on the surface matches, and disambiguate the ambiguity problem. I adopt the "folding point" (Section B.4) for this invariant property of the object's surface.

The Gaussian mapping of the B-B region of the object's surface onto the Gaussian sphere is depicted in Figure 4.5. The B-B region includes neither the occluding boundary nor the North Pole point, and is bounded only by the Brewster curve; thus, the folding curve always appears.

Because curvature is a property of a surface, it is an invariant value that is not changed by rotating the object. For this reason, considering curvatures for finding corresponding points is a suitable option. It is better to adopt a point where the curvature is zero rather than the

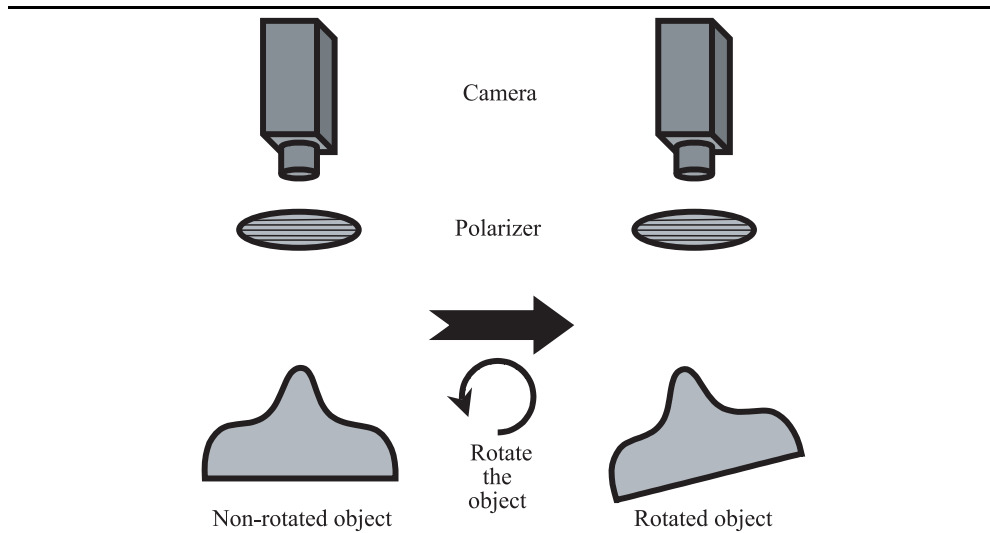


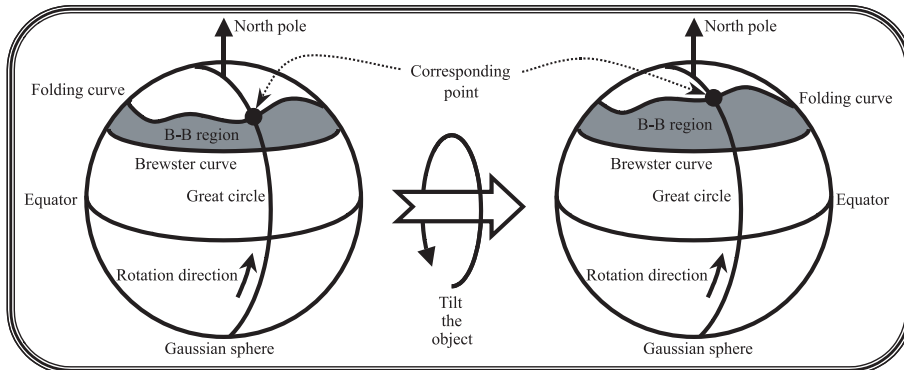
Figure 4.8: Object rotation.

curvature itself, because the curvature can be easily influenced by an error and has ambiguity. Therefore, I adopt folding curves. Adoption of folding curves is the most practical idea, because folding curves always appear in the B-B region.

I cannot determine the number of (local) folding curves that will appear in a closed region; however, I can state that the boundary of the region in the Gaussian sphere that is not the Brewster curve is always a (global) folding curve. Therefore, I utilize the boundary of the region of the Gaussian sphere mapped from the B-B region (global folding curve) for matching. Namely, if the B-B region is to the north of the Brewster curve, I utilize the northernmost folding curve for matching; and if the B-B region is to the south of the Brewster curve, I utilize the southernmost folding curve for matching.

However, there is a problem in matching two folding points. I can decide which folding curve corresponds to which folding curve, but I cannot decide which point on the folding curve corresponds to which point on the folding curve. Therefore, I define the corresponding point as the point where the folding curve and the great circle intersect (Figure 4.9). This great circle must be a cross-section between the Gaussian sphere and the plane that is parallel to the rotation direction of the object and includes the North Pole of the Gaussian sphere. The surface point that is mapped onto this great circle still maps onto this great circle after the object's rotation, thus enabling unique matching.

Summary:



or

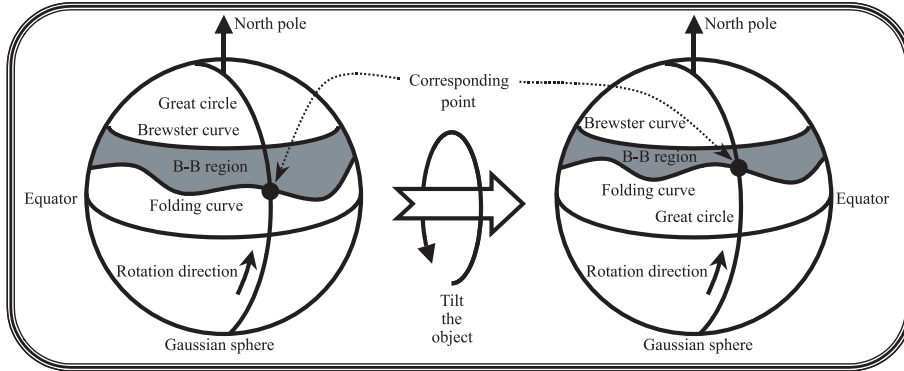


Figure 4.9: Corresponding point.

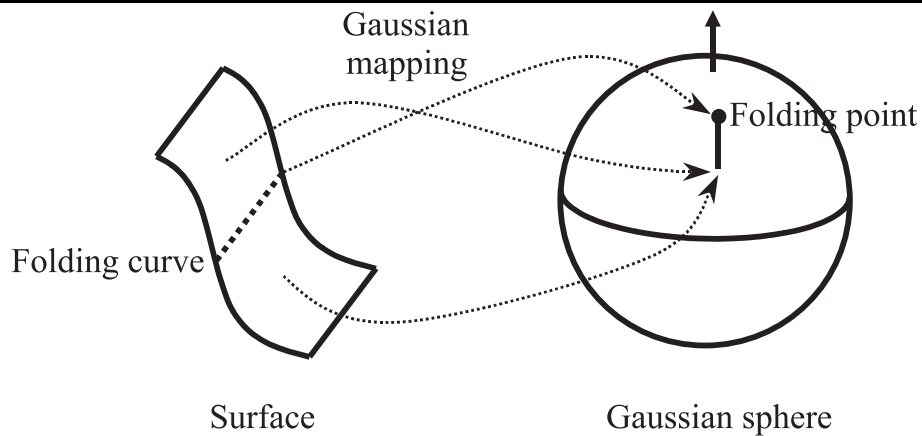


Figure 4.10: Gaussian mapping of slide-shaped surface.

---

1. If the B-B region is mapped onto the north of the Brewster curve, choose the northernmost point for the corresponding point that intersects the great circle; namely, choose the point where the DOP is minimum.
2. If the B-B region is mapped onto the south of the Brewster curve, choose the nearest point to the equator for the corresponding point that intersects the great circle; namely, choose the point where the DOP is minimum.

There exists one or two points where the DOP is minimum and where the folding curve and the great circle intersect. If there are two points, I can distinguish those points, because the azimuth angle  $\phi$  is in direct opposition; thus, there is no difficulty in matching.

My conclusion is that the point of the B-B region where the DOP is minimum and the surface normal lies along the rotation direction is the best corresponding point to adopt (Figure 4.9).

There is not always only one point of the surface that maps onto the corresponding point on the Gaussian sphere. For instance, there are several points that fit the above definition of corresponding point in the slide-shaped patch shown in Figure 4.10. However, my aim is a comparison of the value of DOP at two points, not matching at two points (see Section 4.5 for more detail). Many points exist on the surface that fit the above definition of corresponding point; however, the value of the DOP does not change even if I choose any corresponding point. Therefore, even though there are several corresponding points, the disambiguating process will not be disturbed.

## 4.5 Difference of Degree of Polarization

Finally, I describe the method used to resolve the ambiguity problem of the surface normal by comparing the DOP at the corresponding point of the nontilted object with that of the tilted object.

I regard the refractive index  $n$  as constant; thus, the DOP  $\rho$  is only a function of the zenith angle  $\theta$ . If the rotation angle is  $\delta\theta$ , the Taylor expansion of the DOP  $\rho(\theta + \delta\theta)$  around  $\theta$  will be;

$$\rho(\theta + \delta\theta) = \rho(\theta) + \rho'(\theta)\delta\theta + O((\delta\theta)^2) \quad . \quad (4.8)$$

Therefore, if  $\delta\theta$  is sufficiently small, the difference between two DOP values will be;

$$\rho(\theta + \delta\theta) - \rho(\theta) = \rho'(\theta)\delta\theta \quad . \quad (4.9)$$

The derivative of the DOP  $\rho$  by the zenith angle  $\theta$  is:

$$\frac{d\rho}{d\theta} = \frac{2 \sin \theta (n^2 - \sin^2 \theta - n^2 \sin^2 \theta) (2n^2 - \sin^2 \theta - n^2 \sin^2 \theta)}{\sqrt{n^2 - \sin^2 \theta} (n^2 - \sin^2 \theta - n^2 \sin^2 \theta + 2 \sin^4 \theta)^2} \quad . \quad (4.10)$$

The graph of the DOP is depicted in the lower half of Figure 4.11, and the graph of the derivative of the DOP is depicted in the upper half of Figure 4.11. The derivative of the DOP  $d\rho/d\theta$  is positive when  $0 < \theta < \theta_B$  and is negative when  $\theta_B < \theta \leq \pi/2$ .

The relationship between the rotation angle,  $\Delta\theta$ , the DOP of the nontilted object,  $\rho(\theta)$ , the DOP of the tilted object,  $\rho(\theta + \Delta\theta)$ , and the derivative of the DOP,  $\rho'(\theta)$ , will be:

$$\text{sgn}(\rho'(\theta)) = \frac{\text{sgn}(\rho(\theta + \Delta\theta) - \rho(\theta))}{\text{sgn}(\Delta\theta)} \quad , \quad (4.11)$$

where  $\text{sgn}(x)$  is a function which returns the sign of  $x$ .

In fact, the absolute value of the rotation angle is not needed; however, I assume that the rotation direction is known. Since the azimuth angle  $\phi$  has also already been determined, the sign of  $\Delta\theta$  can be determined. As a result, by calculating the sign of the difference of two DOP values at the corresponding point and by giving the sign of  $\Delta\theta$ , I can determine, by using (4.9), whether the zenith angle  $\theta$  in the B-B region is in the range of  $0 \leq \theta \leq \theta_B$  or of  $\theta_B \leq \theta \leq \pi/2$ .

Consequently, whether the zenith angle  $\theta$  in the B-B region is in the range of  $0^\circ \leq \theta \leq \theta_B$  or  $\theta_B \leq \theta \leq 90^\circ$  can be determined.

And also Figure 4.11 tells that the DOP  $\rho$  is an increasing function in the range of  $0^\circ \leq \theta \leq \theta_B$  and is a decreasing function in the range of  $\theta_B \leq \theta \leq 90^\circ$ . Namely, the correspondence between the DOP  $\rho$  and the zenith angle  $\theta$  is one-to-one in the range of  $0 \leq \theta \leq \theta_B$ , and is also one-to-one in the range of  $\theta_B \leq \theta \leq \pi/2$ . Therefore, if I simply determine that the

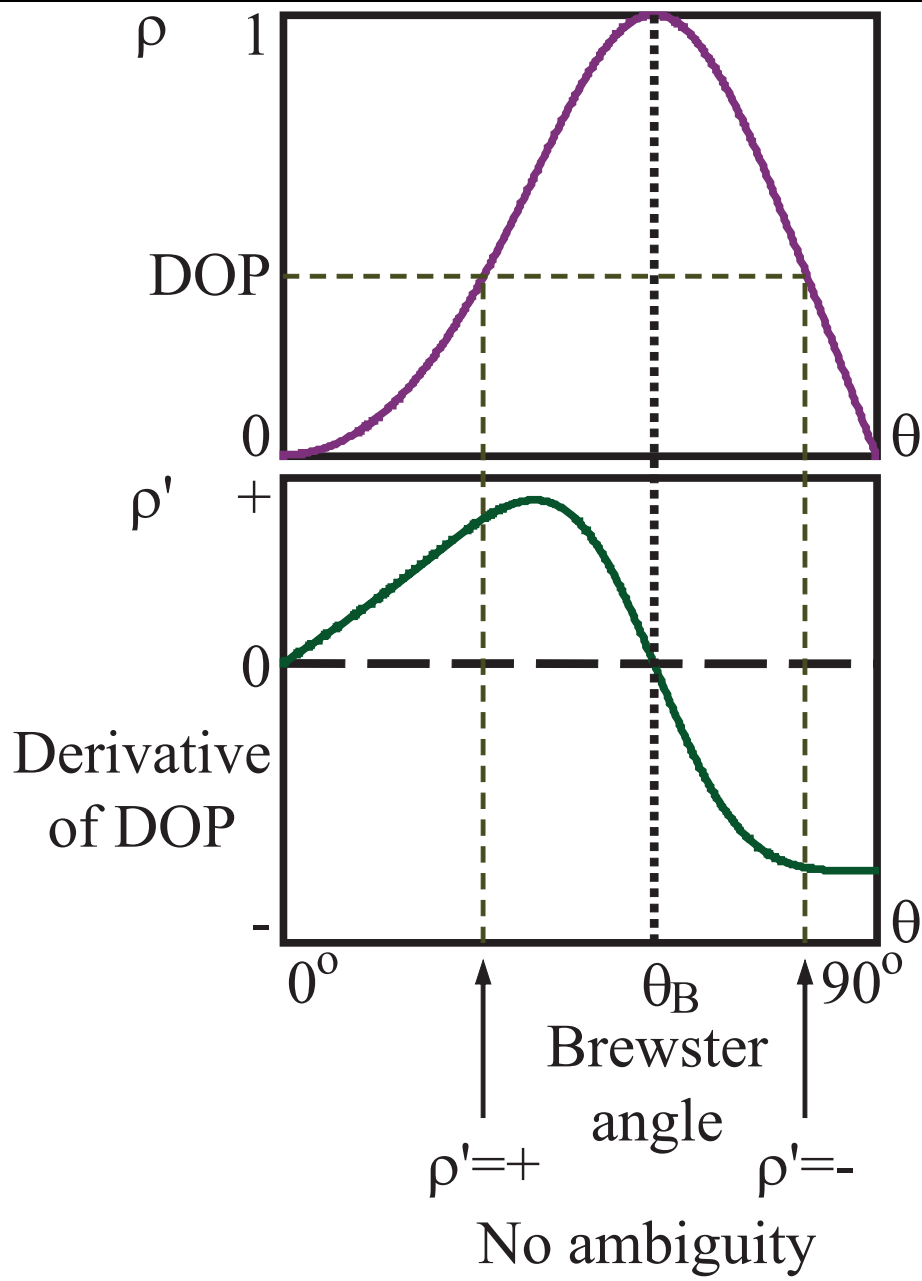


Figure 4.11: Graph of derivative of DOP ( $n = 1.5$ ).

zenith angle  $\theta$  in the B-B region is in the range of whether  $0 \leq \theta \leq \theta_B$  or  $\theta_B \leq \theta \leq \pi/2$  by (4.11), I can determine the zenith angle  $\theta$  uniquely from the value of the DOP  $\rho$ .

## 4.6 Summary

In this chapter, I have proposed a method for determining the shape of a transparent object by using a polarization filter. Surface normals are determined by using the polarization data. Because an algorithm that uses only one view results in ambiguities, polarization of a slightly tilted view is also employed.

I obtain two sets of data: One is from the object not tilted, and the other is from the object tilted at a small angle. I segment these data into regions with regard to the Brewster angle. I calculate the difference of the degree of polarization between these two sets of data at the corresponding point — the point where surface normal lies along the rotation direction and where the degree of polarization is minimum in the B-B region. From that difference, I determine the correct surface normal.

The purpose of the method described in this chapter is that same as the method described in Chapter 3. The purpose of these methods is to disambiguate the problem of the zenith angle  $\theta$ . By analyzing the reflected light from one direction in visible light domain, two possible zenith angles are produced; one is correct and the other is wrong. The first method described in Chapter 3 chose the correct angle by obtaining the polarization data of the thermal radiation of the object in infrared light domain from the same direction, while the second method described in this chapter (Chapter 4) chose the correct angle by obtaining another set of polarization data of the rotated object in visible light domain. There is no difference between the procedure of these two methods to produce two possible angles, thus, the two values themselves are the same using these two methods. The difference between the two methods is how to choose the correct angle.

The experimental setup to obtain polarization data is presented in Section 6.1.1. Implementation detail to obtain polarization data for the non-rotated object is presented in Section 6.2.1, and implementation detail to obtain polarization data for the rotated object is presented in Section 6.2.3. Experimental results of applying the method proposed in this chapter are presented in Section 6.3.2.

Target objects for the method proposed in this chapter must obey the assumptions suggested in Section 4.2. I will discuss what kinds of objects are measurable and what kinds of objects are not measurable in more details below.

- The method of this chapter also assumes that internal interreflection does not occur. Therefore, the measurable and unmeasurable objects of this method are similar to those

of the method of Chapter 3. The third method described in Chapter 5 solves the problem of internal interreflection. The method of this chapter as well as that of Chapter 3 is applicable to not only transparent objects but also translucent objects, opaque objects, metallic objects, hollow transparent objects, and birefringent transparent objects. Since the method assumes that the camera observes the specular reflection of the object's surface, the method cannot be applied to perfect diffuse objects (Lambertian surfaces) and perfect absorbers. The method also assumes that the object's surface is optically smooth; thus, the method is only applicable to perfect specular objects.

If the object's shape is too complex and the interference of the internal interreflection is too strong, the method provides an erroneous result. The method can be applied to shallow concave objects because some of these objects still obey the assumption that the light reflected at the surface only once is observed. However, the method cannot be applied to deep concave objects because some of these objects violate this assumption and cause multiple reflection at the concave part. If the object's surface has a dimple (concavity in convexity), the method cannot be applied since the azimuth angle  $\phi$  is not estimated by the method shown in Section 2.1.1.

- The method assumes that the object's surface must be  $C^2$  surface (a geometrically smooth surface), because the curvature as well as the surface normal must be calculated. This assumption is different from that used in Chapter 3; Chapter 3 assumed that the object's surface must be  $C^1$  surface because the surface normal must be calculated. If the object has a discontinuous part, the method cannot be applied. If the object has a  $C^0$  surface (continuous surface), the method cannot be applied because the surface normal and the curvature cannot be calculated. Theoretically, the method cannot be applied to  $C^1$  surface (geometrically smooth surface but not  $C^2$ ), because the curvature cannot be calculated at the area where it is not  $C^2$ . However, in practice, some of the  $C^1$  object's shape can be estimated by the method proposed in this chapter.
- The method assumes that the refractive index of the object is known. Therefore, if the refractive index is unknown, the object's shape cannot be estimated. However, the method can be applied to an object whose refractive index varies from part to part if such variation of the refractive index is known.
- The experimental setup shown in Section 6.1.1 cannot obtain the polarization data in realtime; however, some measurement systems exist that can obtain the polarization data in realtime [WMPA97, FTA+98, HC02]. By observing the object from two directions by two realtime measurement systems, two sets of polarization data of the object observed from two different viewing directions are obtained. Therefore, if I update the

measurement system into a realtime one, the method can estimate the shape of deforming objects, such as liquid, jelly, or a soap bubble.

To summarize: Transparent objects with optically smooth surfaces and  $C^2$  closed surfaces whose refractive index is known and have no deep concave part are measurable, though there will be some noise due to internal interreflection. Also, translucent objects, opaque objects, metallic objects, hollow transparent objects, and birefringent transparent objects are measurable. Some objects that have a shallow concave part are measurable. Some of the objects whose surface is  $C^1$ , geometrically smooth objects, are measurable. Objects whose refractive index varies from part to part are measurable if we know the refractive index in any part of the object. Objects that deform from time to time, such as liquid, jelly, or soap bubbles, are measurable, by using a realtime measurement system. Objects that melt when heated up to 30–40 degrees Celcius, such as ice or jelly, are measurable.

The following are the examples of the objects that are unmeasurable by the method proposed in this chapter:

- Objects that have optically rough surfaces, such as perfect diffuse objects, are unmeasurable.
- Objects that have deep concave parts or dimples are unmeasurable.
- Objects that have geometrically non-smooth parts, such as a cube, a diamond, or a pyramid, are unmeasurable.
- Objects whose refractive index is unknown are unmeasurable.

## CHAPTER 5

# SHAPE ESTIMATION OF TRANSPARENT OBJECTS BY USING POLARIZATION RAYTRACING

In this chapter, I introduce the method of estimating the shape by polarization raytracing.

### 5.1 Introduction

The two methods described in Section 3 and Section 4 focused on solving the ambiguity problem. However, these methods did not focus on solving the internal interreflection problem; they only considered the reflection; they did not consider the transmission. The method in this chapter focuses on solving this internal interreflection problem by considering both reflection and transmission.

A transparent object not only causes reflection but also causes transmission. The light ray that penetrates the transparent object causes multiple internal interreflections inside it. These interreflections must be considered in estimating the surface shape of transparent objects precisely.

The trajectory of the light ray can be computed by a conventional raytracing method, which is often used in the field of computer graphics to render transparent objects realistically. Also, the polarization state of the light can be computed by a method called Mueller calculus, which is described in Section 2.2. In this thesis, the combination technique of conventional raytracing and Mueller calculus is expressed as the polarization raytracing method. In this chapter, I propose a method to estimate the surface shape of a transparent object by solving the inverse problem of the polarization raytracing method. Specifically, the method iteratively computes the surface shape by minimizing the difference between the obtained polarization

data and the rendered polarization data calculated by the polarization raytracing method.

In this thesis, a forward-facing surface of the transparent object is denoted as a frontal surface and an object surface facing away from the camera is denoted as a rear surface. The proposed method estimates the shape of the frontal surface by using polarization raytracing when the refractive index and the rear surface are given.

First, Section 5.2 shows some assumptions for the method. Next, Section 5.3 explains the method to compute the surface shape by solving the inverse problem of polarization raytracing method.

## 5.2 Assumptions

There are several assumptions I use to successfully apply the method:

- 1 The object is observed as an orthographic projection to the image plane of the camera.
- 2 The object is transparent and solid.
- 3 The refractive index is known and constant for any part of the object.
- 4 The object's surface is optically smooth (not microscopically rough).
- 5 The object's surface is geometrically smooth and closed ( $C^1$  surface).
- 6 No self-occlusion exists. There is no "jump" in the height of the object surface.
- 7 The entire frontal surface is included in the camera field of view.
- 8 The rear surface shape is known.
- 9 The initial value of the frontal surface is given a priori.
- 10 The light that illuminates the frontal surface is unpolarized and uniform. Also, the light that illuminates the rear surface is unpolarized and uniform. Both intensities are known.

Assumption 1 is not the limitation of the method but of the polarizer. The polarizer shows the best performance if the light strikes the polarizer orthogonally. The method itself can be improved for perspective projection.

In fact, assumption 2 is not mandatory. The method is also effective for opaque objects that have a highly specular surface. Also, by using a realtime capture system [WMPA97, FTA+98, HC02], the method can also be applied to non-solid objects.

Assumptions 5 and 6 imply that the surface normal can be calculated by differentiating the height of the object's surface.

Initial value, referred in assumption 9, can be given, for example, by a human operator, or by the methods described in Chapter 3 or Chapter 4.

### 5.3 Inverse Polarization Raytracing

In this section, I introduce the proposed method for estimating the frontal surface shape of a transparent object using the DOP (degree of polarization) and the POI (plane of incidence) angle as inputs under the assumption that the refractive index and the backward-facing surface shape are given. Details of numerical algorithms and mathematics are shown in the literature [PTVF92, CH53].

I denote the input polarization data as  $I_E$ . Polarization data are represented as an image (2-dimensionally distributed data) where the DOP and POI angle are set for each pixel. The polarization raytracing explained in Section 2.2 can render the polarization data from the shape of transparent object. I denote such rendered polarization images as  $I_R$ . The shape of transparent objects is represented as the height  $H$ , set for each pixel. Heights partially differentiated by  $x$  and  $y$  are called gradient, and are represented as  $p$  and  $q$ , respectively:

$$p = H_x = \frac{\partial H}{\partial x}, \quad q = H_y = \frac{\partial H}{\partial y} \quad . \quad (5.1)$$

Surface normal  $\mathbf{n} = (-p, -q, 1)^T$  is represented by these gradients. Note that  $A_x$  can be discretized, for example, as follows:

$$A_x(x, y) = \frac{1}{2} (A(x+1, y) - A(x-1, y)) \quad . \quad (5.2)$$

The rendered polarization image  $I_R$  depends upon the height and surface normal, so it can be represented as  $I_R(H, p, q)$ . The problem is finding the best values to reconstruct a surface  $H$  that satisfies the following equation:

$$I_E = I_R(H, p, q) \quad . \quad (5.3)$$

I call this equation the ‘‘polarization raytracing equation’’ from the analogy of ‘‘image irradiance equation’’ used in the shape-from-shading problem.

A straightforward definition of the cost function, which I want to minimize, can be as follows:

$$\iint E_1(x, y) dx dy \quad , \quad (5.4)$$

where,

$$E_1 = (I_E - I_R(H, p, q))^2 \quad . \quad (5.5)$$

I will sometimes omit the variables  $(x, y)$  in the subsequent discussions for the simplicity of descriptions.  $I_R$  depends upon  $p, q,$  and  $H$ , while  $p, q,$  and  $H$  depend upon each other with Equation (5.1). Therefore, the cost function must be modified as follows:

$$\iint (\lambda E_1 + E_2) dx dy \quad , \quad (5.6)$$

where,

$$E_2 = (H_x - p)^2 + (H_y - q)^2 \quad . \quad (5.7)$$

$\lambda$  is Lagrange undetermined multiplier.

Euler equation (Euler-Lagrange differential equation) which minimize the equation,

$$\iint F(u, u_x, u_y) dx dy \quad , \quad (5.8)$$

will be:

$$F_u - \frac{\partial F_{u_x}}{\partial x} - \frac{\partial F_{u_y}}{\partial y} = 0 \quad . \quad (5.9)$$

Applying the solution method described as Equations (5.8)(5.9) into Equation (5.6) in order to solve for  $p$  gives the following Euler equation:

$$p = H_x - \frac{\lambda}{2} \frac{\partial E_1}{\partial p} \quad . \quad (5.10)$$

Also, for  $q$ , the Euler equation can be derived as:

$$q = H_y - \frac{\lambda}{2} \frac{\partial E_1}{\partial q} \quad . \quad (5.11)$$

As for  $H$ , the Euler equation, which minimizes Equation (5.6), is derived as follows:

$$H_{xx} + H_{yy} - p_x - q_y - \frac{\lambda}{2} \frac{\partial E_1}{\partial H} = 0 \quad . \quad (5.12)$$

Here,  $H_{xx}$  and  $H_{yy}$  can be discretized as follows:

$$H_{xx} = H(x+1, y) + H(x-1, y) - 2H(x, y) \quad (5.13)$$

$$H_{yy} = H(x, y+1) + H(x, y-1) - 2H(x, y) \quad . \quad (5.14)$$

Thus, substituting Equations (5.13)(5.14) into Equation (5.12) produces the following equation:

$$H = \bar{H} - \frac{1}{4} (p_x + q_y) - \frac{\lambda}{8} \frac{\partial E_1}{\partial H} \quad , \quad (5.15)$$

where  $\bar{H}$  is a 4-neighbor average of  $H$ :

$$\bar{H} = \frac{1}{4} (H(x+1, y) + H(x-1, y) + H(x, y+1) + H(x, y-1)) \quad . \quad (5.16)$$

Each of the above Equations (5.10)(5.11)(5.15) can be decomposed into two steps:

$$p \leftarrow H_x \quad (5.17)$$

$$p \leftarrow p - \lambda_1 \nabla E_1 \quad (5.18)$$

$$q \leftarrow H_y \quad (5.19)$$

$$q \leftarrow q - \lambda_2 \nabla E_1 \quad (5.20)$$

$$H \leftarrow \bar{H} - \frac{1}{4} (p_x + q_y) \quad (5.21)$$

$$H \leftarrow H - \lambda_3 \nabla E_1 \quad (5.22)$$

Here,  $\lambda_1$ ,  $\lambda_2$ , and  $\lambda_3$  are scalar values that are determined for each pixel and for each iteration step.  $\nabla$  in Equations (5.18)(5.20)(5.22) are,

$$\frac{\partial}{\partial p}, \quad \frac{\partial}{\partial q}, \quad \frac{\partial}{\partial H}, \quad (5.23)$$

respectively.

First, I set initial values of the shape  $H$  for each point of frontal surface. Next,  $p$  and  $q$  are calculated by Equations (5.17)(5.19). Then, I solve Equations (5.18)(5.20).  $\lambda_1$  and  $\lambda_2$  should be optimal values; thus, I use Brent's method to determine  $\lambda_1$  and  $\lambda_2$ , which minimize the error function  $E_1$ . After computing  $p$  and  $q$  at every pixel, I solve Equation (5.21) by the relaxation method to determine the height  $H$ . Ikeuchi solved the relaxation problem by using the Jacobi method [Ike84], while Horn [Hor90] solved it by means of the successive over-relaxation method. I use the alternating-direction implicit method to increase the speed of computation.

Also, I do not choose to solve Equation (5.22) by Brent's method because the error function  $E_1$  depends upon the change of surface normal rather than on the change of height. Another reason is that the error function  $E_1$  changes smoothly when the surface normal changes, but it does not change smoothly when the height changes. This fact was empirically proved in the preliminary experiments.

To conclude, the frontal surface shape of a transparent object is estimated by an iterative computation, where each step of the iteration solves Equations (5.17)–(5.21), and the iteration stops when the Equation (5.4) is minimized. There are two reasons why I use Equations (5.17)–(5.21) instead of Equations (5.10)–(5.15): (1) If I solve Equations (5.10)–(5.15) simultaneously by setting an arbitrary value  $\lambda$ , a parameter tuning problem will occur where  $\lambda$  must be set to an optimal value in order to solve these equations stably; (2) I can apply adequate numerical algorithms for each of the Equations (5.17)–(5.21).

## 5.4 Summary

In this chapter, I have proposed a method for estimating the surface shape of transparent objects by minimizing the difference between the input polarization data taken by observing the transparent object and the computed polarization data rendered by the polarization raytracing method. It is impossible to analytically solve the inverse problem of polarization raytracing; thus, I estimated the transparent object shape by an iterative computation.

The purpose of the method in Chapter 3 and Chapter 4 is the same; they concentrated on disambiguating the problem of the zenith angle  $\theta$ . The purpose of the method in this chapter is different from the above two methods; the method in this chapter concentrated on considering the phenomenon of internal interreflection. Two methods in Chapter 3 and Chapter 4 assumed that the camera observes the light that is reflected at the object surface only once, and considered neither the transmission nor the multiple reflection occurring between surface patches of the transparent object. Therefore, the estimation results of these methods are polluted by some noise originating from the internal interreflection. In this chapter, the proposed method produces more precise estimation results than the estimation results produced by the above mentioned two methods, due to the consideration of the internal interreflection.

Experimental setup to obtain polarization data is presented in Section 6.1.1. Implementation detail to obtain polarization data for the method proposed in this chapter is presented in Section 6.2.1 and Section 6.2.4. Experimental results of applying the method proposed in this chapter are presented in Section 6.3.3.

Target objects for the method proposed in this chapter must obey the assumptions suggested in Section 5.2. I will discuss what kind of objects are measurable and what kind of objects are not measurable in more detail below.

- The method considers internal interreflection, which is different from the method proposed in Chapter 3 and Chapter 4. External interreflection is still not considered; if multiple reflections occur between the transparent object and the experimental setup, the measurement result will be polluted by some noise. Therefore, the object and the light sources are placed far apart, and the object and the camera are placed far apart.

Considering internal interreflection seems to be a merit of this method; this is true in the sense of increased precision, but it is not true in the sense of increased applicability. Since the method analyzes multiple transmissions and reflections inside the object, the method strongly depends on the internal structure of the target object. Therefore, the method is applicable only to transparent objects, and is not applicable to translucent objects, opaque objects, metallic objects, hollow transparent objects, and birefringent transparent objects. The method also assumes that the object's surface is optically

smooth; thus, the method is only applicable to perfect specular objects.

Since the method considers not only the multiple reflections occurring inside the transparent object but also the multiple reflections occurring outside the transparent object between the surface patches of the object's surface, the method is applicable not only to shallow concave objects but also to deep concave objects and objects that have dimple (concavity in convexity) areas.

- The method assumes that the object surface must be  $C^1$  surface (a geometrically smooth surface), because the surface normal must be calculated. If the object has a discontinuous part, the method cannot be applied. Theoretically, the method cannot be applied to  $C^0$  surface (continuous surface), because the surface normal cannot be calculated at the non-smooth area. However, in practice, some of the  $C^0$  object's shape can be estimated by the method proposed in this chapter.
- The method assumes that the refractive index of the object is known. Therefore, if the refractive index is unknown, the object's shape cannot be estimated.

A birefringent transparent object is an object whose refractive index of the object slightly differs for each direction. The method is sensitive to such birefringency of the object, because birefringency greatly changes the polarization state of transmitted light, while reflected light is not influenced by birefringency. Some crystals and objects that have a photoelastic effect have such birefringency. Photoelastic effect is a phenomenon that produces birefringency, which is caused by the deformation inside the object by high pressure.

Though the method is sensitive to the birefringency, the method can be applied to such birefringent transparent objects if the refractive index for each direction and at each part inside the object is known.

- The experimental setup shown in Section 6.1.1 cannot obtain the polarization data in realtime; however, measurement systems exist that can obtain the polarization data in realtime [WMPA97, FTA+98, HC02]. Therefore, if I update the measurement system into a realtime one, the method can estimate the shape of deforming objects, such as liquid, jelly, or a soap bubble.
- The method of this chapter assumes the rear surface shape is known. Most of the artificial transparent objects have a planar base that enables them to stand by themselves; thus, this assumption is effective in many cases. However, not all objects agree with such conditions; the method cannot estimate the frontal surface shape of the transparent object whose rear surface shape is unknown. Therefore, future work will be to develop

a method that can measure the rear surface shape at the same time as well as the frontal surface shape. Estimating both frontal surface shape and rear surface shape by observing the transparent object from one direction is considered to be impossible, and I have confirmed in the preliminary experiment that it is impossible. In order to solve this problem, I have to develop a method to estimate the shape of the transparent object by observing it from multiple directions.

- The method of this chapter needs an initial value of the frontal surface. The method successfully estimates the shape of the object by providing a proper initial shape. If a proper initial shape is not provided, then the iteration computation will be stuck to the local minimum and produces a wrong shape. The initial value can be provided by the methods proposed in Chapter 3 and Chapter 4 as well as by a human operator.
- The method requires knowing the illumination distribution that surrounds the target object. If the information of the illumination distribution is insufficient, the method provides an erroneous result. The experimental setup shown in Section 6.1.1 produces uniform unpolarized illumination distribution except for the direction where the camera is placed. The object is set on top of a black pipe, which makes the light illuminating the rear surface of the object uniform and unpolarized. The relative intensity of the light that is illuminating the frontal surface and the light that is illuminating the rear surface is obtained by the procedure presented in Section 6.2.4. The procedure to estimate the illumination distribution presented in Section 6.2.4 is an ad hoc one, and a more sophisticated procedure to estimate the correct illumination distribution will be presented in future work.

To summarize: Transparent objects with optically smooth surface and  $C^1$  closed surface whose refractive index and rear surface shape is known and where illumination distribution is known are measurable from a proper initial surface shape. Objects that have not only a shallow concave part but also a deep concave part are measurable. Some of the objects whose surface is  $C^0$ , such as a cube, diamond, or pyramid, are measurable. Objects whose refractive index varies from part to part are measurable if we know the refractive index in any part of the object. Objects that deform time to time, such as liquid, jelly, or soap bubbles, are measurable, by using a realtime measurement system. Objects that melt when heated up to 30–40 degrees Celcius, such as ice or jelly, are measurable.

The following are examples of objects that are unmeasurable by the method proposed in this chapter:

- Translucent objects and hollow transparent objects are unmeasurable.
- Objects that have optically rough surfaces, such as frosted glass, are unmeasurable;

- Objects that have a discontinuous part are unmeasurable.
- Objects whose refractive index is unknown are unmeasurable.
- Objects whose rear surface shape is unknown are unmeasurable.
- Objects are unmeasurable if an appropriate initial frontal surface shape is not provided.
- Objects are unmeasurable if illumination distribution is not provided.

## CHAPTER 6

# EVALUATIONS

In this chapter, I present some experimental results and evaluate the effectiveness of three proposed methods.

- Section 6.1 explains the experimental setup:
  - Section 6.1.1 explains the experimental setup that obtains the polarization data of visible light.
  - Section 6.1.2 explains the experimental setup that obtains the polarization data of infrared light.
- Section 6.2 explains the measurement procedures:
  - Section 6.2.1 explains the procedure for measuring a non-rotated object in a visible light domain.
  - Section 6.2.2 explains the procedure for measuring the polarization data of infrared light.
  - Section 6.2.3 explains the procedure for measuring a rotated object.
  - Section 6.2.4 explains the procedure for preprocessing before applying the third method.
- Section 6.3 explains the experimental results:
  - Section 6.3.1 shows the measurement results of the first method, which uses thermal radiation. The results of measurements of a spherical object and shellfish-shaped object are presented.

- Section 6.3.2 shows the measurement results of the second method, which uses differential geometry. First, some simulation results are presented, and then the results of measuring a hemispherical object, a heart-shaped object, a bell-shaped object, and a mountain-shaped object are presented.
- Section 6.3.3 shows the measurement results of the third method, which uses polarization raytracing. First, an example of an image rendered by polarization raytracing is presented. Then some simulation results are presented. Finally, the results of measuring a hemispherical object, a bell-shaped object, jelly, and a heart-shaped object are presented.

## 6.1 Experimental Setup

### 6.1.1 Experimental Setup of Visible Light

Figure 6.1 represents our experimental setup, which I named “Cocon”, for obtaining the polarization data in a visible light domain. The target object is set inside the center of the plastic sphere whose diameter is 35cm. This plastic sphere is illuminated by 36 incandescent lamps. These 36 light sources are almost uniformly distributed spatially around the plastic sphere by the geodesic dome. This geodesic dome, originally developed by Ikeuchi and Nayar [SNI90, Nay91, KI93], is a polyhedron generated by a 2nd order geodesation operation of an icosahedron. This dome has 42 vertices, 80 faces, and 120 edges; however, there are no triangles in the bottom part of the actual setup in order to support the geodesic dome. Later, Debevec et al. [DWT+02] developed a similar setup called “Light Stage” to sample the appearance of a human face under various illumination distributions. The plastic sphere diffuses the light that comes from the light sources, and it behaves as a spherical light source, which is located at the center of the sphere, and which illuminates the target object from every direction. Because the surface reflection occurs only when the reflecting and incident angles are the same, it is better to illuminate an object from all directions in order to observe surface reflections over the entire object’s surface. The target object is observed by a monochrome camera from the top of the plastic sphere, which has a hole on the top. A linear polarizer is set in front of the camera. The camera and light sources are fixed.

When the light of an incandescent lamp penetrates the white plastic diffuser, the light will be unpolarized while randomly scattered inside the diffuser. The distance between the diffuser and the object is large enough compared with the size of the object, thus the observed light reflected at the object’s surface originally comes from the inner surface of the diffuser with same emitting direction as the surface normal of the diffuser. For this emitting angle, the light does not polarize [BW59]. Therefore, this spherical diffuser provides an unpolarized light.

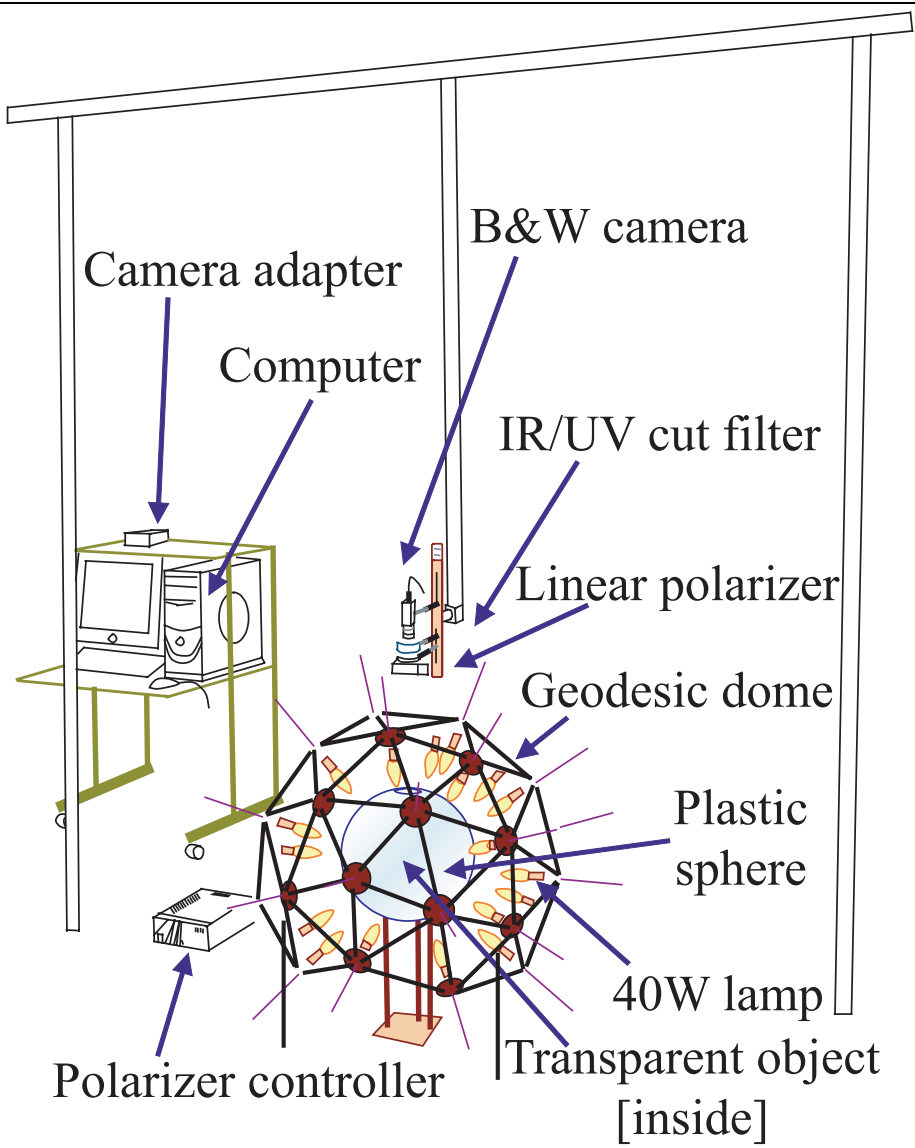


Figure 6.1: Experimental setup for visible light.

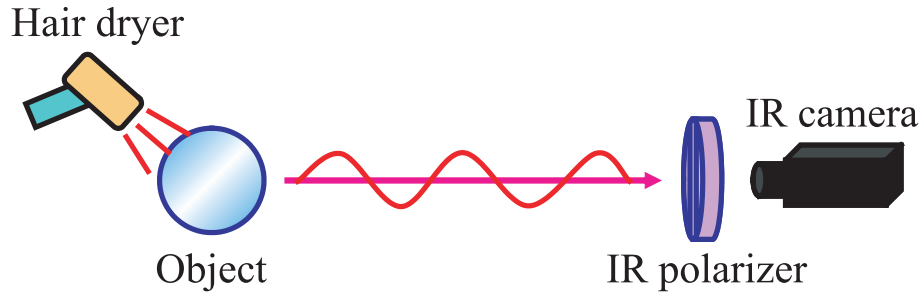


Figure 6.2: Experimental setup for infrared light.

## 6.1.2 Experimental Setup of Infrared Light

Figure 6.2 shows the apparatus for the infrared light. Given that the infrared light is thermal radiation from a body and is not a reflection component, I do not use any light source. Any object emits infrared light. However, at room temperature, the amount of infrared light emitted from the object in 3-5  $\mu\text{m}$  is relatively small, and contains infrared light emitted from the air. This makes the measurement of  $I_{\text{max}}$  and  $I_{\text{min}}$  very sensitive to noise. Therefore, I increase the temperature of the object to 30-40 degrees Celsius, and subtract that from the air temperature to obtain the amount of infrared light emitted solely from the object.

In order to increase the temperature of the object, I use a hair dryer to blow heated air over it. I also employ an infrared filter and an IR-CCD camera in 3-5  $\mu\text{m}$ . The IR-CCD camera determines an appropriate gain in order to map the temperature range onto a 256 gray level. Therefore, a measured intensity is converted to a temperature. In order to determine the degree of polarization, I convert the measured temperature into intensity using Equation (3.2).

## 6.2 Measurement

### 6.2.1 Measurement of a Non-rotated Object in a Visible Light Domain

A transparent object reflects and transmits light in a complex manner causing multiple internal interreflections that interfere with the observations. I set the object on a black pipe to block the light coming from behind the object; however, some internal interreflection still occurs. The internal interreflection lowers the degree of polarization. To overcome it, I subtract an unpolarized light from the input data and increase the degree of polarization. Since I do not know the information of the internal interreflection, I assume that the unpolarized and uniform light caused by internal interreflection is added to the light that is directly reflected from the

object surface only once. This assumption is not always true for each point on an object's surface, but I expect that this assumption statistically holds for sets of many points on the object's surface. I assume that the object is a closed, smooth object; thus, the Brewster angle will always appear. Therefore, the maximum value of the degree of polarization must be "1." I choose a certain number of points where the DOP (degree of polarization) is high, and estimate the subtraction value as the average value that makes the DOP of each chosen point be "1." This modification raises the maximum DOP of raw data to 1. The modified DOP  $\rho'$  is calculated by the following equation, which is derived by modifying (2.5):

$$\rho' = \frac{I_{\max} - I_{\min}}{I_{\max} + I_{\min} - u} \quad (6.1)$$

where  $u/2$  is the intensity of the estimated unpolarized light.  $u$  is estimated by setting  $\rho'$  as 1 for the chosen surface points.

Three images by rotating the polarizer are enough for calculating the polarization state of the light. However, I obtain four images of an object by rotating the polarization filter at 0, 45, 90, and 135 degrees to avoid the noise. Variance of intensity at each pixel can be seen in these four images. By using the least-squares minimization, I fit a sinusoidal curve to those intensities and then determine the maximum and minimum intensities,  $I_{\max}$  and  $I_{\min}$ . From those values, I determine two possible surface normals by using the algorithm.

## 6.2.2 Measurement of Thermal Radiation

For the infrared measurement, I heat the object to a temperature of 30-40 degrees Celsius by using a hair dryer for a certain period. Once equilibrium in the heat exchange is achieved, I use the same procedure, rotating the polarization filters and obtaining a sequence of images, as I did in the visible light measurement. Here, the maximum and minimum correspond to  $T_{\max}$  and  $T_{\min}$ ; I convert them to  $I_{\max}$  and  $I_{\min}$  as appropriate, then obtain the DOP.

After the measurements in infrared and visible light, I compare those data at each pixel. For alignment, I use two calibration points around the object; by extracting these two points in both image sequences, I can align the two measurements. At each pixel, measurement in visible light provides two solutions. Then, from the DOP in infrared measurement, I can choose one of the solutions; it is determined whether the obtained DOP in infrared light is smaller or larger than the infrared DOP at the Brewster angle.

## 6.2.3 Measurement of Rotated Object

After applying this measurement to the nontilted object, I apply the same measurement to the tilted object and obtain the DOP of this second view. A proper rotation direction is provided

by a human operator because, on the Gaussian sphere, the great circle must intersect the B-B region to solve the ambiguity problem.

I applied the “region growing” method [GW93] for Brewster segmentation. Initial values for the “region growing” method are given by the human operator. Since the “1” DOP cannot be observed in any case, I therefore segment the regions by a closed curve of the maximum DOP. I call a curve of the maximum DOP a pseudo-Brewster curve. A folding curve also exists in the pseudo-B-B region — a region bounded by a pseudo-Brewster curve. Consequently, the segmentation is still useful not only for the Brewster curve, but also for the pseudo-Brewster curve.

I compare those two sets of data at each corresponding point. To determine the corresponding points of the two sets of data, I first classify the regions generated by separating the polarization data with regard to the Brewster angle into three classes: the B-E region, the B-N region, and the B-B region. Then, I detect a minimum value of the DOP in each B-B region whose surface normal has the same orientation as the rotating direction. Finally, the difference value of the DOP in those two corresponding points solves the ambiguity problem of the angle; as a result, I obtain the correct incident angle of the object’s surface.

## **6.2.4 Measurement of Multiple Internal Interreflection**

Input data is the raw polarization data obtained by the experimental setup shown in Section 6.1.1. No modification is done to the obtained polarization data as is done in Section 6.2.1. The object is viewed from one direction by observing the visible light.

My third method using polarization raytracing needs the illumination distribution to be known. The experimental setup, shown in Figure 6.1, produces a uniform illumination distribution thanks to the optical diffuser and the geodesic dome. Before applying the proposed method, I checked the uniformity of the illumination distribution, and I concluded that the illumination distribution is sufficiently uniform except for the hole on top of the sphere. I have also checked that the illumination distribution is unpolarized. In this thesis, I applied my algorithm by assuming the illumination distribution is uniform and unpolarized. Considering the hole on top of the sphere will be my future work.

As I said in Section 6.2.1, I avoid the light coming from behind the object by a black pipe. In this thesis, I denote such light coming from behind the object as “background radiation”. The preliminary experiment showed that background radiation cannot be ignored. Fortunately, the background radiation was found to be uniform and unpolarized in the preliminary experiment. Therefore, I computed the polarization raytracing algorithm by considering the background radiation, assuming that it is uniform and unpolarized with its intensity known. However, the problem is discovering the intensity of the background radiation. Determining

its intensity directly from observation is impossible, because I should put the camera between the object and the pipe to observe the intensity of the pipe when the object is settled on the pipe. Luckily, the intensity of the background radiation can be determined indirectly from observation: (1)First, I observe the object whose shape is known and obtain the polarization data of the object, (2)next, I compute the polarization data by using polarization raytracing where the intensity of the background radiation is set to a certain value, (3)then, compare the computed polarization data and the obtained polarization data and check whether the difference between these polarization data is sufficiently small. By changing the value of the intensity, I can find the value where the difference will be the minimum. First, I calculate the intensity from observing a hemispherical acrylic transparent object, whose refractive index is 1.5 and diameter is 3cm. I use this intensity value also for calculating the shape of the objects which are not the hemispherical object.

## **6.3 Experimental Results**

### **6.3.1 Experimental Results of Thermal Radiation Method**

This section shows the experimental results of the first method, which uses thermal radiation. Section 6.3.1 provides the result of measuring a spherical object and Section 6.3.1 provides the of measuring a shellfish-shaped object.

#### **Experiments Using a Spherical Object**

In order to determine the accuracy of the system, I use an acrylic sphere having a refractive index of 1.5 and a diameter of 50mm. Figure 6.3 shows the error characteristics from the observed measurement. The horizontal axis is the emitting angle and the vertical axis denotes the measurement errors. In the figure, the dotted straight line denotes the case without any measurement errors.

From this experiment, except around the area of small angles, the measurement error is small and I can achieve high accuracy in measurement.

One of the reasons for the relatively noisy data around the smaller angles is that the spherical diffuser has a hole in its top portion, and the object does not receive light from that area. Another reason is that the derivative of the degree of polarization is close to zero where the incident angle is near  $0^\circ$ , and is less stable for determining the incident angle from the degree of polarization.

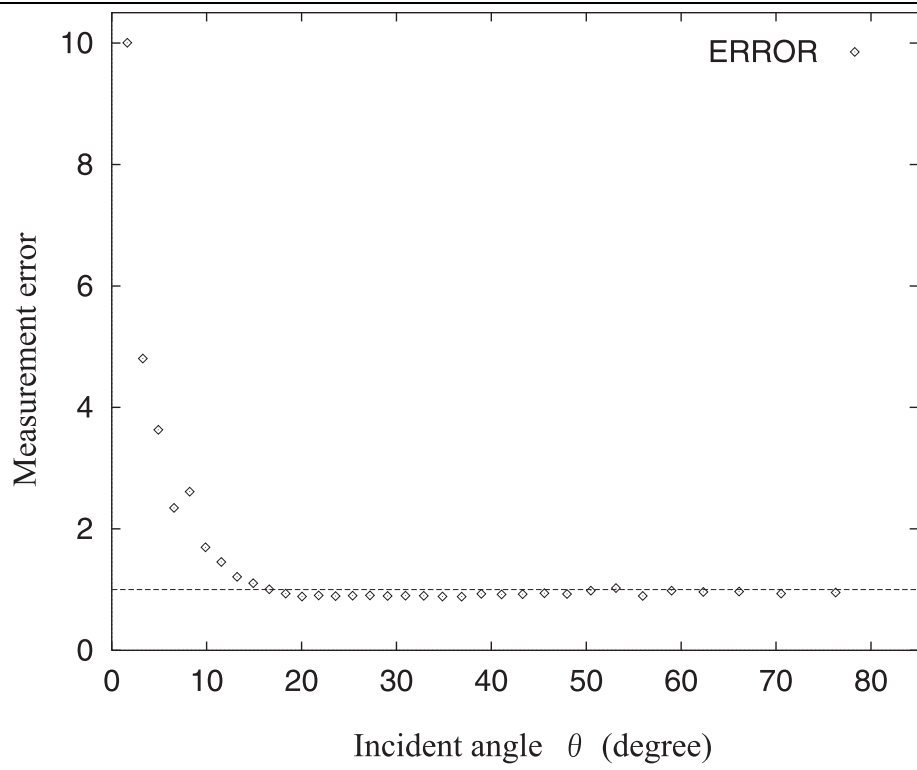
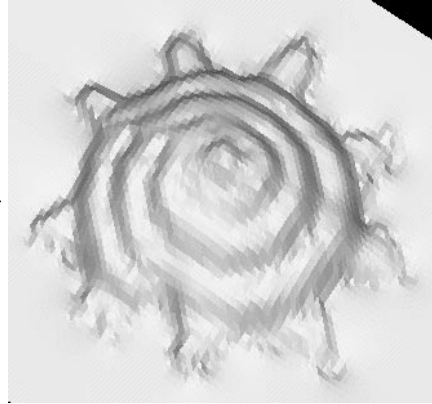
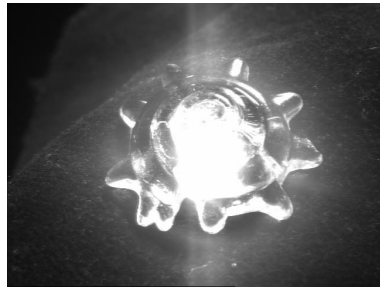


Figure 6.3: Error characteristics of the spherical object.

---



(a) Acrylic shellfish object

(b) Obtained shape

Figure 6.4: The resulting shape of the shellfish-shaped object.

---

### Experiments Using a Shellfish-shaped Object

In order to demonstrate the applicability of the first method to an object of general shape, I determined the shape of the object shown in Figure 6.4(a). The shellfish-shaped object is made of acrylic and its refractive index is 1.5. Figure 6.4(b) shows the obtained shape of the object. Here the system provides the distribution of surface normals. From this obtained distribution, a relaxation algorithm [Ike84] converts the surface normal distribution into a shape corresponding to that of the object.

Figure 6.4(b) recovers the original shape. Notably, the area of steeper angles (that is, those larger than the Brewster angle) provides better recovery results. At the boundary, the shape is a bit noisy. At that region, the degree of polarization is almost zero, and it is difficult to determine this value.

### 6.3.2 Experimental Results of Differential Geometry Method

This section shows the experimental results of the second method, which uses differential geometry. Section 6.3.2 provides computation results of computing the shape of objects generated by simulation. Section 6.3.2 provides the result of measuring a hemispherical object, Section 6.3.2 provides the result of measuring a heart-shaped object, Section 6.3.2 provides the result of measuring a bell-shaped object, and Section 6.3.2 provides the result of measuring a mountain-shaped object.

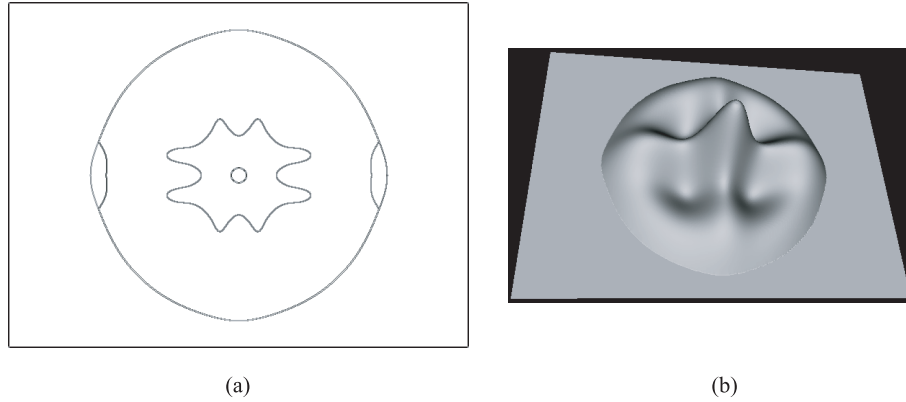


Figure 6.5: Simulation result of the object No.1: (a) Boundaries of each region, (b) the resultant 3D-shape.

---

### Simulational Results of Differential Geometry Method

Before practicing the differential geometry method, I applied the technique to simulated objects to verify the effectiveness of the method. Figure 6.5, 6.6, and 6.7 are the results of the simulation. Figure 6.5(a), 6.6(a), and 6.7(a) depict Brewster curves and occluding boundary of simulated objects. There are 5, 6, and 3 regions depicted in Figure 6.5(a), 6.6(a), and 6.7(a), respectively. Figure 6.5(b), 6.6(b), and 6.7(b) depict the resulting 3D shapes. The simulation software produces the data of degree of polarization, and the disambiguating software computes the surface normal of the object. In this simulation, I inspected the effectiveness of the method, which solves the ambiguity and determines the correct incident angle,  $\theta$ . In this simulation, I assumed that the azimuth angle,  $\phi$ , is given. In addition, I assumed that internal interreflection would not occur.

### Experiments Using a Hemispherical Object

First, I analyzed the precision of the measurement system before applying the proposed method. For this experiment, I used an acrylic transparent hemisphere whose refractive index was 1.5 and diameter was 30mm. The refractive index was obtained from the literature [SAP94].

Figure 6.8 illustrates the resultant shape of the hemisphere. Figure 6.8(a) represents the comparison between the theoretical shape and the obtained shape. The circle represents the theoretical shape, and the plotted dots represent the obtained shape. Figure 6.8(b) represents the result 3D shape.

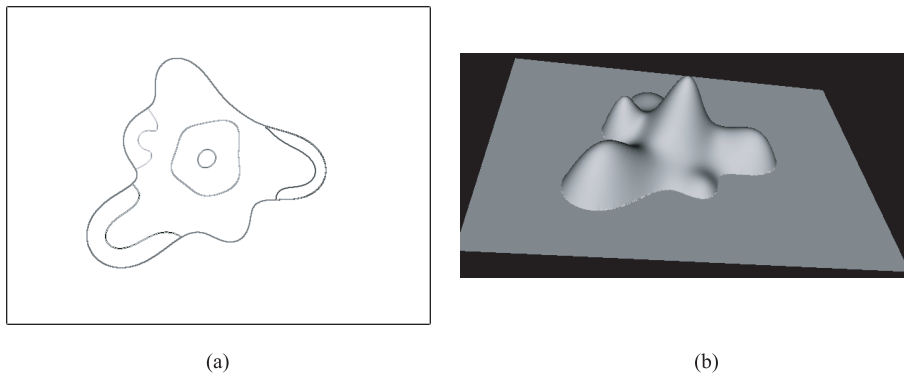


Figure 6.6: Simulation result of the object No.2: (a) Boundaries of each region, (b) the resultant 3D-shape.

---

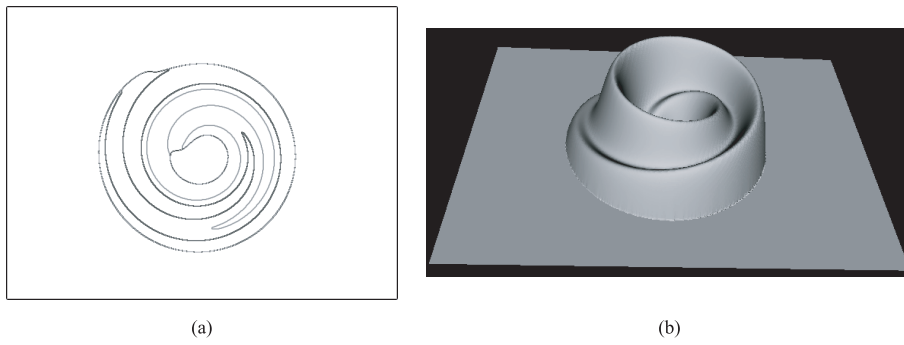


Figure 6.7: Simulation result of object No.3: (a) Boundaries of each region, (b) the result 3D-shape.

---

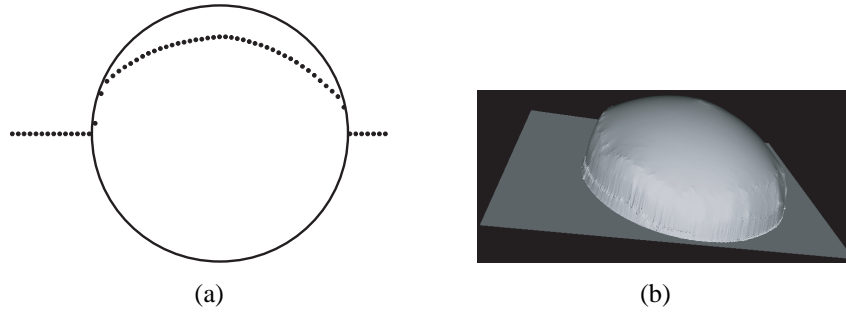


Figure 6.8: The result of the real hemisphere object: (a) Circle for the theoretical shape and plotted dots for the obtained shape, (b) the resultant 3D-shape.

---

The height of the obtained shape seems to be lowered. The reason is that the obtained DOP is attenuated by internal interreflection.

Figure 6.9 illustrates this modification effect described in Section 6.2.1. The theoretical value of the degree of polarization is represented as a solid curve, and the obtained data is plotted as dots. Figure 6.9(a) is produced by using the raw data and Figure 6.9(b) is produced by using modified data. At the range where the angle is bigger than the Brewster angle, the modified data is likely to fit the theoretically estimated value, while at the range where the angle is smaller than the Brewster angle, the modified degree of polarization is still smaller than the theoretically estimated value. This result explains the reason for the height attenuation in Figure 6.8. In Figure 6.8, I can see that the angle larger than the Brewster angle is likely to fit the theoretically estimated height, while the height where the angle is smaller than the Brewster angle is lower than the theoretically estimated height.

Since I knew that the shape was a hemisphere, the computed data became comparable with the true value. Error was calculated as an average value throughout the entire object's surface, that is, it was computed as an absolute difference between the true value and the obtained value. The errors of DOP, incident angle, and height were 0.17, 8.5°, and 1.1mm, respectively. Since the radius of the hemisphere was 15mm, the true average height was 10mm. Therefore, the error rate,

$$\frac{\text{average of } |\text{true height} - \text{calculated height}|}{\text{average of true height}} \quad (6.2)$$

was 11 percent for this measurement.

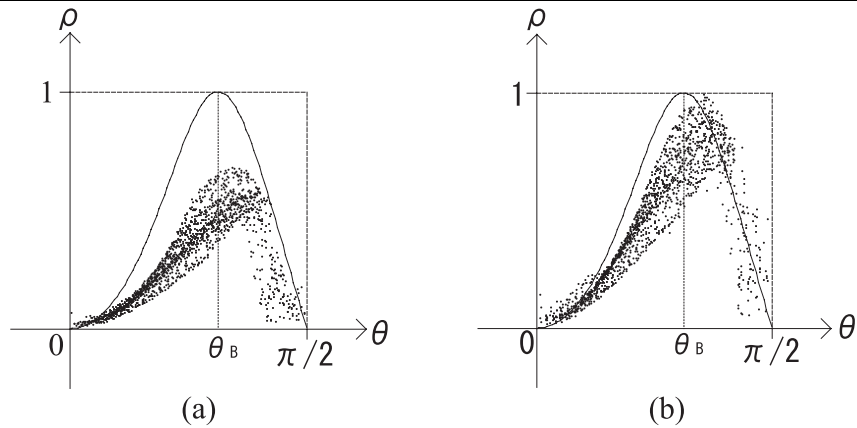


Figure 6.9: The graph of the DOP of the hemisphere object: (a) Raw data plotted, (b) modified data plotted.

### Experiments Using a Heart-shaped Object

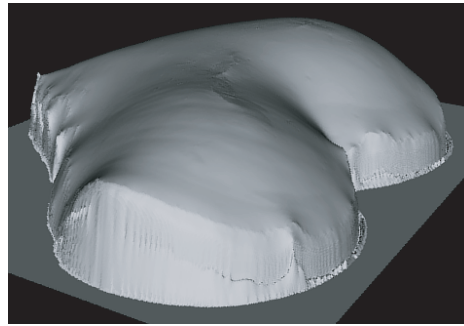
I also measured the heart-shaped piece of glass depicted in Figure 6.10(a). There was no B-B region, making the object rotation unnecessary. The obtained shape is shown in Figure 6.10(b).

### Experiments Using a Bell-shaped Object

In order to demonstrate the applicability of the system to a real object of more general shape than a hemisphere, I determined the shape of the bell-shaped object shown in Figure 6.11. Figure 6.12(b) represents Brewster curves and occluding boundary. There are 3 regions. The object was made of acrylic and its refractive index is 1.5, obtained from the literature [SAP94]. I tilted the object approximately 8 degrees and obtained the data from two views. By applying the method to the data that had been obtained, I calculated the distribution of the surface normal of the object. Then, I used a relaxation algorithm [Hor86, Ike84] to convert the surface normal distribution into a shape corresponding to that of the object. Figure 6.13 shows the rendered image of the estimated shape of the object. Figure 6.14 is a rendered example of the estimated object. Figure 6.15 illustrates how the estimated shape fitted the true shape. Dots represent the obtained height and a solid line represents the true value, which was obtained by hand using the edge from the photo of the object observed from the side. The diameter (width) of the object was 24mm and the height was 8mm. An average error (absolute difference) of the height was 0.4mm.



(a)



(b)

Figure 6.10: (a) Photograph of transparent heart-shaped glass and (b) the obtained shape of this object.

---

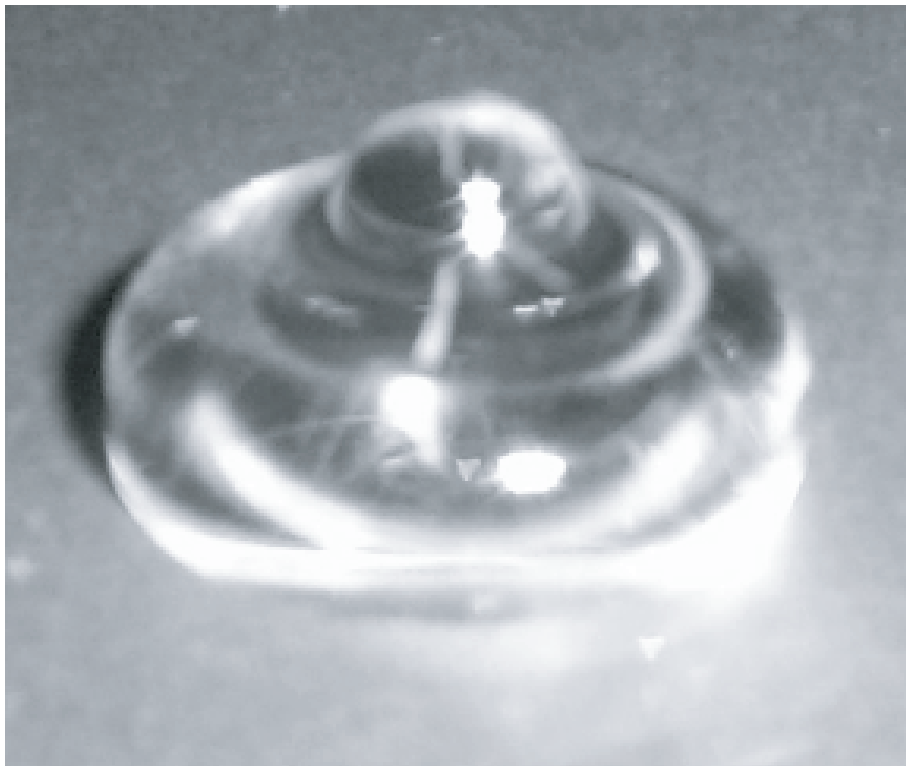


Figure 6.11: A photograph of the bell-shaped object.

---

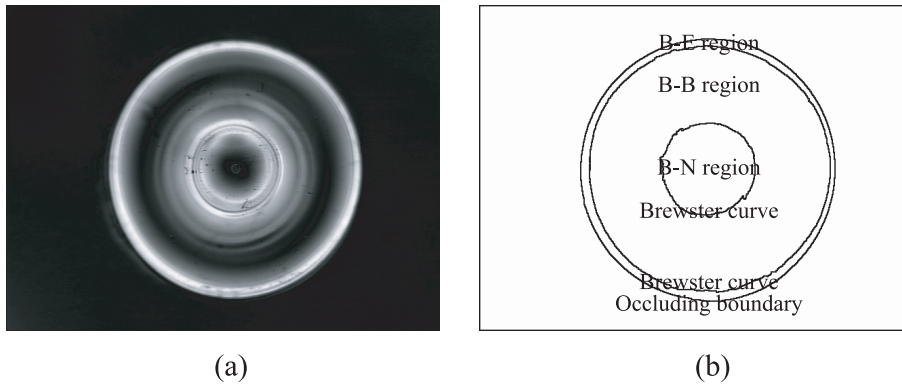


Figure 6.12: (a) A gray image of obtained degree of polarization of the bell-shaped object and (b) the result of Brewster segmentation.

---

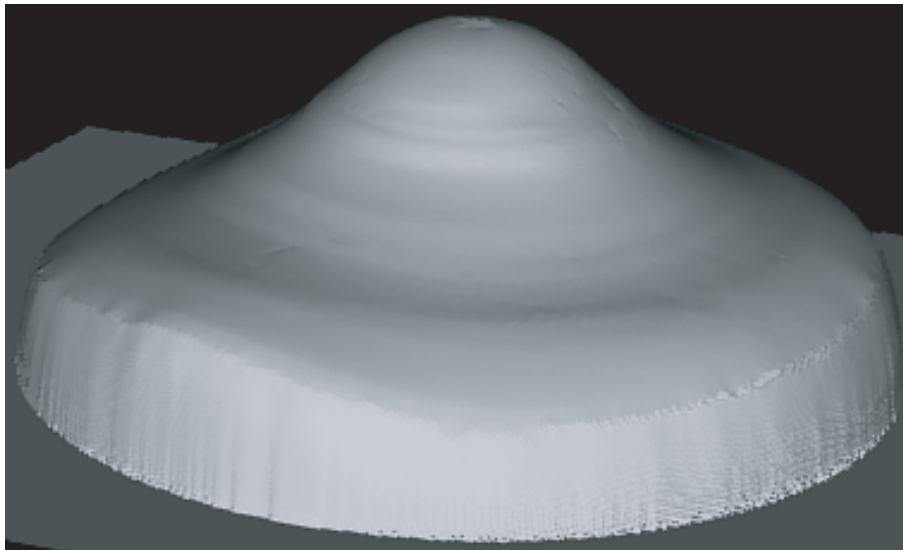


Figure 6.13: A rendered image of the obtained shape of the bell-shaped object.

---

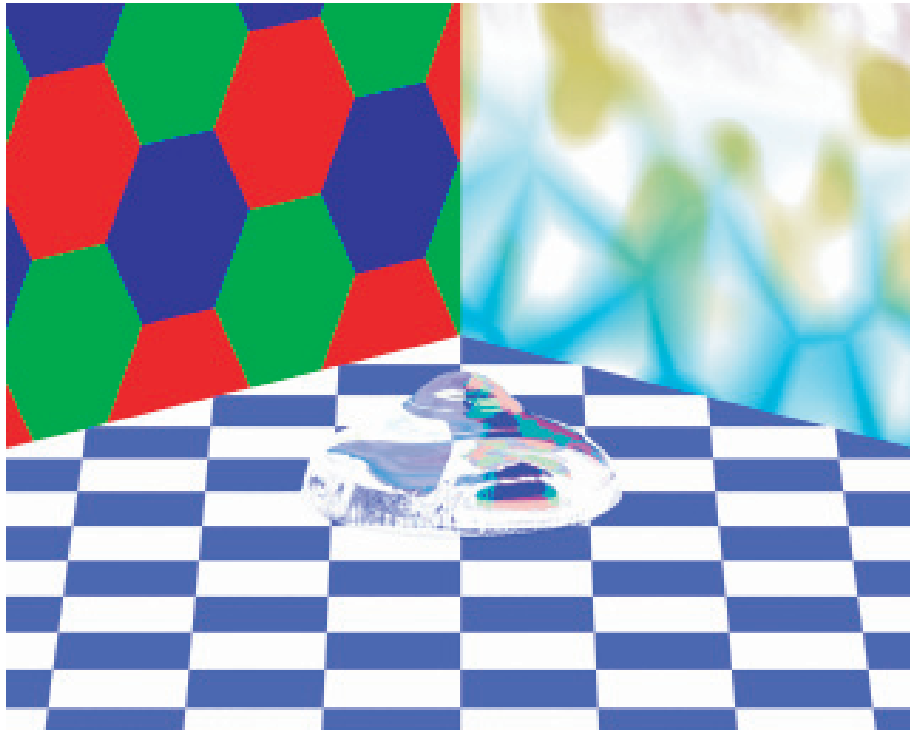


Figure 6.14: Rendering example of the estimated bell-shaped object.

---

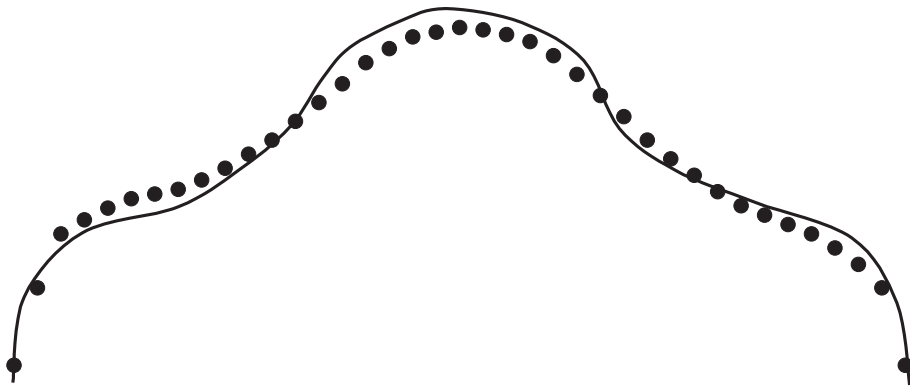


Figure 6.15: The result of the real bell-shaped object.

---

A small error exists in the estimated shape, probably due to the internal interreflection of the object. Internal interreflection lowers the DOP. This means that the zenith angle smaller than Brewster angle becomes smaller and the angle larger than Brewster angle becomes larger. However, the observed area of the smaller zenith angle is larger than that of the larger angle. Therefore, the resulting height will often be lower than the true height; the difference of the height is squeezed. I modified the input data and raised the DOP; however, the modification is not ideal; thus, the resultant height will be different from the true value.

### **Experiments Using a Mountain-shaped Object**

Another transparent object shown in Figure 6.16(a) was measured. This mountain-shaped object was made of epoxy and its refractive index was 1.6 [SAP94]. The diameter (width) of the object was 45mm and the height was 25mm. Figure 6.16(b) shows the result of region segmentation. Here, one B-E region, one B-N region, and four B-B regions are observed. I rotated the object approximately 8 degrees. Figure 6.16(c) and Figure 6.16(d) represent the estimated shape of the object.

### **6.3.3 Experimental Results of the Inverse Polarization Raytracing Method**

This section shows the experimental results of the third method, which uses polarization raytracing. Section 6.3.3 provides calculation results of the polarization raytracing method. Section 6.3.3 provides computation results of computing the shape of objects generated by simulation. Section 6.3.3 provides results of measuring a hemispherical object, Section 6.3.3 provides results of measuring a bell-shaped object, and Section 6.3.3 provides results of measuring jelly.

#### **Rendering Results of Inverse Polarization Raytracing Method**

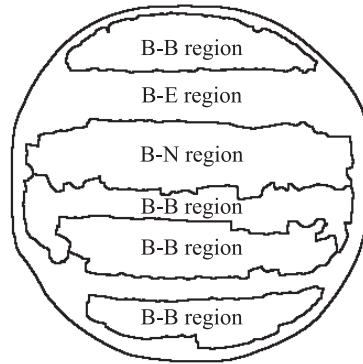
Before estimating the shape of the transparent object, I analyzed the rendered image of forward polarization raytracing (Section 2.2).

From the spherical part, I observed a transparent acrylic hemisphere, whose refractive index was 1.5 and diameter was 30mm. I assumed that the illumination was distributed uniformly from all directions with the same intensity and that the bottom surface of the object, a disk, was not illuminated.

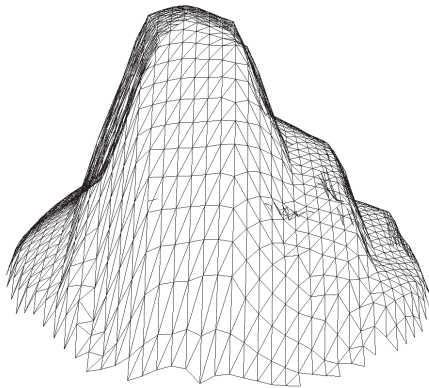
The rendered polarization image of polarization raytracing is shown in Figure 6.17(b), and a real polarization image is shown in Figure 6.17(c). Here, each figure represents the DOP, where DOP 0 and DOP 1 are represented as black and white, respectively.



(a)



(b)



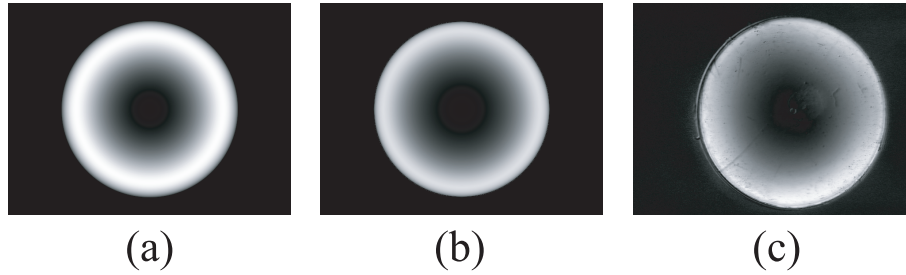
(c)



(d)

Figure 6.16: Result of measuring a transparent mountain-shaped object: (a) Real image, (b) region segmentation result, and (c) and (d) rendered image.

---



---

Figure 6.17: DOP image; (a) rendered by polarization raytracing, (b) obtained from real object, and (c) rendered by assuming that the internal interreflection does not occur.

---

For comparison, a rendered image with no internal interreflection is shown in Figure 6.17(a). This DOP image is rendered by assuming that the light that was reflected at the object's surface once is just observed and that the transmission does not occur. Apparently, Figure 6.17(a) is far from Figure 6.17(b) and Figure 6.17(c). The root mean square (RMS) error between real data (Figure 6.17(c)) and DOP data of no internal interreflection (Figure 6.17(a)) was 0.31, while the RMS error between real data and polarization raytracing data (Figure 6.17(b)) was 0.18.

The computation time was 3.6[sec] with 7,854 pixels by using Pentium4 3.4GHz. Here, the number of light rays traced is 10 reflections or transmissions.

### **Simulated Results of Inverse Polarization Raytracing Method**

In this section, I will show the result of estimating the 2D shape of objects generated by simulation for evaluating the accuracy of the proposed algorithm. The simulation program first generates the true shape of the virtual transparent object, and then computes the polarization data by the polarization raytracing method. The frontal surface of all virtual transparent objects is illuminated uniformly from any direction with the same intensity; however, the light was not set to illuminate the bottom of the object. Finally, I evaluate the proposed algorithm by applying the method to the input data, which is the polarization data computed by the simulation program, assuming the rear surface shape and the refractive index is known.

The first result is that of a 2D virtual transparent object, which is an isosceles triangle shape whose refractive index is 1.5 and whose two base angles are  $76.6^\circ$ . The object is observed from an apical angle. The computation time was 8.1[sec] for 1 loop with 320 pixels by using Pentium4 3.4GHz. Here, the maximum number of the light ray traced is 100 reflections or transmissions; however, if the energy of the light ray becomes less than a certain threshold,

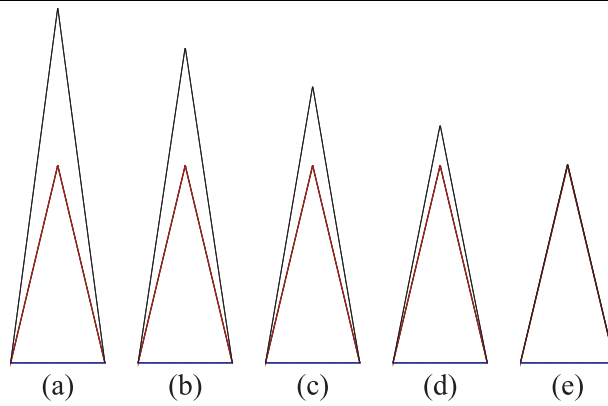


Figure 6.18: Simulation result of a triangle: (a)Initial state (true height times 1.8), (b)–(e)result after 10, 20, 30, 40 loops, respectively.

---

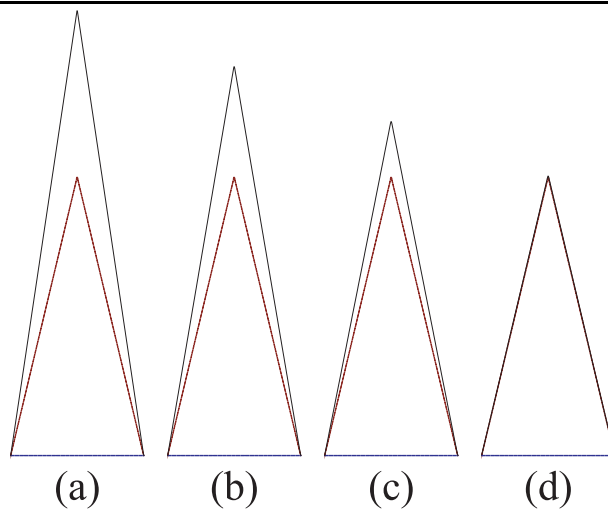


Figure 6.19: Simulation result of a triangle: (a)Initial state (true height times 1.6), (b)–(d)result after 10, 20, 30 loops, respectively.

---

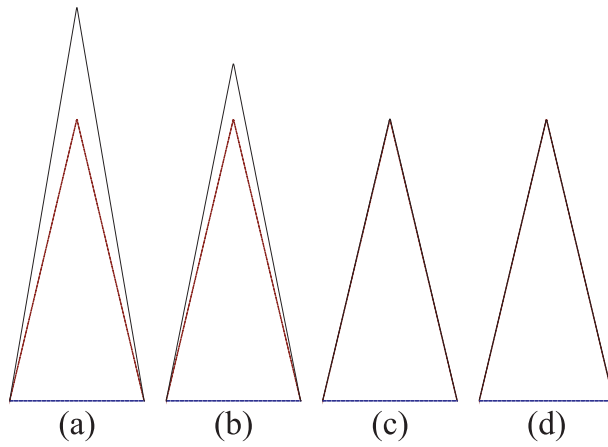


Figure 6.20: Simulation result of a triangle: (a)Initial state (true height times 1.4), (b)–(d)result after 10, 20, 30 loops, respectively.

---

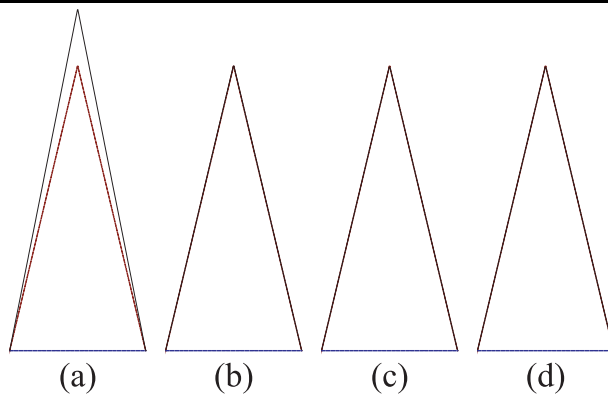


Figure 6.21: Simulation result of a triangle: (a)Initial state (true height times 1.2), (b)–(d)result after 10, 20, 30 loops, respectively.

---

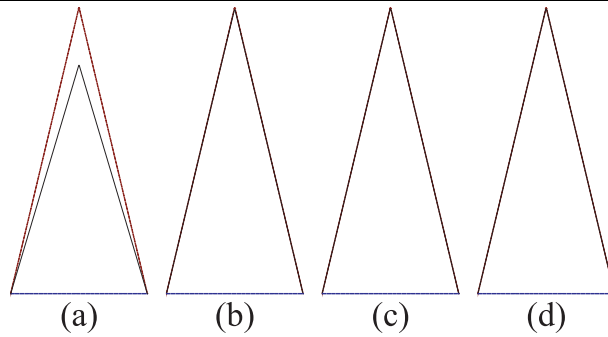


Figure 6.22: Simulation result of a triangle: (a)Initial state (true height times 0.8), (b)–(d)result after 10, 20, 30 loops, respectively.

the tracing of the light ray is stopped. The loop number of Brent's method is set to 8, and that of alternation-direction implicit method is set to 24 (Section 5.3).

The estimated result is illustrated in Figure 6.18, 6.19, 6.20, 6.21, 6.22, 6.23, 6.24, 6.25, 6.26, and 6.27. The dotted red line is the true shape, and the solid black line is the estimated shape. The dotted blue line is the rear surface which is given. For each figure, Figure (a) represents the initial state of the shape, and (b)(c)(d) are the resultant shapes after 10, 20, 30 loops, respectively. Figure 6.18(e) is the resultant shape after 40 loops. I used different initial shape for each figure: Initial shapes of Figure 6.18, 6.19, 6.20, 6.21, 6.22, 6.23, 6.24, and 6.25 are the true height which is scaled by 1.8, 1.6, 1.4, 1.2, 0.8, 0.6, 0.4, and 0.2, respectively. Saito's method produces two kinds of shapes due to its ambiguity; Initial shapes of Figure 6.26 and 6.27 are the two shapes calculated by Saito's method.

The estimated shapes in Figure 6.18, 6.19, 6.20, 6.21, 6.22, 6.23, and 6.26 successfully converge to the true shape; thus, I can state that the proposed method is sufficiently robust in convergence. However, the estimated shapes in Figure 6.24, 6.25, and 6.27 converge to a different shape from the true shape. This fact is caused by the ambiguity of surface normal; thus, the research explained in Section 3 and Section 4 were meaningful and important. This experiment tells that the third method (Section 5) needs an appropriate initial value to avoid the local minimum made by the ambiguity, but fortunately, the error calculated by Equation (5.4) was 0.00656 and 1.39 for Figure 6.26 and 6.27, respectively, thus, the two shapes are distinguishable and the correct shape can be chosen.

The next virtual transparent object is a hexagonal shape whose refractive index is 1.5. The object is represented as a dotted line in Figure 6.28. The polarization data is rendered by observing the object from the upper position to the lower direction. The estimation result

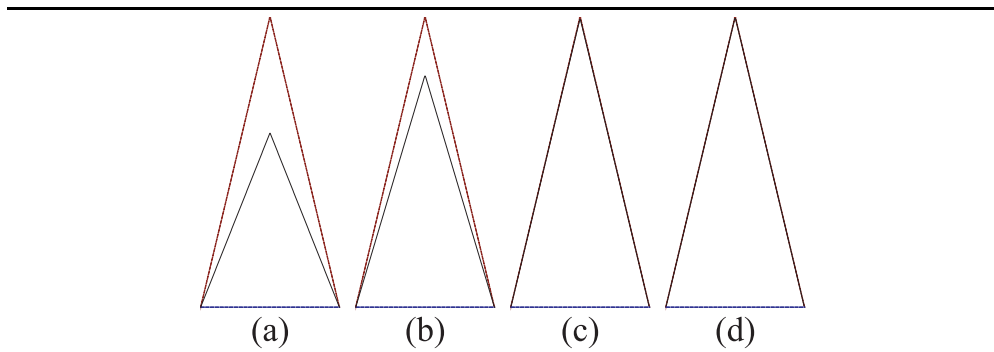


Figure 6.23: Simulation result of a triangle: (a)Initial state (true height times 0.6), (b)–(d)result after 10, 20, 30 loops, respectively.

---

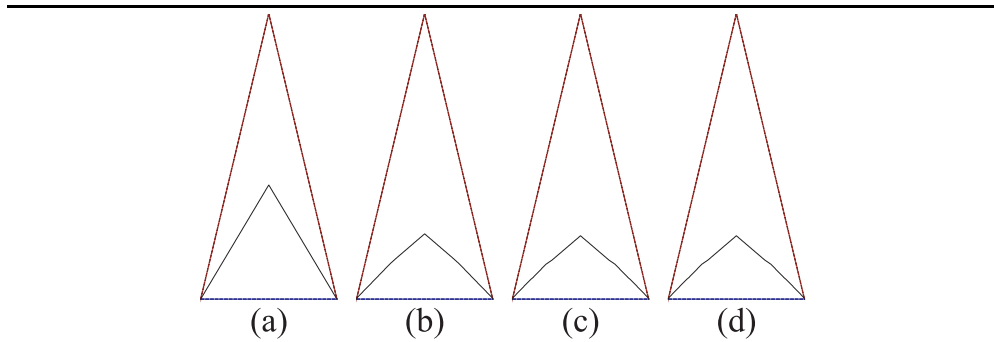


Figure 6.24: Simulation result of a triangle: (a)Initial state (true height times 0.4), (b)–(d)result after 10, 20, 30 loops, respectively.

---

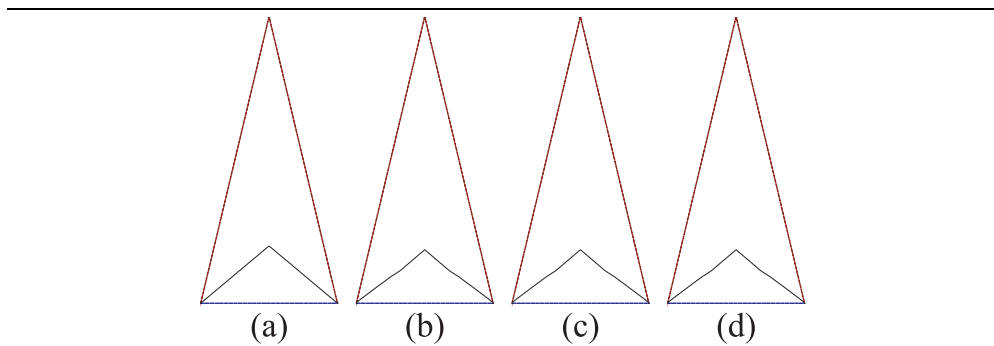


Figure 6.25: Simulation result of a triangle: (a)Initial state (true height times 0.2), (b)–(d)result after 10, 20, 30 loops, respectively.

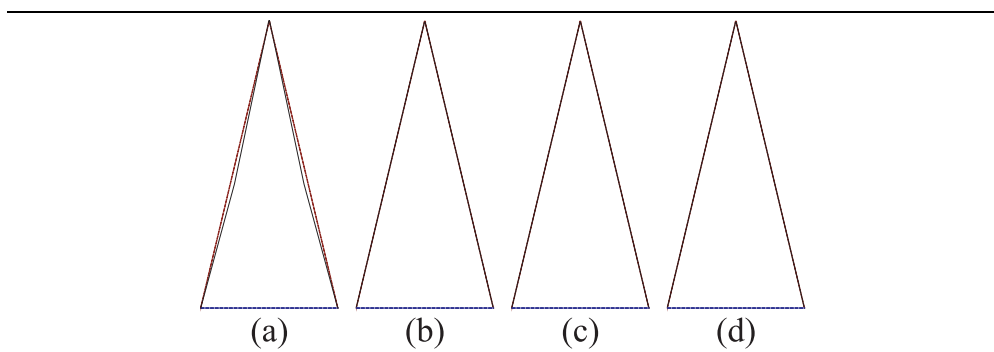


Figure 6.26: Simulation result of a triangle: (a) Initial state (one of the solutions calculated by Saito's method), (b)–(d) result after 10, 20, 30 loops, respectively.

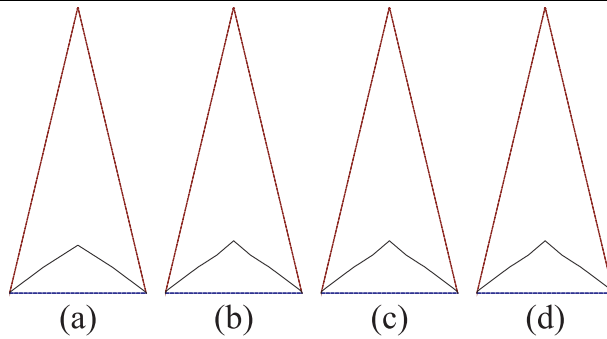


Figure 6.27: Simulation result of triangle: (a) Initial state (one of the solution calculated by Saito's method), (b)–(d) result after 10, 20, 30 loops, respectively.

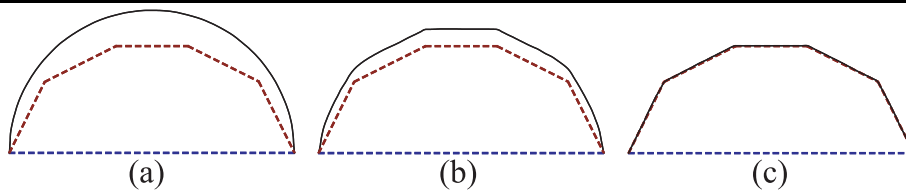


Figure 6.28: Simulation result of a hexagon: (a) Initial state, (b)(c) result after 3, 30 loops, respectively.

is illustrated in Figure 6.28 as a solid line. Figure 6.28(a) indicates the initial value, and (b) and (c) indicate the results after 3 and 30 loops of the proposed method. A hemisphere is used as the initial state of the shape. The shape converged to the true shape at 30 loops. The computation time was 6.4[sec] for 1 loop.

Another virtual transparent object is a bell shape whose refractive index is 1.5. The object is represented as a dotted line in Figure 6.29. The polarization data is rendered by observing the object from the upper position to the lower direction. The estimation result is illustrated in Figure 6.29 as a solid line. Figure 6.29(a) indicates the initial value, and (b)–(l) indicate the results after 2, 4, ..., 22 loops of the proposed method. The shape, which is generated by scaling the true height by 0.01, is used as the initial state of the shape. The shape converged to the true shape at 22 loops. The computation time was 7.8[sec] for 1 loop.

The last virtual transparent object is a concave shape whose refractive index is 1.5. The object is represented as a dotted line in Figure 6.30 and Figure 6.31. An example of the trajectory of the light ray is represented as a black solid line in Figure 6.30. The polarization

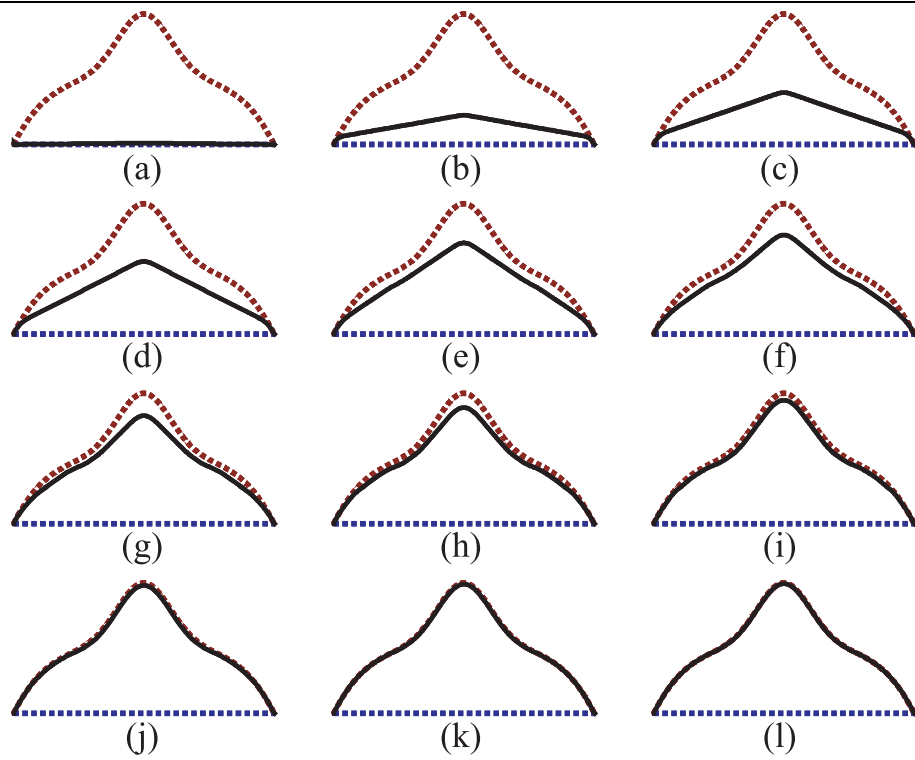


Figure 6.29: Simulation result of bell shape: (a)Initial state, (b)–(l)result after 2, 4, ..., 22 loops, respectively.

---

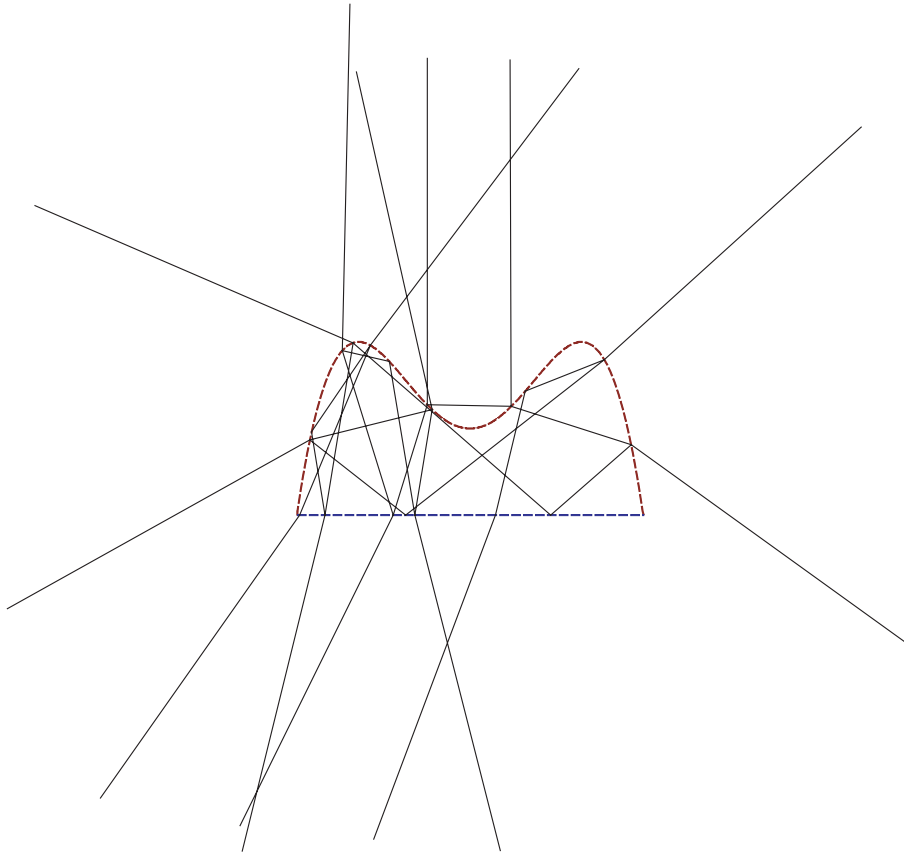


Figure 6.30: Trajectory of the light ray of concave object.

---

data is rendered by observing the object from the upper position to the lower direction. The estimation result is illustrated in Figure 6.31 as a solid line. Figure 6.31(a) indicates the initial value, and (b) and (c) indicate the results after 5 and 20 loops of the proposed method. The shape, which is generated by scaling the true height by 1.2, is used as the initial state of the shape. The shape converged to the true shape at 20 loops. The computation time was 14.8[sec] for 1 loop.

### Experiments Using a Hemispherical Object

I observed an acrylic transparent hemisphere from the spherical part, whose refractive index was 1.5 and diameter was 30mm. The frontal surface was a hemisphere and rear surface was a disk. The camera was set orthogonally to the disk. I assumed that the object was illuminated

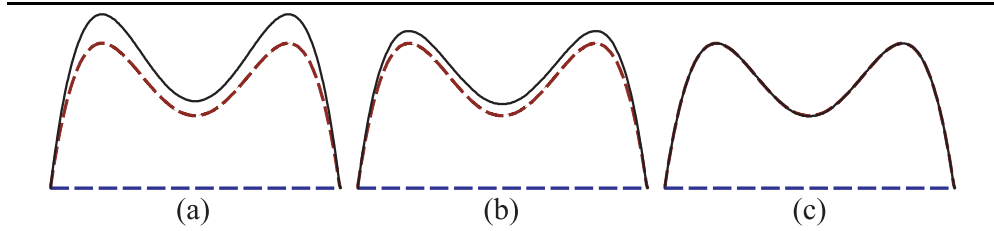


Figure 6.31: Simulation result of concave shape: (a) Initial state, (b)(c) result after 5, 20 loops, respectively.

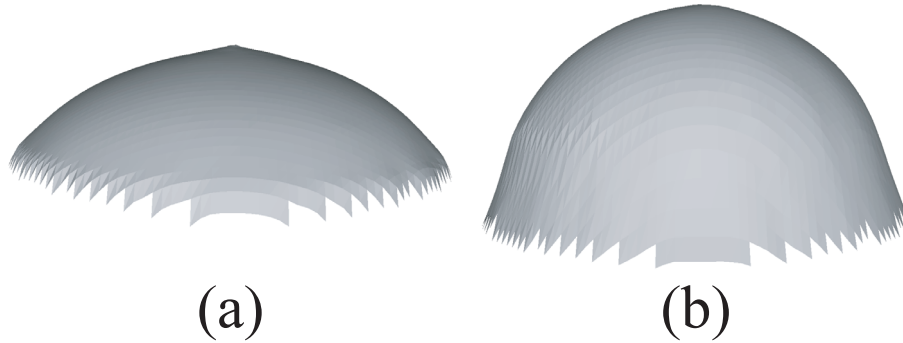


Figure 6.32: 3D hemispherical object result: (a) Initial state, (b) result after 10 loops.

by unpolarized light with uniform intensity from any direction. The disk, the rear surface, was illuminated by background radiation calculated by the method described in Section 6.2.4. Note that the intensity of background radiation is calculated from the same hemisphere; hence, the result in this section is provided only as a suggestion. More objective results are provided in the subsequent sections.

The estimation result is shown in Figure 6.32. Figure 6.32(a) represents the result of Saito's method [SSIK99] and, at the same time, it represents the initial value. Figure 6.32(b) is the result after 10 loops of the method. The computation time was 36[sec] for 1 loop with 7,854 pixels by using Pentium4 3.4GHz. Here, the maximum number of the light rays traced is 10 reflections or transmissions; however, if the energy of the light ray becomes less than a certain threshold, the tracing of the light ray is stopped. The loop number of Brent's method is set to be 8, and that of the alternation-direction implicit method is set to be 24 (Section 5.3). Figure 6.32(b) resembles the hemisphere more accurately than Figure 6.32(a) does.

In order to evaluate the estimation result in more detail, another evaluation was done in the

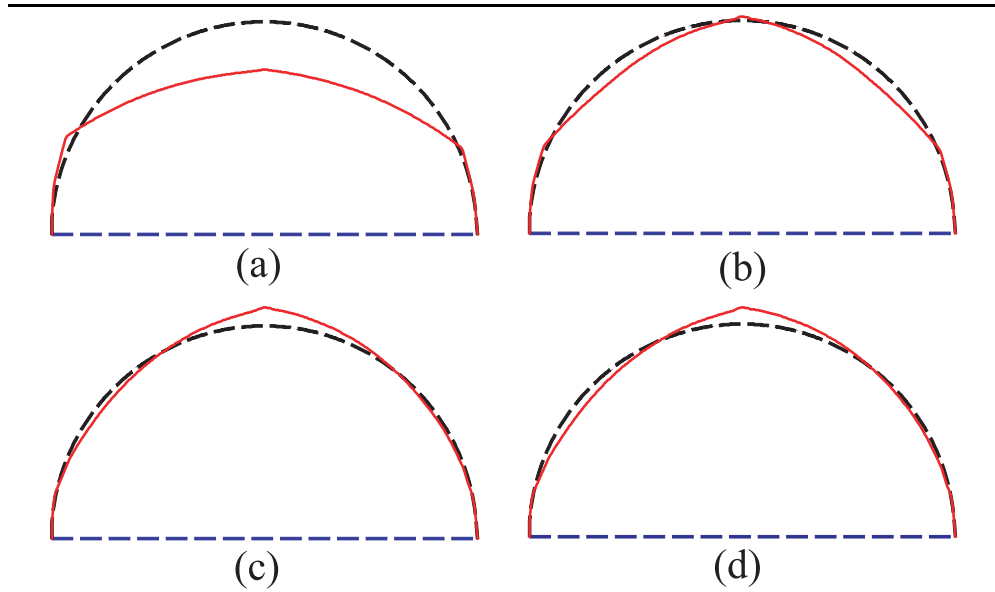


Figure 6.33: Estimation result: (a) Result of Saito's method, (b)(c)(d) result after 5, 25, and 50 loops with proposed method, respectively.

2D plane, which was a cross section of the 3D object, which included the center of the base circle and the line perpendicular to that circle. A light ray that was inside this plane did not go out, and a light ray that was outside this plane did not come in. The proposed algorithm estimated the frontal surface shape, a semicircle, by using the polarization data of the 2D plane as input data.

The result of applying the proposed method is given in Figure 6.33(d). For comparison, the result of Saito's method [SSIK99] is shown in Figure 6.33(a). In Figure 6.33, the solid line represents the estimated shape, and the dotted line represents the true value. The shape computed by Saito's method (Figure 6.33(a)) is used as an initial value for Figure 6.33(d). Figure 6.33(b)(c)(d) is the result after 5, 25, and 50 loops, respectively. The shape did not deform any further even if I computed for more iterations. To ensure this fact, the error value, Equation (5.4), is plotted in Figure 6.34. In Figure 6.34, the vertical axis represents the value of Equation (5.4), and the horizontal axis represents the number of iterations. The leftmost value is the error of Saito's method [SSIK99]. The error did not change after 25 loops. The computation time was 5.9[sec] for 1 loop.

The RMS error between the estimated value and the true value was used to compare the accuracy between the proposed method and Saito's method. The RMS error of the surface

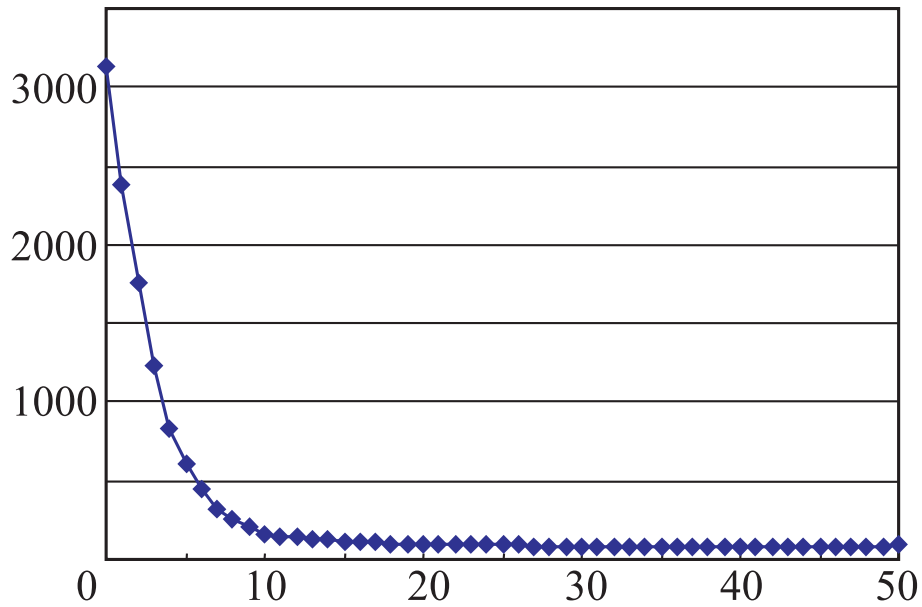


Figure 6.34: Error for each loop.

normal was  $13.5^\circ$  for Saito's method and  $7.02^\circ$  for the proposed method. The RMS error of the height was 2.77mm for Saito's method and 0.607mm for the proposed method. Therefore, I can conclude that the proposed method estimates the surface shape of a transparent object more precisely than Saito's method does.

The reason why the estimated result did not converge to the semicircle, which was the theoretical value, might be the failure to consider the hole on top of the spherical diffuser. Although I had assumed that the object was illuminated uniformly with the same intensity from all directions, the hole on top of the diffuser violates that assumption. Therefore, a reconsideration of the illumination distribution will be future work.

Figure 6.35(a) is the graph of the degree of polarization obtained by observing the real transparent hemisphere. Figure 6.35(b) is the graph of the degree of polarization calculated by using the polarization raytracing method with the true hemispherical shape. Figure 6.35(c) is the graph of the degree of polarization calculated by assuming that the light that reflected at the object surface only once is observed by the camera with the true hemispherical shape. Figure 6.35(d) is the graph of the squared difference between the values in Figure 6.35(a) and the values in Figure 6.35. The horizontal axis in Figures 6.35(a)–(d) represents the pixel position. The vertical axis in Figures 6.35(a)–(c) represents the degree of polarization, and

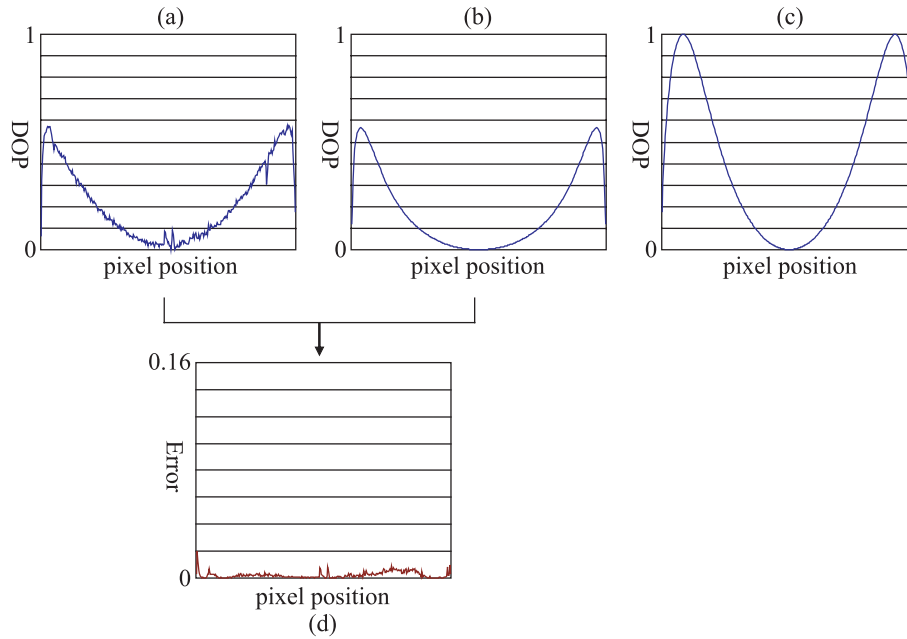


Figure 6.35: DOP: (a) Real data, (b) computed data by polarization raytracing, (c) computed data by assuming only one reflection, (d) error between (a) and (b).

the vertical axis in Figure 6.35(d) represents the error. Two peaks are found in the middle of Figure 6.35(a), while there are no peaks in the middle of Figure 6.35(b). This fact causes the error at the middle of the object as shown in Figure 6.35(d). The proposed method did not consider the hole on top of the spherical diffuser; thus, the rendered data couldn't reproduce these two peaks as shown in Figure 6.35(b). This means that even if the iterative computation tries hard to minimize the error, the estimated shape can never attain the true shape due to this error in the input data.

Figures 6.36(a) represent the graph of the degree of polarization calculated by using the polarization raytracing method with the estimated shape. Figures 6.36(1)–(5) represent the degree of polarization for 0, 2, 5, 10, and 50 loops, respectively. Figures 6.36(b) represent the graph of the squared difference between the obtained DOP and the calculated DOP, which is denoted as  $(I_E - I_R)^2$ . The more the iteration process progresses, the closer the calculated DOP (Figures 6.36(a)) will be to the obtained DOP (Figure 6.35(a)). The more the iteration process progresses, the less the error becomes (Figures 6.36(b)). There are no peaks in the middle of Figure 6.36(5b) as is shown in Figure 6.35(d). The iteration process strives to make

the calculated DOP resemble the obtained DOP without knowing that the obtained DOP is polluted by noise.

### **Experiments Using a Bell-shaped Object**

I applied the method using polarization raytracing to the bell-shaped transparent object shown in Figure 6.11 in Section 6.3.2. The object was made of acrylic and its refractive index was 1.5, obtained from the literature [SAP94]. The diameter (width) of the object was 24mm and the height was 8mm. The object was observed from the projected area of the object. The frontal surface was the curved surface and the rear surface was a disk. The camera was set orthogonally to the disk. I assumed that the object was illuminated by unpolarized light with uniform intensity from any direction. The disk, the rear surface, was illuminated by background radiation calculated by the method described in Section 6.2.4.

I estimated the shape of the cross-section of the object to analyze the precision of the proposed method. Figure 6.37(d) illustrates the estimated shape of the object. The red solid curve represents the obtained frontal height, and the blue dotted line represents the given rear height. The initial value was set to be a semicircle shown in Figure 6.37(a). The estimated shape after 1, 5, and 20 loops is illustrated in Figure 6.37(b), (c), and (d), respectively. The true shape is represented as a solid curve in Figure 6.15. An error (mean deviation) of the height was 0.24mm. Compared to the result shown in Section 6.3.2, 40 percent of the error is reduced. The computation time was 7.0[sec] for 1 loop.

### **Experiments Using Jelly**

Figure 6.38(a) is a photograph of a transparent jelly. Haptic devices cannot measure such soft objects. For example, suppose a red stick in Figure 6.38(b)(c) is a touch sensor trying to measure the jelly. In most cases, the sensor cannot stop at the surface of the jelly and destroys the jelly as illustrated in Figure 6.38(d). Jelly does not have much repulsive force thanks to its softness; thus, even if the haptic device has a force-feedback system, the system cannot detect the repulsive force at the surface of the jelly. However, if humans operate the touch sensor, they can stop the sensor at the surface of the jelly, because humans can see the position of the sensor and the shape of the jelly (visual feedback). Therefore, I state that recognizing the shape of the object by visual technique is very important.

My methods can measure such soft transparent objects, and I will show the measurement result by using the inverse polarization raytracing method. The refractive index of the jelly is 1.4, obtained from the literature [Sch79] and the sugar content [Exa]. The object is observed from the thinner part of the object. The camera was set orthogonally to the base of the jelly. I assumed that the object was illuminated by unpolarized light with uniform intensity from any

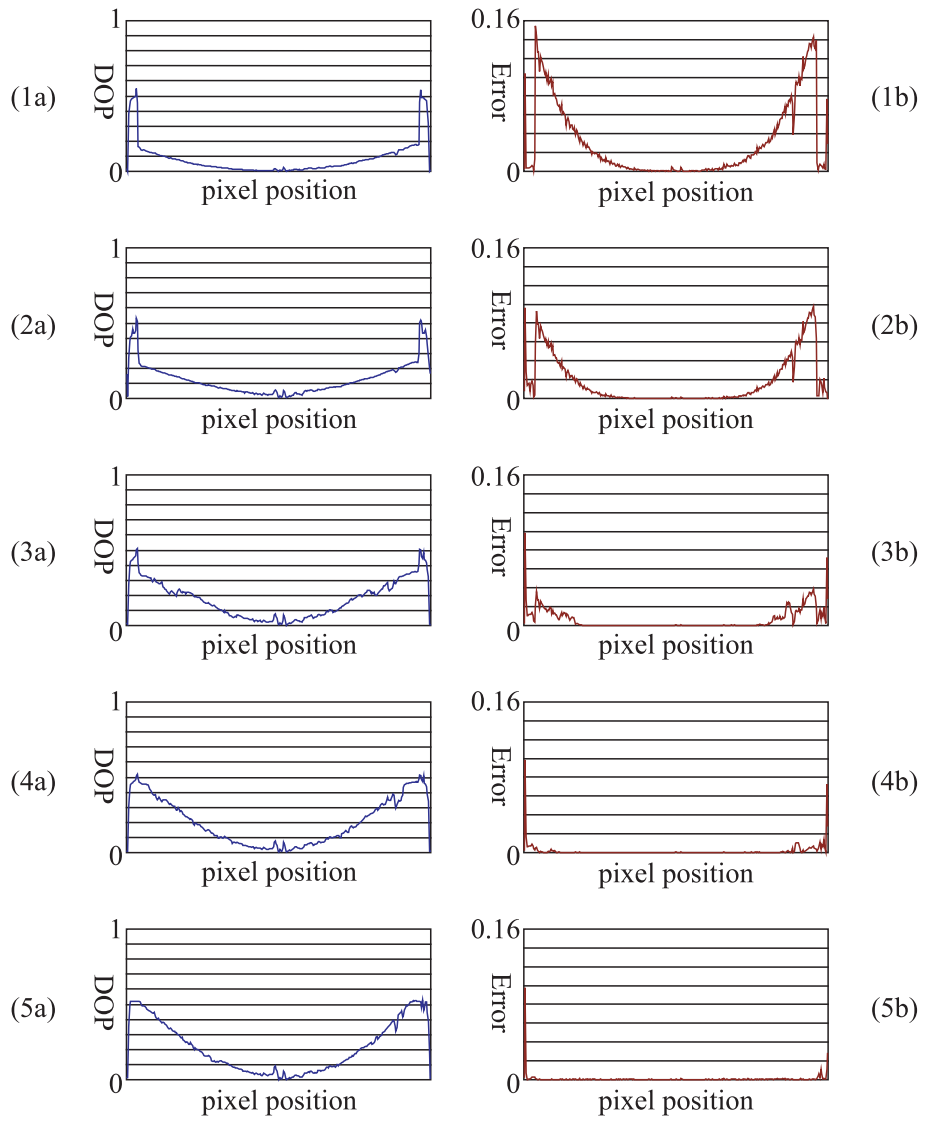


Figure 6.36: DOP and error: (a) DOP, (b) error; (1)–(5) result after 0, 2, 5, 10, 50 loops, respectively.

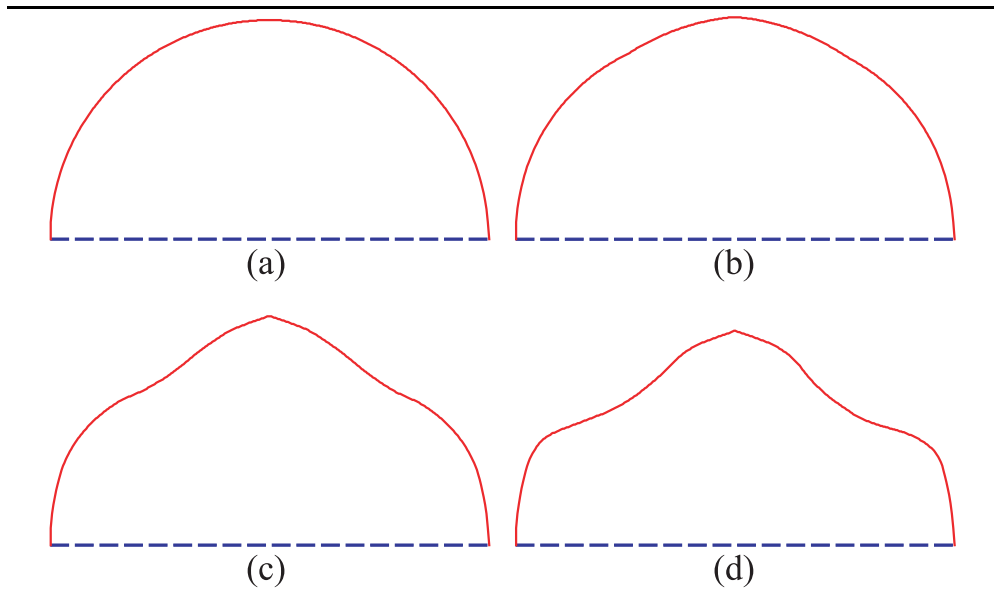


Figure 6.37: Estimated shape of bell-shaped acrylic object by using the inverse polarization raytracing method: (a) initial value, (b)(c)(d) estimated after 1, 5, and 20 loops, respectively.

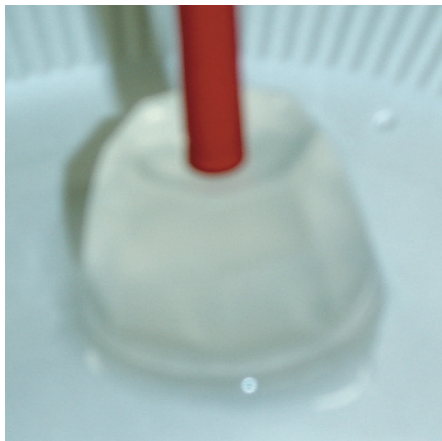
---



(a)



(b)



(c)



(d)

Figure 6.38: Photograph of transparent jelly: (a) photograph of transparent jelly, (b)(c)(d) showing the situation where the touch sensor destroys the jelly and cannot measure the shape of the jelly.

---

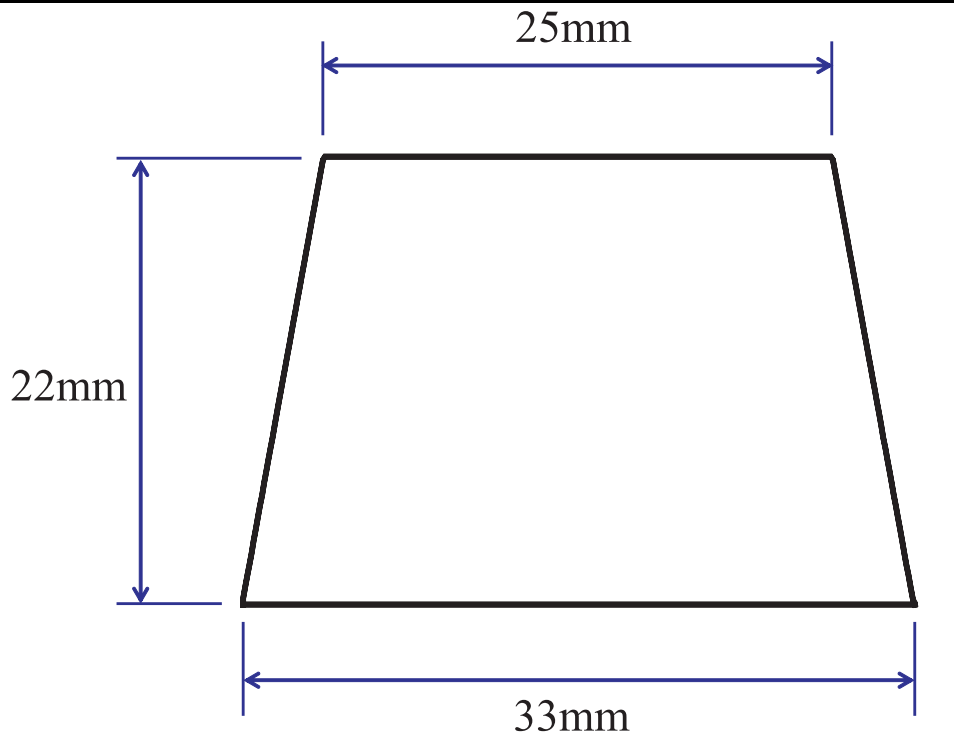


Figure 6.39: True shape of jelly.

direction. The rear surface was illuminated by background radiation calculated by the method described in Section 6.2.4.

Shape estimation is done at the cross-section of the object to analyze the jelly in detail. Figure 6.39 expresses the true shape of the object, which is obtained by measuring the mold by a ruler. The object is a trapezoid whose length of the upper base is 25mm, length of the lower base is 33mm, and height is 22mm. The estimated shape is shown in Figure 6.40. The red solid line represents the obtained frontal shape, the blue dotted line represents the given rear shape, and the black dotted line represents the true shape. Figure 6.40 is the result of the 50th iteration, and the initial value is set to be the true shape. The RMS error of the surface normal was  $12^\circ$  and that of the height was 0.84mm. The computation time was 6.8[sec] for 1 loop.

The reason why the result is not very close the theoretical value is due to the noise that appeared in the input data. I think the noise in the input data is caused by the anisotropy and the translucency of the jelly. Due to the ingredients or other effects during the coagulation,

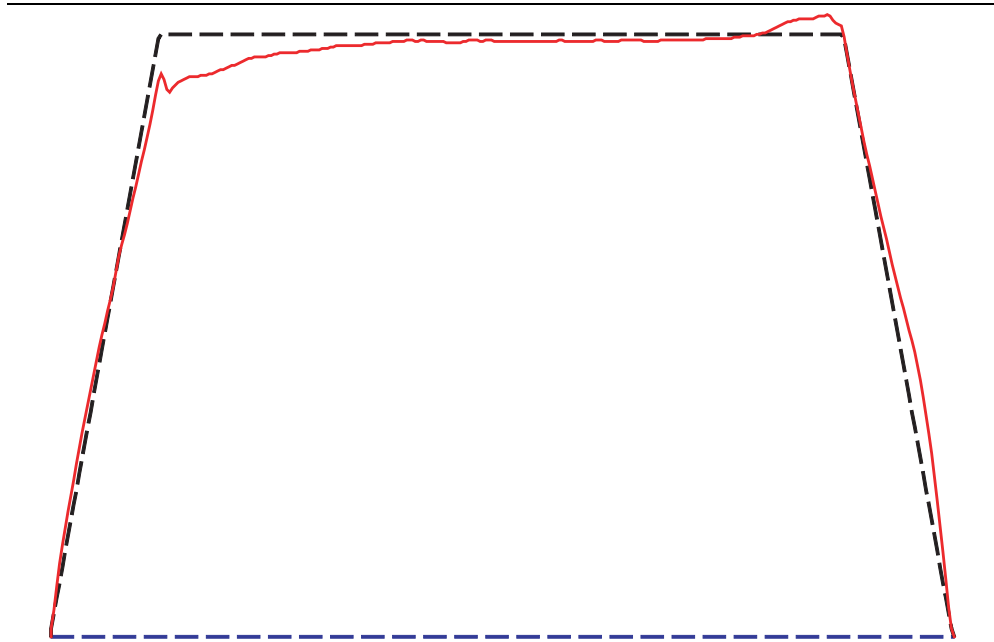


Figure 6.40: Estimated shape of jelly.

jelly becomes slightly anisotropic and translucent, and the refractive index and the opacity will slightly differ from each part inside the jelly. This effect invalidates the assumption that the object must be isotropic and transparent. Therefore, my methods recognize the anisotropy and the translucency as noise. A noise reduction process is needed for estimating the shape of an object that has such characteristics, but fortunately, many noise reduction techniques are proposed in the field of image processing such as smoothing, median filtering, fitting polynomials or B-spline curves, or frequency-based methods such as Chebyshev approximation, Fourier analysis, and wavelet transformation. Shape estimation by analyzing the nonuniformity of refractive index and opacity is an ideal; however, I am convinced that it will be a very difficult work. Therefore, I am planning to develop a method that uses more input data obtained from different views or under different illuminations because, by increasing the amount of input data, the shape can be estimated in a way that is more resistant to noise.

### **Experiments Using a Heart-shaped Object**

I applied the method using polarization raytracing to the bell-shaped transparent object shown in Figure 6.10(a) in Section 6.3.2. The object was made of glass and its refractive index was 1.5, obtained from the literature [SAP94]. The object was observed from the curved surface of the object. The frontal surface was the curved surface, and the rear surface was a planar surface. The camera was set orthogonally to the rear surface. I assumed that the object was illuminated by unpolarized light with uniform intensity from any direction. The rear surface was illuminated by background radiation calculated by the method described in Section 6.2.4.

The estimation result is shown in Figure 6.41. Figure 6.41(a) represents the result of Saito's method [SSIK99] and, at the same time, it represents the initial value. Figure 6.41(b) is the result after 10 loops of the method. The computation time was 36[sec] for 1 loop with 7,854 pixels by using Pentium4 3.4GHz. Figure 6.41(c) is a rendered example of the raytracing method by using the estimated shape.

### **6.3.4 Comparison to Other Research**

In the above sections, I have compared my result to Saito's method. In this section, I will compare the proposed method to other researchers' methods.

Other researchers have also proposed methods to estimate the shape of transparent objects. Murase's method [Mur92] can only measure the shape of water surface. Ohara's method [OMOT03] can only measure the depth of the edge of the object. Ben-Ezra's method [BN03] can only measure a parametrized surface such as a sphere or rounded cube. Hata's method [HSKK96] estimated the surface shape of transparent paste. Hata's method is suitable for

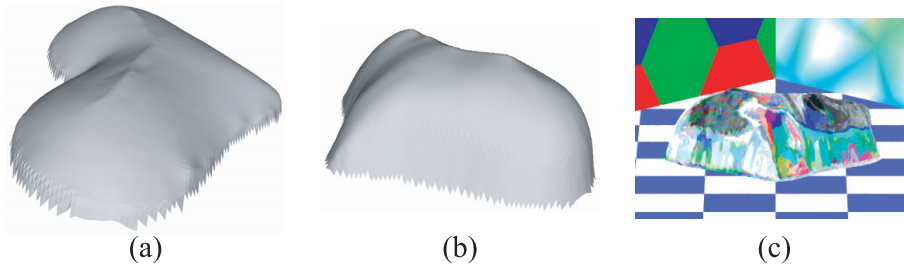


Figure 6.41: 3D heart object result: (a) Initial state, (b) result after 10 loops, (c) raytracing image.

---

measuring paste-like shapes; however, the method can possibly be used to estimate an arbitrary shape. Therefore, I compare the proposed method with Hata's method in this thesis.

### **Hata's Algorithm**

First, I will briefly explain Hata's algorithm.

The target object is set on a desk, and the camera observes the transparent object from above. A slit ray beam is shot from the projector, which is set obliquely to the object and set above the desk. Object, camera, and projector are fixed; however, the direction of the slit ray beam is changed. Images are taken for each shot of the slit ray beam.

Computation of the shape is done by using a genetic algorithm. If the estimated shape coincides with the true shape, then the position of the slit ray beam on the surface of the desk will coincide. Therefore, the error function can be determined as the difference of the position of the slit ray beam on the desk. True ray position is obtained from the camera, while the estimated ray position is calculated by tracing the ray direction for one transmission.

There are three operations in a genetic algorithm; "mutation," "cross-over," and "natural-selection." The "mutation" procedure is to generate a shape model randomly. The "cross-over" procedure is to merge the models of the two shapes. The "Natural-selection" procedure is to select models that have less error than other models.

First, 20 initial models are created by mutation. Next, 40 models are created by cross-over, and another 40 models are created by mutation. Then, natural-selection is done, and 20 superior models will survive out of the 100 models generated. This cycle is repeated for 50 generations.

### Comparison to the Proposed Method

The evaluation is done in computer simulation for two reasons: (1) To set up the measurement apparatus of Hata's method is indeed a hard task, and (2) the two methods must be compared with the estimation algorithm itself since a fair comparison cannot be done if the accuracy depends on how I set up the measurement apparatus of Hata's method. I compare Hata's method with the method described in Chapter 5, the method that uses polarization raytracing. Evaluation is done in a 2D plane. The number of pixels I used for both Hata's method and my method was 320 points. The number of slit ray beams I used for Hata's method was 320 lights. The projector was set  $30^\circ$  right to the camera.

The estimation results for the virtual transparent hexagon shape, the concave shape, the bell shape, and the triangle shape are presented in Figures 6.42(1a)(1b), 6.42(2a)(2b), 6.42(3a)(3b), and 6.42(4a)(4b), respectively. Figures 6.42(1a)(2a)(3a)(4a) are the most superior models of the initial 20 shapes in Hata's method. Figures 6.42(1b)(2b)(3b)(4b) are the estimation results of Hata's method after 50 loops. Black solid line represents the estimated shape, red dotted line represents the true frontal shape, and blue dotted line represents the rear surface shape, which is known a priori. Hata's method cannot estimate these shapes, while the proposed method successfully estimates them as is shown in Section 6.3.3.

All of the results of Hata's method shown in Figure 6.42 are similar to a hemisphere. I regarded Hata's method as failing to estimate undulating shapes but as somewhat good at estimating hemispherical shapes. Therefore, I applied Hata's method to the virtual transparent hemisphere (semicircle) presented in Figure 6.43, and compared the result of Hata's method to that of my proposed method. The computation time of Hata's method was 3.1[sec] for each loop, while that of the proposed method was 7.0[sec]. Figure 6.43(1a) is the most superior model of the initial 20 shapes in Hata's method. I used the same shape also for the proposed method (Figure 6.43(2a)). Figures 6.43(1b)(1c)(1d) are the estimation result of Hata's method after 1, 2, and 50 loops. Figures 6.43(2b)(2c)(2d) are the estimation result of the proposed method after 1, 2, and 50 loops. The black solid line represents the estimated shape, the red dotted line represents the true frontal shape, and the blue dotted line represents the rear surface shape given both for Hata's method and the proposed method. Hata's method cannot estimate the shape of the hemisphere, while the proposed method successfully estimates it. The RMS error of surface normal in Hata's method was  $2.3^\circ$ , while that in the proposed method was  $0.3^\circ$ .

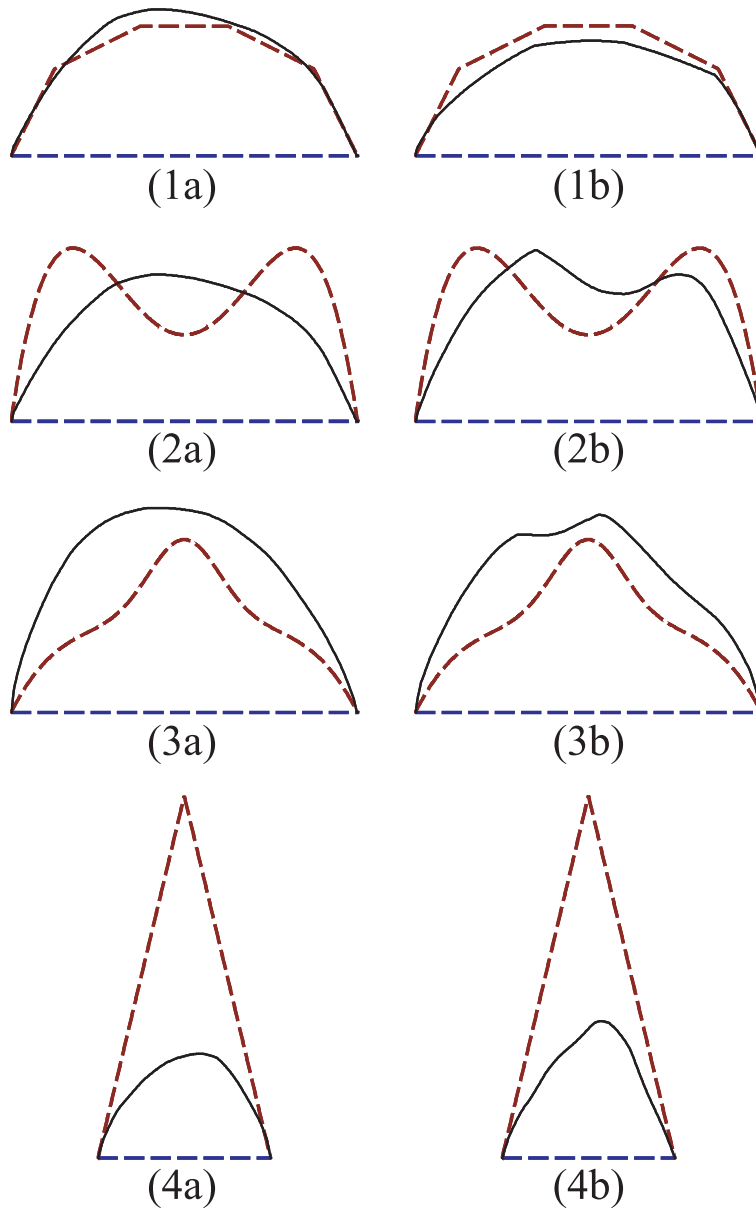


Figure 6.42: Results of Hata's method: (1)–(4)Result of hexagon shape, concave shape, bell shape, triangle shape, respectively, (a) initial shape, (b) result after 50 loops.

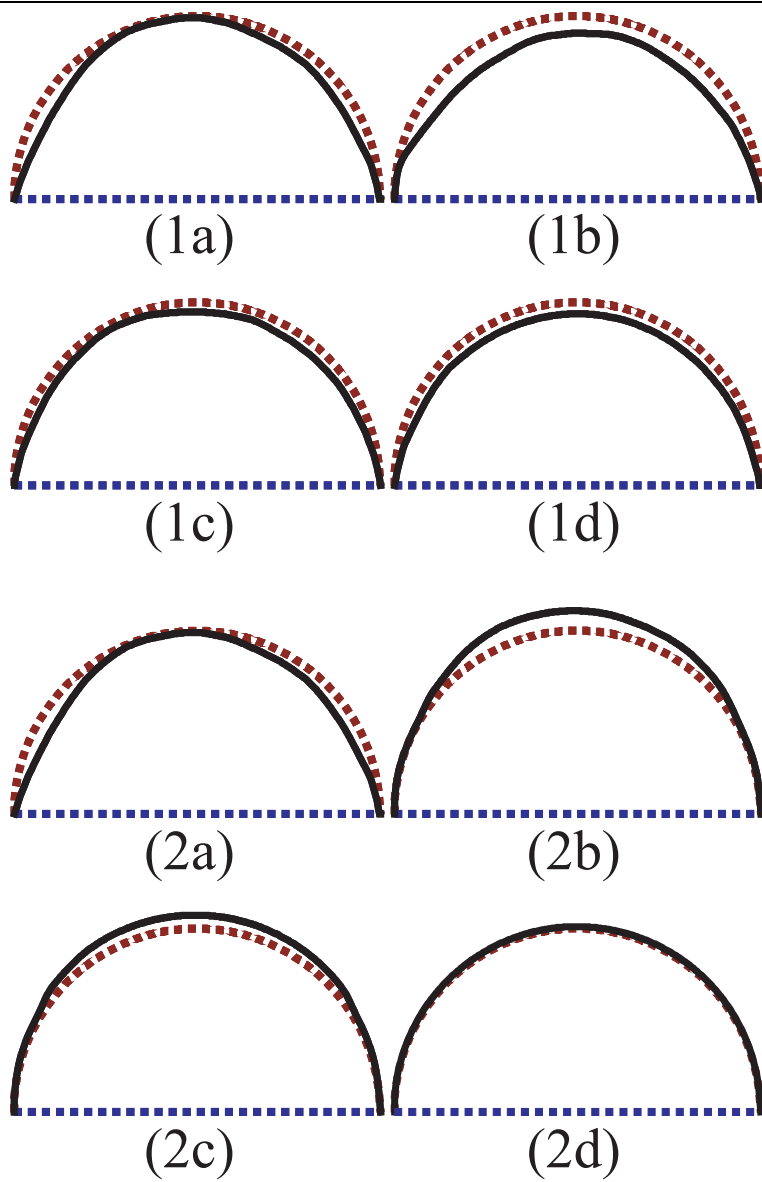


Figure 6.43: Comparison between Hata's method and proposed method: (1) Result of Hata's method, (2) result of proposed method; (a) Initial shape, (b)(c)(d) result after 1, 2, 50 loops, respectively.

---

## 6.4 Summary

I applied the method described in Chapter 3, Chapter 4, and Chapter 5 to estimate the surface shape of transparent objects, and presented the experimental result in Section 6.3.1, Section 6.3.2, and Section 6.3.3, respectively, by using the experimental setup shown in Section 6.1.

These experiments verify that the proposed methods can estimate the surface shape of transparent objects. My methods can be applied to general types of shapes, while Murase's method can only be applied to water surface, Ben-Ezra's method can only be applied to parametrized surface, Hata's method can only be applied to paste-like shapes, and Saito's method can only be applied to a shape whose abstract shape is known due to its ambiguity. Murase's paper showed the experimental result of estimating water surface, Ben-Ezra's method showed the experimental results of estimating spheres and rounded cubes, Hata's method showed the experimental result of estimating paste, and Saito's method showed the experimental results of estimating hemispheres and cones. Section 6.3.1 showed the experimental result of estimating hemispheres and shell-like shapes, Section 6.3.2 showed the experimental results of estimating hemispheres, heart shapes, bell shapes, and mountain shapes, and Section 6.3.3 showed the experimental results of estimating hemispheres, bell shapes, and jelly shapes.

Finally, Section 6.3.4 presented a result of Hata's method compared with the method proposed in Chapter 5. The accuracy of the proposed method was higher than that of Hata's method.

I will discuss the experimental results in greater detail as follows:

- Experimental setup of the visible light domain is shown in Section 6.1.1. This experimental setup is used for all three methods.

This system cannot obtain the polarization data in realtime; however, it can obtain the data in realtime by using the system that can measure the polarization data in realtime by using a liquid crystal [WMPA97, FTA+98, HC02].

The light sources illuminate a plastic sphere, which I denote as a spherical diffuser, and then the spherical diffuser behaves as a spherical light source and illuminates the target object, which is set in the center of the spherical diffuser. There is a hole on top of the spherical diffuser, and the transparent object is observed through the hole by the camera, which is set over the hole. This hole is a shortcoming of the experimental setup. The spherical diffuser behaves as a spherical light source except at the hole; in other words, the object is illuminated from all directions by the spherical diffuser except for the direction where the hole exists.

The non-illuminated part of the object due to the hole can be illuminated by observing

the object from a different direction. In addition, the precision of the measurement of the shape will improve by using multiple input data obtained by observing the object from different directions. However, it is difficult to observe the object from different directions by using the experimental setup depicted in Figure fig:cocoon due to the inflexibility of the system. An alternative approach is to rotate the object and fix the camera instead of moving the camera. The object will drop out the experimental setup if the object is rotated in a large angle; thus, the object is rotated only in a small angle. This limitation is still effective for the second method proposed in Chapter 4; however, this limitation is a serious issue for improving the precision of shape measurement by observing the object from many different viewpoints. I intend to use another kind of measurement system [SRS, FKIS02, Yam04, SOSI03], which is similar to “Light Stage” developed by Hawkins et al. [HCD01].

The target object must be sufficiently small compared to the spherical diffuser; thus, large objects are unmeasurable. The experimental setup in Figure 6.1 is unobtainable to others. Therefore, I intend to apply my methods without using the spherical diffuser and the light sources: measurement is also possible in both indoor and outdoor environments if the intensity and the polarization state of the surrounding environment is acquired beforehand.

- Experimental setup of the infrared light domain is shown in Section 6.1.2. This experimental setup is used for the first method proposed in Chapter 3.

The fact that the infrared light camera is more expensive than the visible light camera is somewhat of a problem.

The object must be carefully heated not to change the temperature of the object during the measurement.

- Experimental results of the first method proposed in Chapter 3 are shown in Section 6.3.1.

The method is applicable to transparent objects that have a complex shape such as shell-like shape.

The resultant shape has some noise at the part whose zenith angle  $\theta$  is around  $0^\circ$ ; points where the surface normal is heading towards the camera. This is caused by the hole on top of the spherical diffuser, a white plastic sphere surrounding the target object. This hole is necessary for the camera to observe the target object. The target object is illuminated by the spherical diffuser except for this hole. Therefore, the surface normal heading towards the camera is noisy because the light is not illuminated at such surface points.

- Experimental results of the second method proposed in Chapter 4 are shown in Section 6.3.2.

This second method, like the first method, does not consider the influence of internal interreflection, and thus provides an incorrect result. The measured degree of polarization is lowered in most cases compared to the expected degree of polarization, the value of which is calculated by assuming that the camera observes the light reflected at the object surface only once. If the degree of polarization is lowered, then the zenith angle, which is smaller than the Brewster angle, will be smaller. The angle shifts towards  $0^\circ$ , and the zenith angle, which is greater than Brewster angle, will be greater, that is, the angle shifts towards  $90^\circ$ . The observed area of the surface part whose zenith angle is smaller than the Brewster angle  $\theta_B$  is larger than that of the surface part whose zenith angle is greater than the Brewster angle. Therefore, the estimated height will be smaller than the true height.

This second method needs a region segmentation operation. I used a region-growing algorithm for implementation of the region segmentation. This algorithm requires the “seed” to be set by a human operator. Regions will “grow” from the seed. Implementing a region splitting and merging algorithm is better since it does not need any seeds to be input. This second method depends on the robustness of the region segmentation method. Due to the noise caused by internal interreflection, robust region segmentation is difficult. Therefore, this method cannot estimate the shape of shell-like object, because this object has a complex shape and region segmentation cannot be achieved so robustly.

The purpose of the first method and the second method is the same; they concentrate on solving the ambiguity problem. These two methods yield a pair of possible surface normals, whose values are same between these methods. The resultant surface normal seems to be the same between these methods; it is almost true, but it is not strictly true. The first method does not require region segmentation, while the second method does. Therefore, the resultant shape differs between these methods depending on the result of region segmentation. In most cases, the resultant shape of the first method is more precise than that of the second method due to the difficulty of region segmentation.

- Experimental results of the third method proposed in Chapter 5 are shown in Section 6.3.3.

This third method requires knowledge of the illumination distribution that surrounds the target object. The procedure to estimate the illumination distribution presented in Section 6.2.4 is an ad hoc one, and a more sophisticated procedure to estimate the

correct illumination distribution will be presented in future work. Still, this procedure does not take account of the hole on top of the spherical diffuser. The estimated surface normal that is heading towards the camera still has some errors. Correct illumination distributions or additional inputs from multiple directions are needed to recover the error of this surface normal.

The input polarization data is polluted by some noise due to the variation of the refractive index inside the object or the opacity of the object. If the variation of the refractive index and the opacity are known, the result will be more precise; however, such information is hard to obtain. A noise reduction process is effective in practice for such polluted input data. A first aid for noise reduction is to apply the noise reduction algorithms developed in the field of image processing: smoothing, median filtering, fitting polynomials or B-spline curves, and frequency-based methods such as Chebyshev approximation, Fourier analysis, and wavelet transformation. In order to reduce such noise fundamentally, multiple input data are needed, taken under different illumination or taken from different directions.

This third method requires much computation time for iterative computation due to the raytracing method which takes a lot of time computing time. Roughly speaking, there are three types of ideas to reduce the computation time of the raytracing method: bounding volume, voxel-based computing, and parallel computation. In this research, one object is analyzed for each computation. Bounding volume based raytracing method is not very effective. Bounding volume is created by splitting the object into several parts; however, the shape of the object deforms for each iteration steps, thus, bounding volume should be updated for each iteration step. I employed a similar approach to voxel-based computing; a square pillar based computing (*or* pixel-based computing). The object's shape in this research is represented as two height values set for each pixels; thus, it is better to split the object's shape into a square pillar per pixel than to split it into a voxel. While the conventional raytracing method searches all surface patches that the ray hits, this method compares two heights and the height of the ray per pixel. If there are 640 surface patches, the conventional raytracing method searches 640 times to find the surface patch where the ray hits, while this method uses, for example, only 10 surface patches if the ray hits at a certain surface patch when the ray steps forward for a 5 pixel length. In this research, parallel computation is not used: this will be used in future work.

If the initial shape is not appropriate, the iteration process will fall to a local minimum. As for the second method, two possible shapes are produced per one B-B region. If these two possible shapes are used as the initial shape, these shapes converge to two

different shapes; one is correct and one is incorrect. If the initial shape is similar to the true shape, then it will converge to a correct shape, but if the initial shape is similar to the wrong shape which is produced by the ambiguity of the degree of the polarization, then it will converge to an incorrect shape.

## CHAPTER 7

# CONCLUSION

### 7.1 Summary

In this thesis, I have proposed three methods for determining the shape of a transparent object by using a polarization filter. Surface normals are determined by using the polarization data. An algorithm that uses only one view in a visible light domain results in ambiguities. The first method solves this ambiguity problem by employing the polarization in an infrared light domain, and the second method solves it by employing the polarization of a slightly tilted view. These two methods still have a problem in that they do not consider internal interreflection. The third method solves this internal interreflection problem by employing a polarization raytracing algorithm. The ambiguity problem and the polarization raytracing algorithm are presented in Chapter 2.

**First method** The thermal radiation, which also has characteristics of polarization, can be observed as infrared light. This polarization is a one-valued function; measuring the degree of polarization in an infrared domain provides the unique zenith angle. However, the degree of polarization is relatively low, and in some cases it is difficult to determine the degree of polarization precisely. Therefore, I propose to use polarization in both visible and infrared light. This method is presented in Chapter 3.

**Second method** By rotating the object, the ambiguity problem can also be solved. Two sets of data are obtained: One is from the object not tilted, and the other is from the object tilted at a small angle. These data sets are segmented into some regions with regard to the Brewster angle. This method calculates the difference of the degree of polarization between these two sets of data at the corresponding point — the point where surface normal lies along the rotation direction and where the degree of polarization is minimal

in the B-B region. From that difference, the correct surface normal is determined. This method is presented in Chapter 4.

**Third method** Solving the inverse problem of the polarization raytracing method, the shape of transparent objects can be estimated more precisely. The polarization raytracing method considers internal interreflection. To obtain the shape of a transparent object, the method minimizes the difference between the input polarization data taken by observing the transparent object and the computed polarization data rendered by the polarization raytracing method. This method is presented in Chapter 5.

I have implemented these proposed methods, and demonstrated their abilities to determine the shape of transparent objects. First, I showed the experimental setup for obtaining the polarization data. Second, I explained the implementation details for calculating the polarization data. Finally, I demonstrated the ability of the proposed methods to determine the shapes of transparent objects by applying these methods to not only computer-generated transparent objects but also real transparent objects such as a transparent hemisphere and objects whose shapes are more complex than the hemisphere. Experiments are presented in Chapter 6.

## 7.2 Contribution

In this thesis, I proposed three methods to obtain the surface shape of a transparent object by using polarization analysis.

- The first method described in Chapter 3 estimates the shape of a transparent object by combining the knowledge of optics and thermodynamics. The method uses two kinds of input data; one is the polarization data of the reflected light in a visible light domain, and the other is the polarization data of the thermal radiation in an infrared light domain. First, I explained the relation between the surface normal of the object and the polarization state of the reflected light by using knowledge in the field of optics. Next, I explained the relation between the surface normal of the object and the polarization state of the thermal radiation by using knowledge in the field of optics and thermodynamics. The key idea of the method is that the relationship between the surface normal and the degree of polarization of reflected light is not one-to-one but that between the surface normal and the degree of polarization of thermal radiation is one-to-one; thus, the surface normal can be uniquely determined by these two kinds of polarization data. The key point of this research is that I combined the knowledge of different research fields (computer science, optics, and thermodynamics) and carried out an interdisci-

plinary research. This research is published in *Journal of Optical Society of America, A* [MSSI02].

- The second method described in Chapter 4 estimates the shape of a transparent object by combining the knowledge of optics and differential geometry. The method uses two pieces of polarization data obtained from two different views. First, I explained that the relationship between the surface normal and the degree of polarization of the reflected light observed from one view is not one-to-one. Next, I explained that the surface normal can be uniquely determined by comparing the degree of polarization obtained from two views at the same surface point. The key idea of the method is that the identical surface point in two pieces of polarization data can be determined even if the shape of the object is not known. The key point of this research is that I carried out an interdisciplinary research by combining the knowledge of different research fields (computer science, optics, and differential geometry), especially, I proved the validity of the algorithm, which searches the identical surface point, by relating the polarization data and the differential-geometrical property of the surface. This research is published in *IEEE Transactions on Pattern Analysis and Machine Intelligence* [MKI04].
- The third method described in Chapter 5 estimates the shape of a transparent object by solving the inverse problem of polarization raytracing. The method analyzes not only the reflected light but also the transmitted light obtained from one view. First, I explained the polarization raytracing algorithm, which is a combination of a conventional raytracing algorithm and Mueller calculus, in order to calculate the polarization state of the light. Next, I explained an iterative framework to compute the surface shape by minimizing the difference between the obtained polarization data and the rendered polarization data calculated by the polarization raytracing method. The key idea of the method is that the surface shape of the transparent object is calculated robustly by considering the multiple internal interreflections occurring inside the object. The key point of this research is that I solved the inverse problem of the polarization raytracing method. This research is now being prepared to be published in English journal. The research will be published in the proceedings of an international conference, *IEEE Computer Society International Conference on Computer Vision and Pattern Recognition* [MI05].

## 7.3 Discussion

### 7.3.1 Comparison between Three Proposed Methods

Advantages and disadvantages are listed in Table 7.1. The first method analyzes the polarization data in a visible light domain and an infrared light domain; thus, the method uses one visible light camera and one infrared light camera. The second method analyzes the polarization data obtained from two different views; thus, the method uses two visible light cameras, though I actually used one camera by rotating the object. The third method analyzes the polarization data obtained by one visible light camera. The third method provides precise estimation results by considering the internal interreflections, while the first and the second methods do not. The third method estimates the object's shape by an iterative computation; thus, it requires an initial value of the object shape, it takes a great deal of time to compute, and it is not so robust because it falls to a local minimum if the initial value is not good. The first and the second methods do not need an initial value and do not take so much time to compute. The second method is not so robust because it needs region segmentation, which is sensitive to noise, while the first method is robust because it does not need region segmentation or iterative computation. The experimental setup I used cannot measure the polarization data in realtime; however, some researchers proposed realtime measurement systems [WMPA97, FTA+98, HC02]. By using such realtime measurement equipment, the three proposed systems can possibly obtain the polarization data in realtime. However, the first method needs to observe the object from one direction with two different cameras; thus, it is difficult using this method to measure the polarization data in realtime.

The proposed three methods have both advantages and disadvantages as listed in Table 7.1. Thus, the best way to use these methods depends on the individual circumstances of each case. According to this table, examples of the usage of these methods will be like this:

- If you need a precise shape of a transparent object, then use the third method, which uses the polarization raytracing method (Chapter 5).
- If you need the shape of a transparent object quickly, then use the second method, with two cameras, which uses the differential geometrical property (Chapter 4).
- If you are intending to obtain the geometric data of a complex-shaped transparent object, and if the above two methods cannot calculate the complex shape, then use the first method, which uses the thermal radiation (Chapter 3).

	Method 1 (infrared)	Method 2 (geometry)	Method 3 (raytracing)
Camera	1 visible 1 infrared	2 visible	1 visible
Accuracy	low	low	high
Robustness	high	low	low
Computation time	quick	quick	long
Possibility of realtime measurement	NG	OK	OK
Initial value	no need	no need	need
Smooth surface ( $C^2$ ) measurable?	yes	yes	yes
Smooth surface ( $C^1$ ) measurable?	yes	possibly	yes
Continuous surface ( $C^0$ ) measurable?	possibly	no	possibly
Discontinuous surface measurable?	no	no	no

Table 7.1: Advantage and disadvantage of three methods.

### 7.3.2 Comparison with Other Methods

- My methods can estimate the shape of soft objects such as jelly or water surface, while haptic devices cannot estimate such soft objects.
- Murase's method [Mur92] observes the moving picture of the water surface and estimates the shape of the water surface. A picture laid on the bottom of the water is transmitted once at the water's surface and then observed by the camera. Optical flow is calculated from the deformation of the picture if the refractive index is given, and the surface shape of the water surface is estimated from the optical flow. Murase's method can only estimate the shape of the water surface; however, my methods can estimate various kinds of objects. In addition, my second and third methods can estimate the shape of the water surface if I use a realtime polarization camera [WMPA97, FTA+98, HC02].
- Hata's method [HSKK96](Section 6.3.4) illuminates the transparent object with a line-strip projector and observes a multiple picture for each line-strip light. The light transmits once at the object's surface, and it hits the white table beneath the object. This method computes the shape by a genetic algorithm from the deformation of the line-strip light under the assumption that the refractive index is given. Geometrical calibration is also needed: the position and the direction of the camera, the object, and the projector should be known. As shown in Section 6.3.4, Hata's method cannot measure a hemispherical transparent object with enough precision. Therefore, It seems to be difficult to estimate the shape of protruding objects such as a bell-shaped object shown in Section 6.3.2 and 6.3.3 by Hata's method. Also, it is more difficult to improve Hata's method in order to measure the object in realtime than my first and second method, since Hata's method needs the object to be illuminated by line-strip light while my methods can be used to measure the polarization state by using the realtime polarization camera.
- Ohara's method [OMOT03] estimates the depth of the edge of the object by using a shape-from-focus approach from multiple images taken by changing the focus of the camera. This method does not require the refractive index to be known. This method does not trace the light ray, and the computation itself can be done in realtime; however, it cannot obtain the input images in realtime since it should change the focus of the camera. Ohara's method can only estimate the depth of the edge of the object and cannot estimate the shape of a curved surface, while, my methods successfully estimate the shape of curved surfaces.
- Ben-Ezra's method [BN03] estimates the shape of transparent objects from multiple images taken from multiple directions. The background scene seen through a transparent

object deforms due to the refraction. By tracing the light ray for two or three transmissions, the deformation of the background scene can be calculated. By minimizing the difference between the calculated background scene seen through the object and the obtained background scene seen through the object, the shape of the transparent object can be computed. Multiple images taken from multiple directions are used for inputs. Ben-Ezra only estimated the shape that is represented by a small number of parameters such as a sphere (center position and radius) and rounded cube, while my methods can estimate more complex shapes, such as a heart-shaped object, a bell-shaped object, and a shellfish-shaped object.

- My research is based on Saito's method [SSIK99], which tried to estimate the surface shape of transparent objects by analyzing polarization. This method obtains three or more images under different polarized angles by observing the reflected light of the transparent object illuminated by a spherical diffuser. Then the degree of polarization is calculated, and an attempt is made to estimate the surface shape of the object with the refractive index known. However, Saito's method did not solve the ambiguity problem and could not determine the surface normal uniquely, while my first and second methods solved the ambiguity problem and determined the unique surface normal. My first method, my second method, and Saito's method did not consider multiple internal interreflections inside the transparent object; however, my third method did consider such internal interreflections and estimated the surface shape of transparent objects more precisely.
- The first method presented in Chapter 3 first obtains the polarization data of reflected light of the transparent object illuminated by spherical diffuser, then obtains the polarization data of thermal radiation of the transparent object heated by a hair dryer. Polarization data is calculated by three or more images taken under different polarizer angles. The image of reflected light and the image of thermal radiation are matched by 2D translation, rotation, and scaling. The surface shape is calculated directly from the degree of polarization with the refractive index known. The object should be observed from the same direction with two different cameras, one visible and one infrared; thus, realtime measurement is difficult.
- The second method presented in Chapter 4 obtains two sets of polarization data of reflected light of the transparent object illuminated by a spherical diffuser, taken from two different viewing directions. The directions of the two cameras should be known; however, the positions of the two cameras may be arbitrary. The surface shape is calculated directly from the degree of polarization with the refractive index known. Realtime

measurement is possible if we use realtime measurement systems [WMPA97, FTA+98, HC02].

- The third method presented in Chapter 5 obtains the polarization data of reflected light of the transparent object illuminated by spherical diffuser, taken from one viewing direction. Up to 100 reflections and transmissions of the light ray are calculated. The surface shape is calculated iteratively from the polarization data with the refractive index known. Realtime measurement is possible if we use realtime measurement systems [WMPA97, FTA+98, HC02].

Table 7.2 compares Murase's method, Hata's method, Ohara's method, Ben-Ezra's method, and Saito's method, with my three methods (denoted as 1–3 in this table).

## 7.4 Future Work

Future work in this area will be to obtain the shapes of transparent objects more accurately. It is impossible to analytically solve the inverse problem of polarization raytracing; thus, I estimated the transparent object's shape by an iterative computation by a method that uses the polarization raytracing method. I used a uniform illumination for that method; however, Hata et al. [HSKK96] estimated a transparent object's shape by an iterative computation where the object was illuminated by structured light. Ben-Ezra and Nayar [BN03] estimated the shape of a transparent object observed from many viewpoints by an iterative computation. Shape-from-silhouette (visual hull), which measures the object's shape from multiple views, has the defect that it cannot estimate a concave object; however, Nayar et al. [NIK91b], Wada et al. [WUM97], and Yang et al. [YZOS97] estimated the concave shape of an opaque object by iterative computation. To improve the precision of measuring the surface shape of transparent objects, I should probably observe the target object from multiple viewpoints or under various types of illumination. In any case, the iterative computation is considered to be necessary. The thesis provides the technique for measuring the surface shape of transparent objects using iterative computation, and this technique might be used as the basis for further developments.

I also intend to develop a method that can measure the refractive index at the same time, as well as the surface shape of a transparent object. I am now collaborating with industrial companies to provide my system to many people. By collaborating with Furuuchi Chemical Corporation, we developed a polarization camera [Fur] made from a material called PLZT. This PLZT polarization camera still cannot measure in realtime; however, we are trying to measure the polarization state of the light faster than existing realtime polarization cameras [WMPA97, FTA+98, HC02]. The future work is to develop a commercial product for measuring the shape of transparent object by collaborating with a camera manufacturer. I am

	Observed light	Light source	Views	Image per view
Murase	transmitted light	underwater picture	1	many
Hata	transmitted light	projector	1	many
Ohara	edge of object	ambient light	1	many
Ben-Ezra	transmitted light	background scene	many	1
Saito	reflected light	spherical diffuser	1	3
1	reflected light thermal radiation	spherical diffuser hair dryer	1 visible 1 IR	3
2	reflected light	spherical diffuser	2	3
3	reflected light transmitted light	spherical diffuser	1	3

	Geometrical calibration	Refractive index	Calculation method	Ray traced?
Murase	no need	need	optical flow	1 transmission
Hata	need	need	genetic algorithm	1 transmission
Ohara	no need	no need	shape from focus	0
Ben-Ezra	need	need	iteration	2-3 transmission
Saito	no need	need	direct	1 reflection
1	2D affine transformation	need	direct	1 reflection / 1 emission
2	direction of cameras	need	direct	1 reflection
3	no need	need	iteration	100 reflection & transmission

	Realtime measurable?	Realtime computable?	Hemisphere measurable?	Bell measurable?
Murase	yes	no	no	no
Hata	no	no	possibly	no
Ohara	no	yes	no	no
Ben-Ezra	yes	no	yes	no
Saito	yes	no	yes	no
1	no	yes	yes	yes
2	yes	possibly	yes	yes
3	yes	no	yes	yes

Table 7.2: Comparison between other methods.

also planning to collaborate with physicists to obtain some advice to make my methods more robust by using related knowledge in the field of physics.

There are many beautiful glass objects of art all over the world. These objects are hard but fragile, and are always in danger of destruction. Many methods are proposed for modeling works of cultural heritage [MON+00, IS01], but there are few methods proposed for modeling glass objects of art. The proposed method will be useful for this purpose.

Other application fields for the modeling of transparent objects can range from computer-aided manufacturing to classifying garbage/rubbish for recycling glass and plastic bottles to creating 3D catalogs for online shopping, etc. My basic technique for modeling the surface shape of transparent objects is the first step in this wide area of applications.

## APPENDIX A

# THEORY OF OPTICS

In this appendix, I will provide the theory of optics [BW59, Hec02, Shu62].

### A.1 Maxwell's Equations

Maxwell's equations for arbitrary mediums are,

$$\text{rot}\mathbf{E} = -\frac{\partial\mathbf{B}}{\partial t} \quad (\text{A.1})$$

$$\text{rot}\mathbf{H} = \mathbf{j} + \frac{\partial\mathbf{D}}{\partial t} \quad (\text{A.2})$$

$$\text{div}\mathbf{D} = \rho \quad (\text{A.3})$$

$$\text{div}\mathbf{B} = 0 \quad (\text{A.4})$$

where  $\mathbf{E}$  is electric vector,  $\mathbf{B}$  is magnetic induction,  $t$  is time,  $\mathbf{H}$  is magnetic vector,  $\mathbf{j}$  is electric current density,  $\mathbf{D}$  is electric displacement,  $\rho$  is charge density. These equations represents,

1. Faraday's electromagnetic induction law
2. Ampère's law
3. Gauss' law
4. magnetic monopole does not exist,

respectively. Following equations relates  $\mathbf{E}$  to  $\mathbf{D}$  and  $\mathbf{H}$  to  $\mathbf{B}$  respectively.

$$\mathbf{D} = \varepsilon_0\mathbf{E} + \mathbf{P} \quad (\text{A.5})$$

$$\mathbf{B} = \mu_0(\mathbf{H} + \mathbf{M}) \quad (\text{A.6})$$

where  $\mathbf{P}$  is electrolytic polarization,  $\mathbf{M}$  is magnetization,  $\varepsilon_0$  is dielectric permittivity of vacuum,  $\mu_0$  is magnetic permeability of vacuum.

Dielectric (*or* insulator) medium does not include electric charge, and does not produce electric current when electric field appears. For isotropic dielectrics, following equations hold.

$$\rho = 0 \quad (\text{A.7})$$

$$\mathbf{j} = 0 \quad (\text{A.8})$$

$$\mathbf{D} = \varepsilon \mathbf{E} \quad (\text{A.9})$$

$$\mathbf{B} = \mu \mathbf{H} \quad (\text{A.10})$$

Therefore, Maxwell's equations for isotropic dielectrics (include vacuum) will be,

$$\text{rot} \mathbf{E} = -\mu \frac{\partial \mathbf{H}}{\partial t} \quad (\text{A.11})$$

$$\text{rot} \mathbf{H} = \varepsilon \frac{\partial \mathbf{E}}{\partial t} \quad (\text{A.12})$$

$$\text{div} \mathbf{E} = 0 \quad (\text{A.13})$$

$$\text{div} \mathbf{H} = 0 \quad (\text{A.14})$$

where  $\varepsilon$  is dielectric permittivity, and  $\mu$  is magnetic permeability.

Following equations are defined in the research field of vector analysis.

$$\nabla \mathbf{A} = \text{grad} \mathbf{A} = \begin{pmatrix} \frac{\partial A_x}{\partial x} \\ \frac{\partial A_y}{\partial y} \\ \frac{\partial A_z}{\partial z} \end{pmatrix} \quad (\text{A.15})$$

$$\nabla \times \mathbf{A} = \text{rot} \mathbf{A} = \text{curl} \mathbf{A} = \begin{pmatrix} \frac{\partial A_z}{\partial y} - \frac{\partial A_y}{\partial z} \\ \frac{\partial A_x}{\partial z} - \frac{\partial A_z}{\partial x} \\ \frac{\partial A_y}{\partial x} - \frac{\partial A_x}{\partial y} \end{pmatrix} \quad (\text{A.16})$$

$$\nabla \cdot \mathbf{A} = \text{div} \mathbf{A} = \frac{\partial A_x}{\partial x} + \frac{\partial A_y}{\partial y} + \frac{\partial A_z}{\partial z} \quad (\text{A.17})$$

$$\nabla^2 \mathbf{A} = \Delta \mathbf{A} = \frac{\partial^2 A_x}{\partial x^2} + \frac{\partial^2 A_y}{\partial y^2} + \frac{\partial^2 A_z}{\partial z^2} \quad (\text{A.18})$$

where

$$\mathbf{A} = \begin{pmatrix} A_x \\ A_y \\ A_z \end{pmatrix} .$$

From above equations, the following equation can be derived.

$$\text{rot rot} = \text{grad div} - \nabla^2 . \quad (\text{A.19})$$

By calculating  $\partial/\partial t$  of both sides of Equation (A.11), I obtain the following equation by using Equations (A.12), (A.14) and (A.19).

$$\begin{aligned} -\mu \frac{\partial^2 \mathbf{H}}{\partial t^2} &= \frac{\partial}{\partial t}(\text{rot} \mathbf{E}) \\ &= \text{rot} \frac{\partial \mathbf{E}}{\partial t} \\ &= \frac{1}{\varepsilon} \text{rot}(\text{rot} \mathbf{H}) \\ &= \frac{1}{\varepsilon} (\text{grad}(\text{div} \mathbf{H}) - \nabla^2 \mathbf{H}) \\ &= -\frac{1}{\varepsilon} \nabla^2 \mathbf{H} . \end{aligned} \quad (\text{A.20})$$

Therefore,

$$\nabla^2 \mathbf{H} = \varepsilon \mu \frac{\partial^2 \mathbf{H}}{\partial t^2} . \quad (\text{A.21})$$

Similarly,

$$\nabla^2 \mathbf{E} = \varepsilon \mu \frac{\partial^2 \mathbf{E}}{\partial t^2} . \quad (\text{A.22})$$

These equations are wave equation which is ordinarily expressed as,

$$\nabla^2 \mathbf{A} = \frac{1}{v^2} \frac{\partial^2 \mathbf{A}}{\partial t^2} , \quad (\text{A.23})$$

where  $v$  is the propagating speed of the wave. Therefore, the speed of electromagnetic wave will be,

$$v = \frac{1}{\sqrt{\varepsilon \mu}} . \quad (\text{A.24})$$

By denoting  $\varepsilon_0$  as the  $\varepsilon$  in vacuum and  $\mu_0$  as the  $\mu$  in vacuum, the light speed  $c$  in vacuum can be expressed as,

$$c = \frac{1}{\sqrt{\varepsilon_0 \mu_0}} . \quad (\text{A.25})$$

In almost all mediums except for magnetic mediums,  $\mu = \mu_0$  holds. The ratio of the light speed in vacuum to that in the medium is called refractive index of the medium.

$$n = \frac{c}{v} = \sqrt{\frac{\varepsilon}{\varepsilon_0}} . \quad (\text{A.26})$$

## A.2 Electric Field and Magnetic Field

Plane wave is expressed as,

$$\mathbf{A} \exp\{-i(\omega t - \mathbf{k} \cdot \mathbf{r})\} \quad , \quad (\text{A.27})$$

where  $\mathbf{A}$  is amplitude,  $i$  is an imaginary number,  $\omega$  is angular frequency,  $t$  is time,  $\mathbf{k}$  is wave vector (*or* propagation vector),  $\mathbf{r}$  is position vector. From the definition of wave,  $\omega = 2\pi\nu$ ,  $v = \lambda\nu$  and  $\lambda_0 = n\lambda$ , where  $\nu$  is frequency,  $\lambda$  is wavelength,  $\lambda_0$  is that in vacuum and  $n$  is refractive index. Wave vector is defined as  $\mathbf{k} = k\mathbf{n}$ , where  $k$  is wave number and  $\mathbf{n}$  is the unit vector which represents the direction of the propagation of the wave.

$$k = \frac{\omega}{v} = \frac{2\pi}{\lambda} = \frac{2\pi n}{\lambda_0} = \omega\sqrt{\epsilon\mu_0} \quad . \quad (\text{A.28})$$

From,

$$\mathbf{k} = \begin{pmatrix} k_x \\ k_y \\ k_z \end{pmatrix} , \quad \mathbf{n} = \begin{pmatrix} x \\ y \\ z \end{pmatrix} ,$$

I can derive,

$$\frac{\partial \mathbf{k} \cdot \mathbf{r}}{\partial x} = k_x , \quad \frac{\partial \mathbf{k} \cdot \mathbf{r}}{\partial y} = k_y , \quad \frac{\partial \mathbf{k} \cdot \mathbf{r}}{\partial z} = k_z \quad . \quad (\text{A.29})$$

The electric field and the magnetic field of plane wave is expressed as,

$$\mathbf{E} = \mathbf{E}_0 \exp\{-i(\omega t - \mathbf{k} \cdot \mathbf{r})\} \quad (\text{A.30})$$

$$\mathbf{H} = \mathbf{H}_0 \exp\{-i(\omega t - \mathbf{k} \cdot \mathbf{r})\} \quad , \quad (\text{A.31})$$

where  $\mathbf{E}_0$  and  $\mathbf{H}_0$  are constant complex vector. By calculating  $\partial/\partial t$  of  $\mathbf{E}$  and  $\mathbf{H}$ , I obtain,

$$\frac{\partial \mathbf{E}}{\partial t} = -i\omega \mathbf{E} \quad (\text{A.32})$$

$$\frac{\partial \mathbf{H}}{\partial t} = -i\omega \mathbf{H} \quad . \quad (\text{A.33})$$

I denote the  $x$ -component of  $\text{rot}\mathbf{E}$  as  $(\text{rot}\mathbf{E})_x$  and I obtain,

$$\begin{aligned} (\text{rot}\mathbf{E})_x &= \frac{\partial E_z}{\partial y} - \frac{\partial E_y}{\partial z} \\ &= i(k_y E_z - k_z E_y) \\ &= i(\mathbf{k} \times \mathbf{E})_x \quad . \end{aligned} \quad (\text{A.34})$$

Similarly I obtain,

$$(\text{rot}\mathbf{E})_y = i(\mathbf{k} \times \mathbf{E})_y , \quad (\text{rot}\mathbf{E})_z = i(\mathbf{k} \times \mathbf{E})_z \quad . \quad (\text{A.35})$$

Therefore,

$$\text{rot}\mathbf{E} = i\mathbf{k} \times \mathbf{E} \quad . \quad (\text{A.36})$$

By applying the above derivation to  $\mathbf{H}$ , I also obtain,

$$\text{rot}\mathbf{H} = i\mathbf{k} \times \mathbf{H} \quad . \quad (\text{A.37})$$

By substituting Equation (A.36) and (A.33) into Equation (A.11), I obtain,

$$\mathbf{k} \times \mathbf{E} = \omega\mu\mathbf{H} \quad . \quad (\text{A.38})$$

By substituting Equation (A.37) and (A.32) into Equation (A.12), I obtain,

$$\mathbf{k} \times \mathbf{H} = -\omega\varepsilon\mathbf{E} \quad . \quad (\text{A.39})$$

By calculating the dot product of  $\mathbf{k}$  with Equations (A.38), (A.39), I obtain,

$$\begin{aligned} \mathbf{E} \cdot \mathbf{k} &= -\frac{1}{\omega\varepsilon}(\mathbf{k} \times \mathbf{H}) \cdot \mathbf{k} = 0 \\ \mathbf{H} \cdot \mathbf{k} &= \frac{1}{\omega\mu}(\mathbf{k} \times \mathbf{E}) \cdot \mathbf{k} = 0 \end{aligned} \quad . \quad (\text{A.40})$$

These equations indicates that the oscillation of the electric field  $\mathbf{E}$  and the magnetic field  $\mathbf{H}$  is orthogonal to the propagation direction  $\mathbf{k}$ , concluding that light is a transversal wave. From Equation (A.38) or (A.39), I obtain,

$$\mathbf{E} \cdot \mathbf{H} = -\frac{1}{\omega\varepsilon}\mathbf{H} \cdot (\mathbf{k} \times \mathbf{H}) = \frac{1}{\omega\mu}\mathbf{E} \cdot (\mathbf{k} \times \mathbf{E}) = 0 \quad . \quad (\text{A.41})$$

Therefore,  $\mathbf{E}$  and  $\mathbf{H}$  is also orthogonal. By calculating the absolute value of both sides of Equation (A.38) or (A.39) using Equation (A.28), I obtain,

$$\sqrt{\varepsilon}|\mathbf{E}| = \sqrt{\mu_0}|\mathbf{H}| \quad . \quad (\text{A.42})$$

### A.3 Poynting Vector and Intensity

Poynting vector is defined as,

$$\mathbf{S} = \mathbf{E} \times \mathbf{H} \quad . \quad (\text{A.43})$$

This represents the propagation direction and the instantaneous energy density per unit time and per unit area, propagates by the electromagnetic field. I call the light energy per unit time and per unit area as intensity and represent as  $I$ .  $I$  is expressed as  $I = \langle |\mathbf{S}| \rangle$ , where  $\langle \rangle$

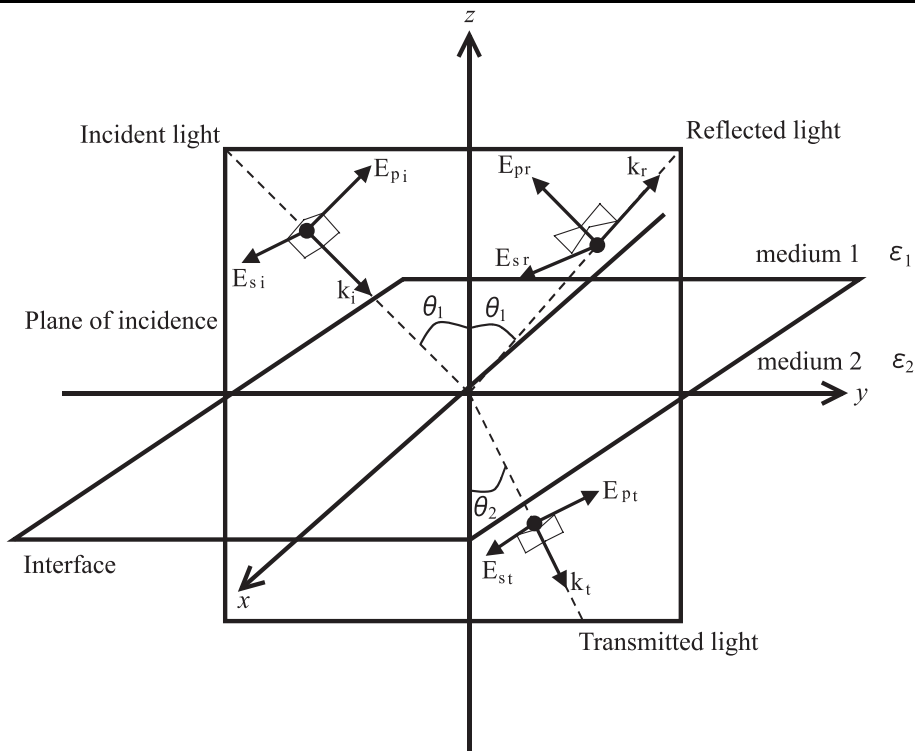


Figure A.1: Electric vector.

represents the time average.

$$\begin{aligned}
 I &= \langle |\mathbf{S}| \rangle \\
 &= \frac{1}{2} |\mathbf{E}| |\mathbf{H}| \\
 &= \frac{1}{2} \sqrt{\frac{\varepsilon}{\mu_0}} |\mathbf{E}|^2 \\
 &= \frac{n}{2} \sqrt{\frac{\varepsilon_0}{\mu_0}} |\mathbf{E}|^2 .
 \end{aligned} \tag{A.44}$$

## A.4 Fresnel Formulae

Consider the interface of medium 1 (dielectric permittivity  $\varepsilon_1$ ) and medium 2 (dielectric permittivity  $\varepsilon_2$ ) lies in the  $xy$ -plane and the plane of incidence lies in the  $yz$ -plane (Figure A.1 and Figure A.2). (Note: This definition is different from Figure 2.1.) I denote the incident

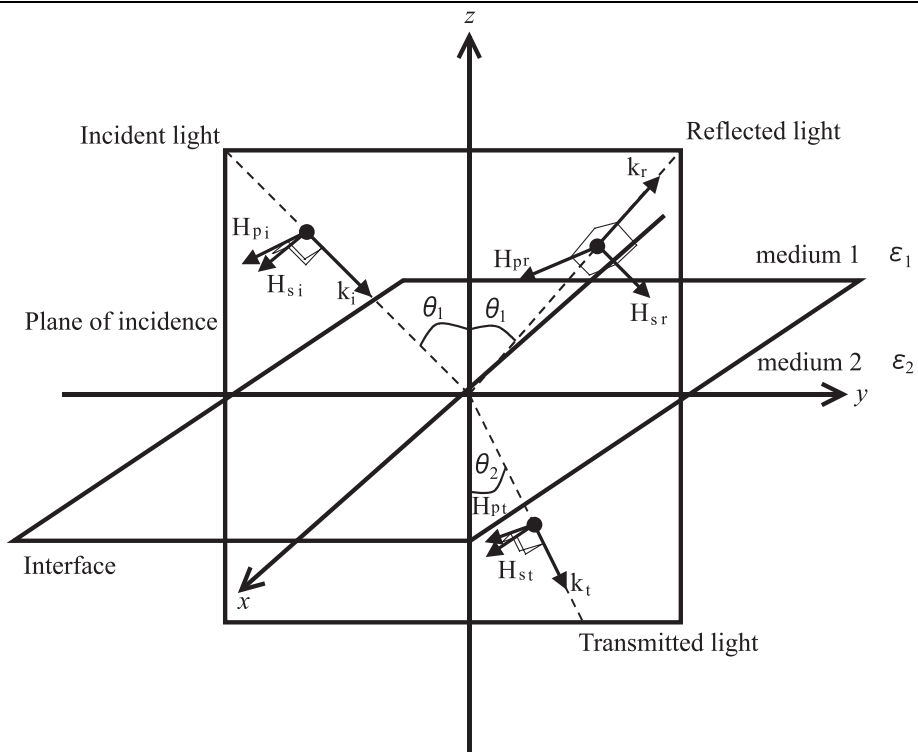


Figure A.2: Magnetic vector.

angle, the reflecting angle, the transmitting angle, as  $\theta_1, \theta_1, \theta_2$ , respectively. The electric amplitude of the incident light, the reflected light, the transmitted light is denoted as  $\mathbf{E}_{0i}, \mathbf{E}_{0r}, \mathbf{E}_{0t}$ , respectively, and the magnetic amplitude of those are denoted as  $\mathbf{H}_{0i}, \mathbf{H}_{0r}, \mathbf{H}_{0t}$ , respectively. I divide these lights in  $p$ -component, which is parallel to the plane of incidence, and  $s$ -component, which is parallel to  $x$ -axis. Then the light can be expressed as the following vectors.

$$\mathbf{E}_{0i} = \begin{pmatrix} E_s^i \\ E_p^i \cos \theta_1 \\ E_p^i \sin \theta_1 \end{pmatrix}, \quad \mathbf{E}_{0r} = \begin{pmatrix} E_s^r \\ -E_p^r \cos \theta_1 \\ E_p^r \sin \theta_1 \end{pmatrix}, \quad \mathbf{E}_{0t} = \begin{pmatrix} E_s^t \\ E_p^t \cos \theta_2 \\ E_p^t \sin \theta_2 \end{pmatrix} \quad (\text{A.45})$$

$$\mathbf{H}_{0i} = \begin{pmatrix} H_p^i \\ -H_s^i \cos \theta_1 \\ -H_s^i \sin \theta_1 \end{pmatrix}, \quad \mathbf{H}_{0r} = \begin{pmatrix} H_p^r \\ H_s^r \cos \theta_1 \\ -H_s^r \sin \theta_1 \end{pmatrix}, \quad \mathbf{H}_{0t} = \begin{pmatrix} H_p^t \\ -H_s^t \cos \theta_2 \\ -H_s^t \sin \theta_2 \end{pmatrix}. \quad (\text{A.46})$$

At the interface  $z = 0$ , because of the continuity of the light wave, the sum of the amplitude of the incident light and the reflected light, which both are in the medium 1, must be equal to the amplitude of the transmitted light, which is in the medium 2, for each  $x$ -component and  $y$ -component. Therefore, the following equations hold.

$$E_s^i + E_s^r = E_s^t \quad (\text{A.47})$$

$$E_p^i \cos \theta_1 - E_p^r \cos \theta_1 = E_p^t \cos \theta_2 \quad (\text{A.48})$$

$$H_p^i + H_p^r = H_p^t \quad (\text{A.49})$$

$$H_s^i \cos \theta_1 - H_s^r \cos \theta_1 = H_s^t \cos \theta_2 \quad (\text{A.50})$$

By substituting  $H = \sqrt{\varepsilon/\mu_0}E$  and Snell's law  $\sqrt{\varepsilon_1} \sin \theta_1 = \sqrt{\varepsilon_2} \sin \theta_2$ , the above equations can be rewritten as,

$$E_s^i + E_s^r = E_s^t \quad (\text{A.51})$$

$$(E_p^i - E_p^r) \cos \theta_1 = E_p^t \cos \theta_2 \quad (\text{A.52})$$

$$(E_p^i + E_p^r) \sin \theta_2 = E_p^t \sin \theta_1 \quad (\text{A.53})$$

$$(E_s^i - E_s^r) \tan \theta_2 = E_s^t \tan \theta_1 \quad (\text{A.54})$$

The ratio of the amplitude of the reflected light to that of the incident light is called amplitude reflectivity, and the ratio of the amplitude of the transmitted light to that of the incident light is called amplitude transmissivity. The amplitude reflectivity  $r$  and the amplitude transmissivity  $t$  of  $p$ -component and  $s$ -component is defined as,

$$r_p = \frac{E_p^r}{E_p^i}, \quad r_s = \frac{E_s^r}{E_s^i}, \quad t_p = \frac{E_p^t}{E_p^i}, \quad t_s = \frac{E_s^t}{E_s^i}. \quad (\text{A.55})$$

From Equation (A.52) and (A.53),

$$E_p^t = (E_p^i - E_p^r) \frac{\cos \theta_1}{\cos \theta_2} = (E_p^i + E_p^r) \frac{\sin \theta_2}{\sin \theta_1} \quad (\text{A.56})$$

$$\text{i.e. } (1 - r_p) \sin \theta_1 \cos \theta_1 = (1 + r_p) \sin \theta_2 \cos \theta_2 \quad (\text{A.57})$$

Therefore,

$$\begin{aligned} r_p &= \frac{\sin \theta_1 \cos \theta_1 - \sin \theta_2 \cos \theta_2}{\sin \theta_1 \cos \theta_1 + \sin \theta_2 \cos \theta_2} \\ &= \frac{\sin 2\theta_1 - \sin 2\theta_2}{\sin 2\theta_1 + \sin 2\theta_2} \\ &= \frac{\cos(\theta_1 + \theta_2) \sin(\theta_1 - \theta_2)}{\sin(\theta_1 + \theta_2) \cos(\theta_1 - \theta_2)} \\ &= \frac{\tan(\theta_1 - \theta_2)}{\tan(\theta_1 + \theta_2)} \end{aligned} \quad (\text{A.58})$$

From Equation (A.51) and (A.54),

$$E_s^t = E_s^i + E_s^r = (E_s^i - E_s^r) \frac{\tan \theta_2}{\tan \theta_1} \quad (\text{A.59})$$

$$\text{i.e. } (1 + r_s) \tan \theta_1 = (1 - r_s) \tan \theta_2 \quad (\text{A.60})$$

Therefore,

$$\begin{aligned} r_s &= -\frac{\tan \theta_1 - \tan \theta_2}{\tan \theta_1 + \tan \theta_2} \\ &= -\frac{\sin \theta_1 \cos \theta_2 - \cos \theta_1 \sin \theta_2}{\sin \theta_1 \cos \theta_2 + \cos \theta_1 \sin \theta_2} \\ &= -\frac{\sin(\theta_1 + \theta_2) + \sin(\theta_1 - \theta_2) - \sin(\theta_1 + \theta_2) + \sin(\theta_1 - \theta_2)}{\sin(\theta_1 + \theta_2) + \sin(\theta_1 - \theta_2) + \sin(\theta_1 + \theta_2) - \sin(\theta_1 - \theta_2)} \\ &= -\frac{\sin(\theta_1 - \theta_2)}{\sin(\theta_1 + \theta_2)} \end{aligned} \quad (\text{A.61})$$

From Equation (A.52) and (A.53),

$$E_p^r = E_p^i - E_p^t \frac{\cos \theta_2}{\cos \theta_1} = -E_p^i + E_p^t \frac{\sin \theta_1}{\sin \theta_2} \quad (\text{A.62})$$

$$\text{i.e. } \cos \theta_1 \sin \theta_2 - t_p \cos \theta_2 \sin \theta_2 = -\sin \theta_2 \cos \theta_1 + t_p \sin \theta_1 \cos \theta_1 \quad (\text{A.63})$$

Therefore,

$$\begin{aligned} t_p &= \frac{2 \sin \theta_2 \cos \theta_1}{\sin \theta_1 \cos \theta_1 + \sin \theta_2 \cos \theta_2} \\ &= \frac{2 \sin \theta_2 \cos \theta_1}{\frac{1}{2} \sin 2\theta_1 + \frac{1}{2} \sin 2\theta_2} \\ &= \frac{2 \sin \theta_2 \cos \theta_1}{\sin(\theta_1 + \theta_2) \cos(\theta_1 - \theta_2)} \end{aligned} \quad (\text{A.64})$$

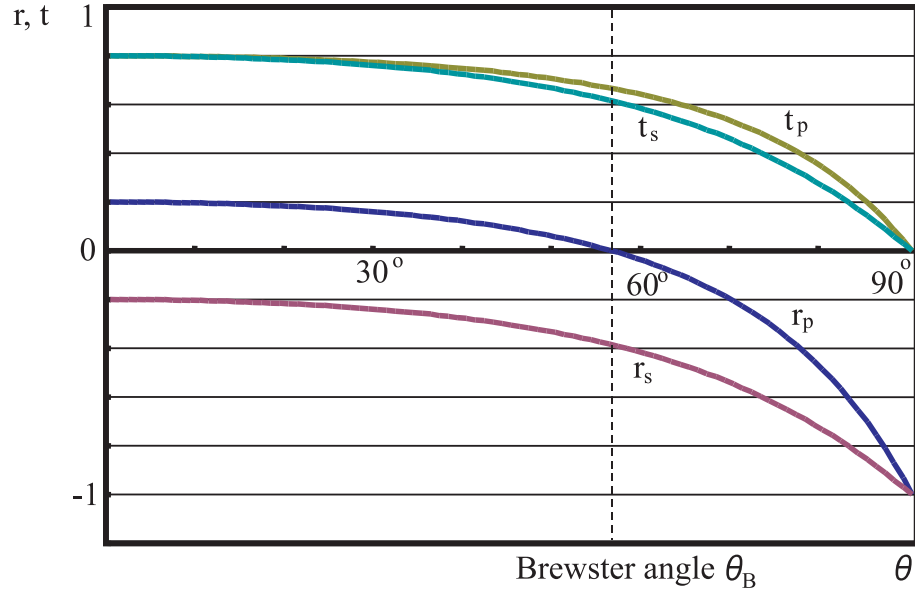


Figure A.3: Amplitude reflectivity and amplitude transmissivity.

From Equation (A.51) and (A.54),

$$E_s^r = E_s^t - E_s^i = E_s^i - E_s^t \frac{\tan \theta_1}{\tan \theta_2} \quad (\text{A.65})$$

$$\text{i.e. } (t_s - 1) \tan \theta_2 = \tan \theta_2 - t_s \tan \theta_1 \quad (\text{A.66})$$

Therefore,

$$\begin{aligned} t_s &= \frac{2 \tan \theta_2}{\tan \theta_1 + \tan \theta_2} \\ &= \frac{2 \sin \theta_2 \cos \theta_1}{\sin \theta_1 \cos \theta_2 + \cos \theta_1 \sin \theta_2} \\ &= \frac{2 \sin \theta_2 \cos \theta_1}{\frac{1}{2} \sin(\theta_1 + \theta_2) + \frac{1}{2} \sin(\theta_1 - \theta_2) + \frac{1}{2} \sin(\theta_1 + \theta_2) - \frac{1}{2} \sin(\theta_1 - \theta_2)} \\ &= \frac{2 \sin \theta_2 \cos \theta_1}{\sin(\theta_1 + \theta_2)} \quad (\text{A.67}) \end{aligned}$$

Equations (A.58), (A.61), (A.64), (A.67) are called Fresnel's law (Figure A.3).

## A.5 Derivation of Intensity Ratio

The light energy at the interface per unit area is expressed by using Equation (A.44) as,

$$\text{Incident Light } I_i = \frac{n_1}{2} \sqrt{\frac{\varepsilon_0}{\mu_0}} E_{0i}^2 \cos \theta_1 \quad (\text{A.68})$$

$$\text{Reflected Light } I_r = \frac{n_1}{2} \sqrt{\frac{\varepsilon_0}{\mu_0}} E_{0r}^2 \cos \theta_1 \quad (\text{A.69})$$

$$\text{Transmitted Light } I_t = \frac{n_2}{2} \sqrt{\frac{\varepsilon_0}{\mu_0}} E_{0t}^2 \cos \theta_2 \quad (\text{A.70})$$

The intensity reflectivity of  $p$ -component  $F_p$  and that of  $s$ -component  $F_s$  are,

$$F_p = \left( \frac{I_r}{I_i} \right)_p = \left( \frac{E_{0r}}{E_{0i}} \right)_p^2 = r_p^2 \quad (\text{A.71})$$

$$F_s = \left( \frac{I_r}{I_i} \right)_s = \left( \frac{E_{0r}}{E_{0i}} \right)_s^2 = r_s^2 \quad (\text{A.72})$$

From this equations and Equation (A.58) and (A.61), I can derive Equation (2.2).

The intensity transmissivity of  $p$ -component  $T_p$  and that of  $s$ -component  $T_s$  are,

$$T_p = \left( \frac{I_t}{I_i} \right)_p = \left( \frac{E_{0t}}{E_{0i}} \right)_p^2 \frac{n_2 \cos \theta_2}{n_1 \cos \theta_1} = \frac{n_2 \cos \theta_2}{n_1 \cos \theta_1} t_p^2 \quad (\text{A.73})$$

$$T_s = \left( \frac{I_t}{I_i} \right)_s = \left( \frac{E_{0t}}{E_{0i}} \right)_s^2 \frac{n_2 \cos \theta_2}{n_1 \cos \theta_1} = \frac{n_2 \cos \theta_2}{n_1 \cos \theta_1} t_s^2 \quad (\text{A.74})$$

From this equations and Equation (A.64) and (A.67) and Snell's law  $n_1 \sin \theta_1 = n_2 \sin \theta_2$ , I can derive Equation (3.5).

## A.6 Graph of Intensity Ratio

By substituting Snell's law into Equation (2.2), I obtain,

$$F_p = \frac{1 + n^2 - (n^2 + 1/n^2) \sin^2 \theta - 2 \cos \theta \sqrt{n^2 - \sin^2 \theta}}{1 + n^2 - (n^2 + 1/n^2) \sin^2 \theta + 2 \cos \theta \sqrt{n^2 - \sin^2 \theta}} \quad (\text{A.75})$$

$$F_s = \frac{1 + n^2 - 2 \sin^2 \theta - 2 \cos \theta \sqrt{n^2 - \sin^2 \theta}}{1 + n^2 - 2 \sin^2 \theta + 2 \cos \theta \sqrt{n^2 - \sin^2 \theta}} \quad (\text{A.76})$$

By substituting Snell's law into Equation (3.5), I obtain,

$$T_p = \frac{4 \cos \theta \sqrt{n^2 - \sin^2 \theta}}{1 + n^2 - (n^2 + 1/n^2) \sin^2 \theta + 2 \cos \theta \sqrt{n^2 - \sin^2 \theta}} \quad (\text{A.77})$$

$$T_s = \frac{4 \cos \theta \sqrt{n^2 - \sin^2 \theta}}{1 + n^2 - 2 \sin^2 \theta + 2 \cos \theta \sqrt{n^2 - \sin^2 \theta}} \quad (\text{A.78})$$

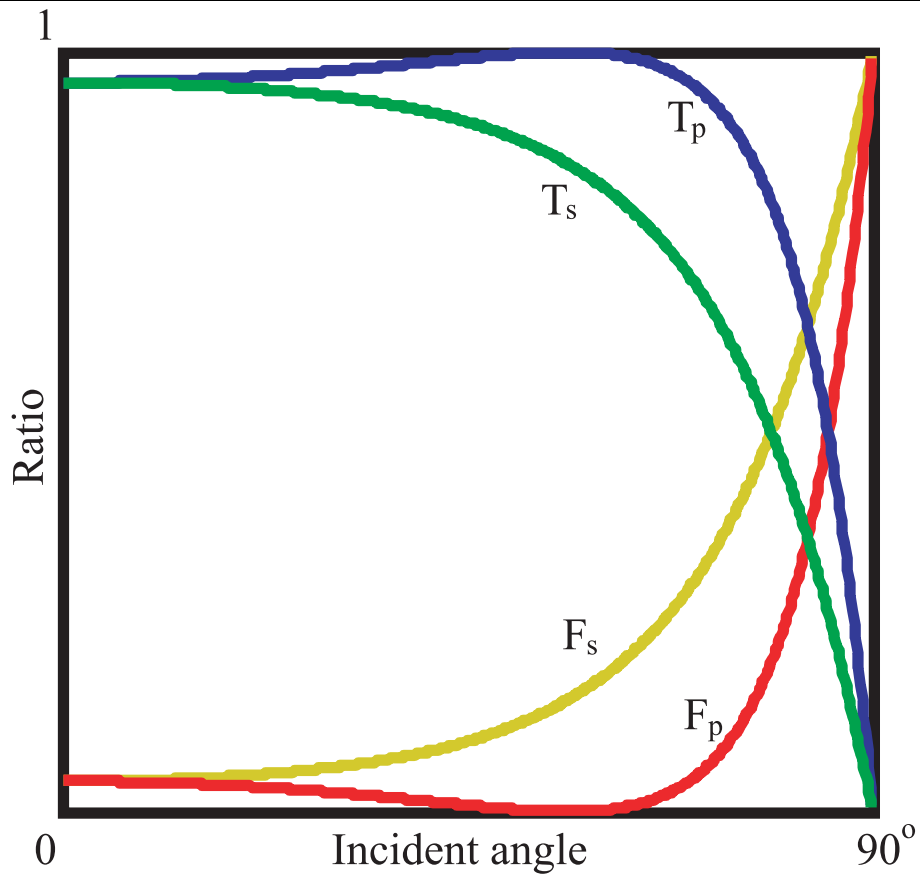


Figure A.4: Graphs of intensity ratios.

These graphs are depicted in Figure A.4. The graphs with the tags written as  $F_p$  and  $F_s$  are the graphs of the parallel and perpendicular intensity ratios of reflection, respectively. The graphs with the tags written as  $T_p$  and  $T_s$  are the graphs of the parallel and perpendicular intensity ratios of transmission, respectively.

## APPENDIX B

# GAUSSIAN GEOMETRY

In this appendix, I will present a basic theory of differential geometry [Car76, Hor86, Koe90].

### B.1 Gaussian Mapping

Consider translating the starting point of the unit surface normal vector  $\mathbf{n}_P$  at the point P of the surface  $S$  to the origin of the coordinate axes. Therefore, the end of the unit surface normal vector lies on an unit sphere and let us denote this point as  $g(P)$ . I call the mapping,

$$g : S \longrightarrow \text{unit sphere} \tag{B.1}$$

as Gaussian mapping. Figure B.1 depicts a Gaussian mapping.

I will explain in more detail (Figure B.2).

The Gaussian mapping of a sphere whose radius is  $R$  is depicted in Figure B.2(a). The point P and Q of the sphere maps onto the point  $g(P)$  and  $g(Q)$ , respectively, on unit sphere, where each surface normal is the same. Scaling the sphere of radius  $R$  to an unit sphere will be the Gaussian mapping, namely, the similarity mapping of similarity ratio  $1/R$  will be the Gaussian mapping.

The Gaussian mapping of a kind of a lemon is depicted in Figure B.2(b). The upper part of the lemon is scale-downed by Gaussian mapping near to the north pole of the unit sphere, while, the sharp part of the lemon extends by Gaussian mapping to almost an half of the unit sphere. You will see that the degree of curving surfaces is in proportion to the scale of the mapped part of the unit sphere to the surface part.

How the elliptic surface maps onto the unit sphere by Gaussian mapping was shown in Figure B.2(b), whereas, how the hyperbolic surface maps onto the unit sphere by Gaussian mapping is shown in Figure B.2(c). The left and the right part around P maps inversely to

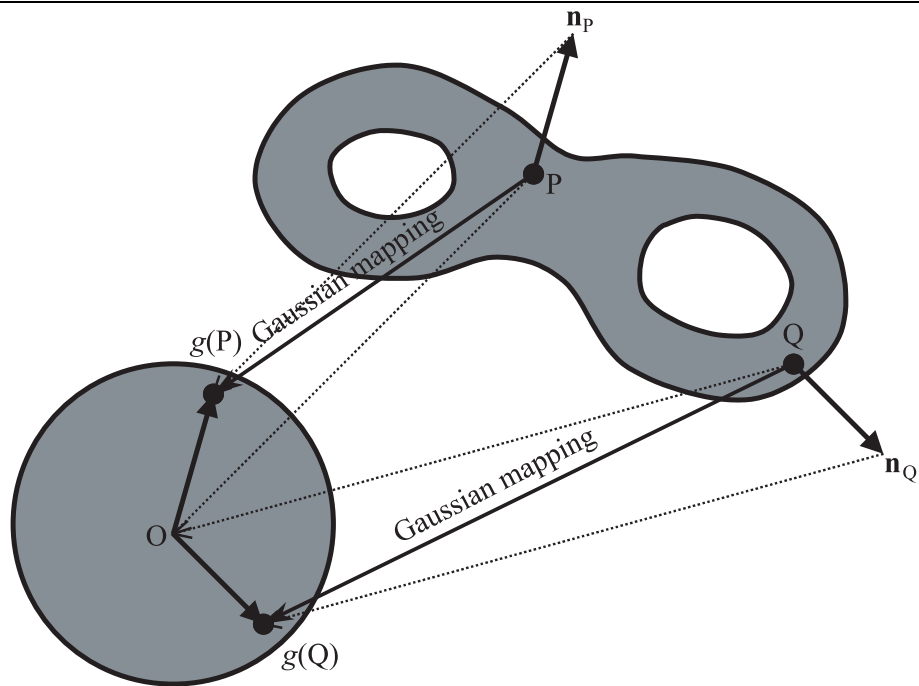


Figure B.1: Gaussian mapping.

---

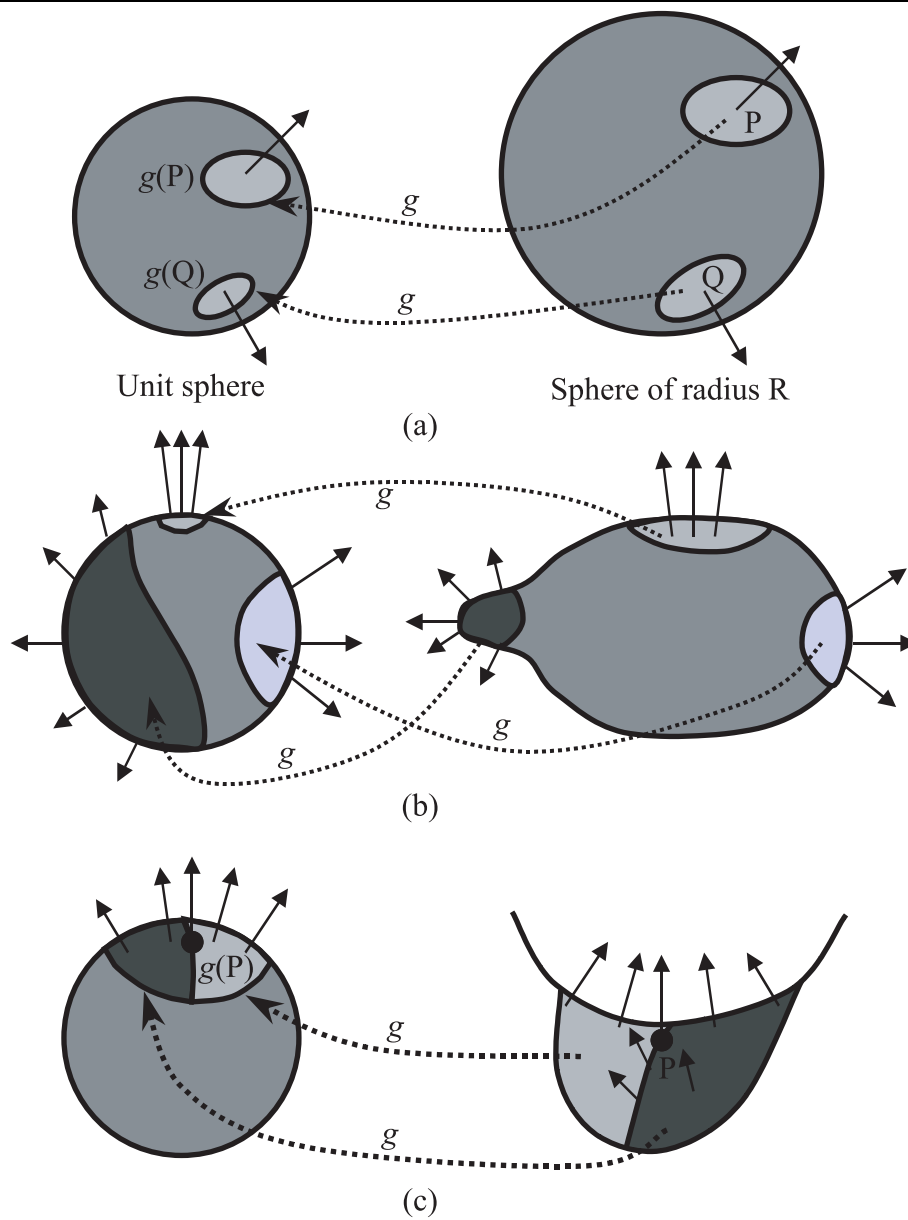


Figure B.2: Three examples of Gaussian mapping.

---

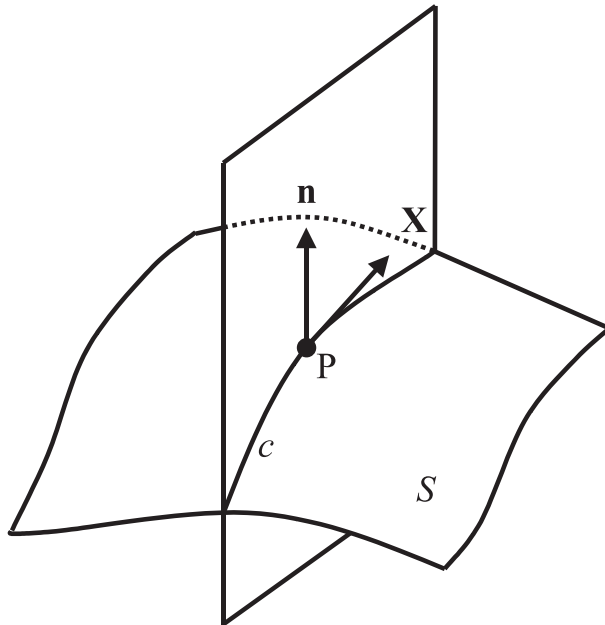


Figure B.3: Normal section.

the right and the left part around  $g(P)$ . The small area around  $P$  reversely maps to the small area around  $g(P)$ . You will see that hyperbolic surface reversely maps onto the unit sphere by Gaussian mapping.

## B.2 Gaussian Curvature

I consider that the cross section of the surface  $S$  with the plane consists of the unit normal vector  $\mathbf{n}$  and the arbitrary unit tangent vector  $\mathbf{X}$  at the point  $P$ . I call this plane the normal section, and I denote the curve generated by the cross section of the surface and the normal section as  $c$ . I represent the curvature of  $c$  as  $\kappa_{\mathbf{X}}$  (Figure B.3).

### Euler's theorem

Suppose  $\kappa_{\mathbf{X}}$  is not a constant value through the arbitrary unit tangent vector  $\mathbf{X}$  at  $P$  on  $S$ . There exist two unit tangent vectors  $\mathbf{X}_1$  and  $\mathbf{X}_2$  which have the following properties:

1.  $\kappa_{\mathbf{X}_1}$  is the maximum of  $\kappa_{\mathbf{X}}$ ,  $\kappa_{\mathbf{X}_2}$  is the minimum of  $\kappa_{\mathbf{X}}$
2.  $\mathbf{X}_1$  and  $\mathbf{X}_2$  are orthogonal.

3. When the angle between  $\mathbf{X}$  and  $\mathbf{X}_1$  is represented as  $\psi$ ,

$$\kappa_{\mathbf{X}} = \kappa_{\mathbf{X}_1} \cos^2 \psi + \kappa_{\mathbf{X}_2} \sin^2 \psi$$

### Definition of principal curvatures

$\kappa_{\mathbf{X}_1}$  and  $\kappa_{\mathbf{X}_2}$  are called principal curvatures at the point P, and  $\mathbf{X}_1$  and  $\mathbf{X}_2$  are called principal directions. The plane which consists of  $\mathbf{n}$  and  $\mathbf{X}_1$  and the plane which consists of  $\mathbf{n}$  and  $\mathbf{X}_2$ , are called principal planes. If  $\kappa_{\mathbf{X}_1} = \kappa_{\mathbf{X}_2} = \kappa_{\mathbf{X}}$ , the point is called umbilic.

### Definition of Gaussian curvature and mean curvature

$K = \kappa_{\mathbf{X}_1} \kappa_{\mathbf{X}_2}$  is called Gaussian curvature at the point P. If P is umbilic ( $\kappa_{\mathbf{X}_1} = \kappa_{\mathbf{X}_2} = k$ ), then  $K = k^2$ .  $H = \frac{1}{2}(\kappa_{\mathbf{X}_1} + \kappa_{\mathbf{X}_2})$  is called mean curvature.

In the following section, I will briefly describe  $\kappa_{\mathbf{X}_1}$  as  $\kappa_1$  and  $\kappa_{\mathbf{X}_2}$  as  $\kappa_2$ .

## B.3 Surface Classes

Suppose that I am classifying the surface by Gaussian curvature (Figure B.4).

I name each class of surface in Figure B.4 for convenience. From up to down, left to right; elliptic patch, hyperbolic patch, planar patch, cylindrical patch, toric patch, monkeysaddle-shaped patch, slide-shaped patch, and bell-shaped patch.  $K > 0$  at elliptic patch,  $K < 0$  at hyperbolic patch,  $K = 0$  at the other patches. I argue the curvatures only at the dotted curve of the toric patch, the slide-shaped patch and the bell-shaped patch, and at the center dot of the monkeysaddle-shaped patch.

The toric patch is shaped like a doughnut, and the Gaussian curvature at the dotted curve is zero. In this figure, the Gaussian curvature of the left part of the dotted curve is positive and that of the right part is negative. The monkeysaddle-shaped patch is shaped like a horse's saddle, but has an additional concave spot to accommodate the monkey's tail. In this figure, the Gaussian curvature at the center dot in the monkeysaddle-shaped patch is zero. The slide-shaped patch is shaped like a children's slide, and the Gaussian curvature is zero at any place. In particular, the dotted line denotes the umbilic point and the principal curvatures are zero. The slide-shaped patch consists of two cylindrical patches stuck at the dotted line. The bell-shaped patch is shaped like a part of a bell, and the Gaussian curvature of the dotted curve is zero. In this figure, the Gaussian curvature of the upper part of the dotted curve is negative and that of the lower part is positive.

Surfaces can be classified in three types,  $K > 0$ ,  $K < 0$  and  $K = 0$ , but I consider the more detailed classification of each surfaces in Figure B.4 by the sign of  $\kappa_1, \kappa_2$  ( $\kappa_1 > \kappa_2$ ). The Gaussian curvature  $K$ , mean curvature  $H$ , and principal curvatures  $\kappa_1$  and  $\kappa_2$  of each

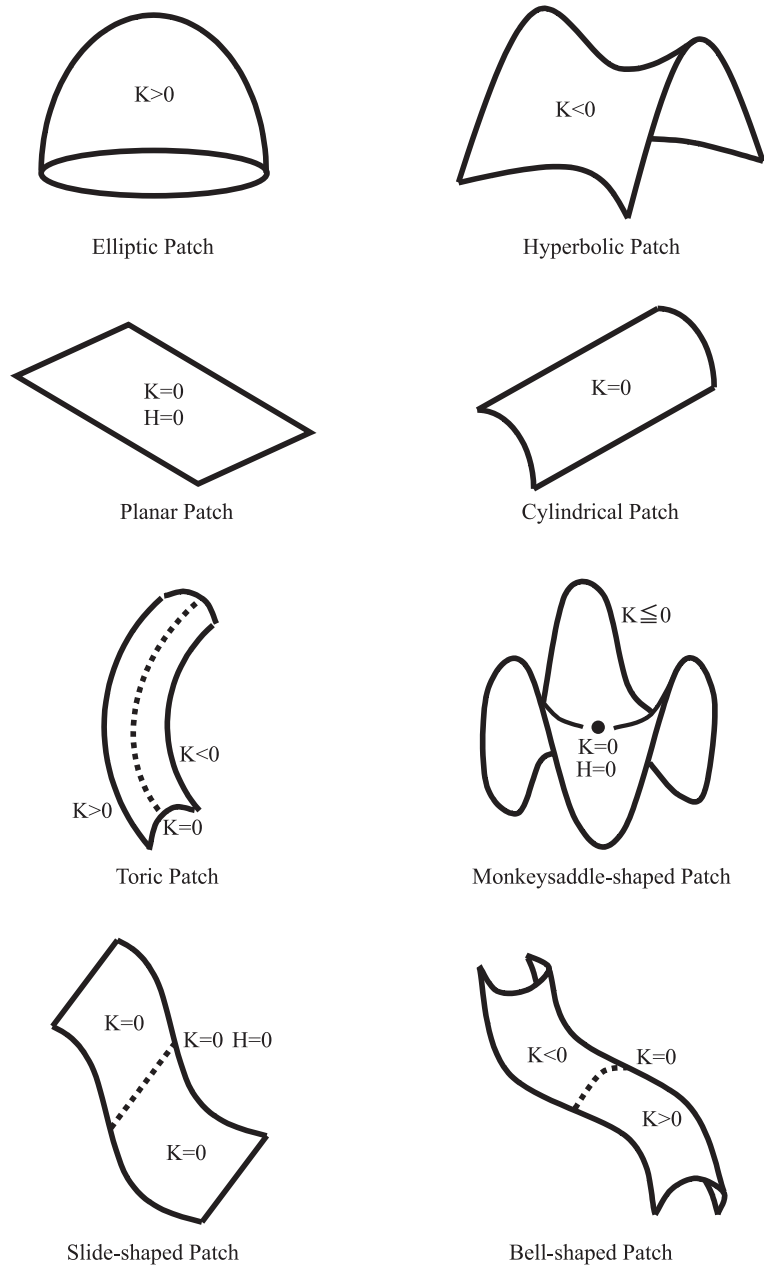


Figure B.4: Surfaces classified by Gaussian curvature.

---

Surface classes	Possible combinations of curvatures		
Elliptic patch	$K > 0, H > 0,$ $\kappa_1 > 0, \kappa_2 > 0$	$K > 0, H < 0,$ $\kappa_1 < 0, \kappa_2 < 0$	
Hyperbolic patch	$K < 0, H < 0,$ $\kappa_1 > 0, \kappa_2 < 0$	$K < 0, H = 0,$ $\kappa_1 > 0, \kappa_2 < 0$	$K < 0, H > 0,$ $\kappa_1 > 0, \kappa_2 < 0$
Planar patch	$K = 0, H = 0,$ $\kappa_1 = 0, \kappa_2 = 0$		
Cylindrical patch	$K = 0, H > 0,$ $\kappa_1 > 0, \kappa_2 = 0$	$K = 0, H < 0,$ $\kappa_1 = 0, \kappa_2 < 0$	
Toric patch	$K = 0, H > 0,$ $\kappa_1 > 0, \kappa_2 = 0$	$K = 0, H < 0,$ $\kappa_1 = 0, \kappa_2 < 0$	
Monkeysaddle-shaped patch	$K = 0, H = 0,$ $\kappa_1 = 0, \kappa_2 = 0$		
Slide-shaped patch	$K = 0, H = 0,$ $\kappa_1 = 0, \kappa_2 = 0$		
Bell-shaped patch	$K = 0, H > 0,$ $\kappa_1 > 0, \kappa_2 = 0$	$K = 0, H < 0,$ $\kappa_1 = 0, \kappa_2 < 0$	

Table B.1: Surface classes and curvatures

surfaces in Figure B.4 are shown in Table B.1. Note that the curvatures of the toric patch, the slide-shaped patch and the bell-shaped patch described in this table are the curvatures at the dotted curve of those patches, and the curvatures of the monkeysaddle-shaped patch are the curvatures at the center dot.

## B.4 Folding Point

Figure B.5 represents an example of the Gaussian mapping to the Gaussian sphere from the planar patch, the cylindrical patch, the toric patch, the monkeysaddle-shaped patch, the slide-shaped patch, and the bell-shaped patch.

The planar patch is mapped onto a point on the Gaussian sphere, and the cylindrical patch is mapped onto a curve on the Gaussian sphere. The toric patch is mapped onto an image which is point symmetry to a certain point. The surface points where  $K = 0$  is mapped onto that point on the Gaussian sphere. The monkeysaddle-shaped patch has a surface point where  $K = 0$  and  $H = 0$ , which is denoted in the figure as the dot in the center of the patch. The slide-shaped patch also has surface points where  $K = 0$  and  $H = 0$ , which are denoted in

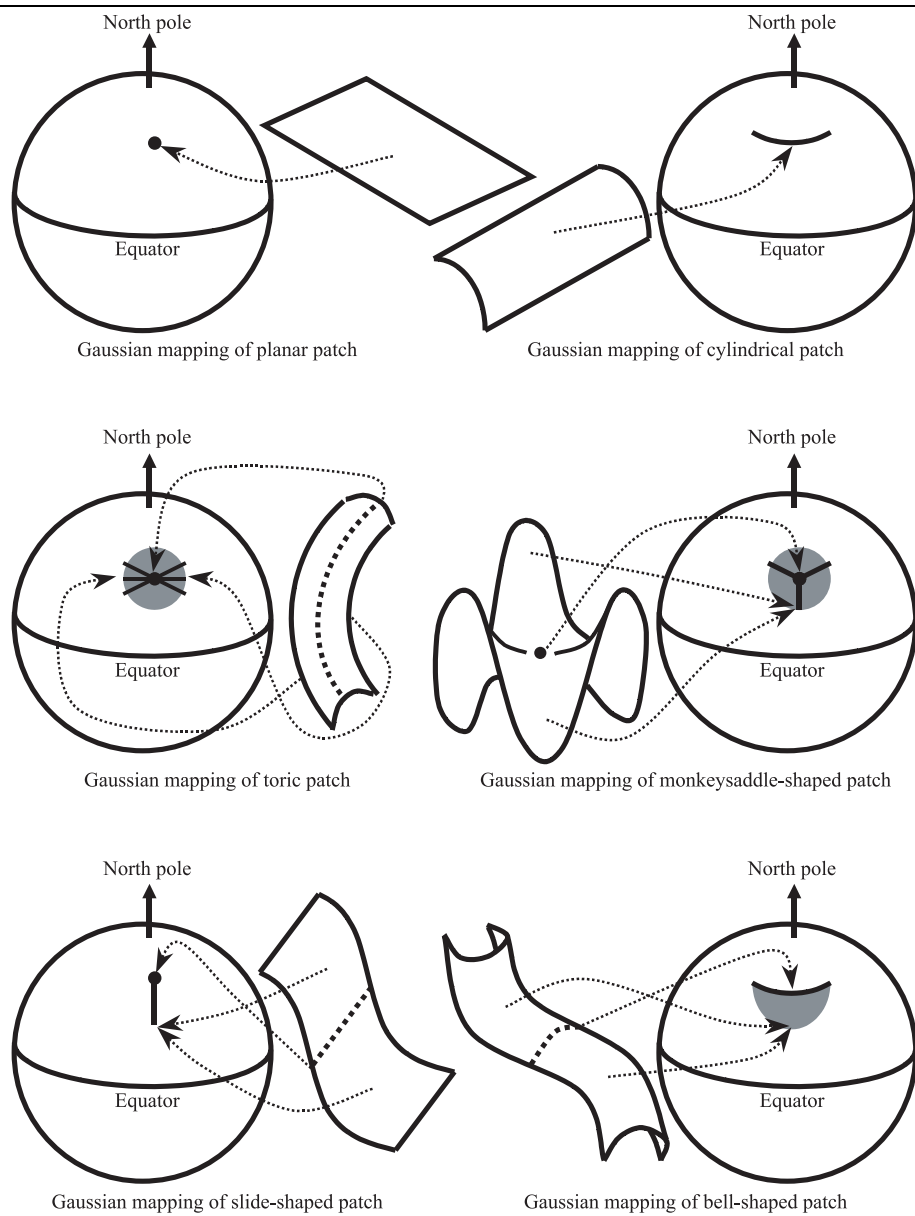


Figure B.5: Gaussian mapping of some patches.

the figure as a dotted line. The bell-shaped patch has surface points where  $K = 0$ , which are denoted in the figure as a dotted curve.

The term “local folding curve” is defined in Section 4.4.

For the bell-shaped patch in this figure, the upper surface where  $K < 0$  and the lower surface where  $K > 0$  are mapped onto the southern part from the folding curve, where  $K = 0$ . If the point walks from the point where  $K > 0$  to the point where  $K < 0$ , the point walks on the Gaussian sphere first from south to north, and then arrives at the folding curve when  $K = 0$ ; the point then turns in the opposite direction, and walks from north to south.

Two lines appear in the principal directions for a planar patch. A convex curve and a line appear in the principal directions for a cylindrical patch. A convex curve and a line appear in the principal directions at the point where  $K = 0$  for a toric patch. Either a line and an inflection point, or two inflection points, or two lines appear in the principal directions at the point where  $K = 0$  and  $H = 0$  for a monkeysaddle-shaped patch. A line and an inflection point or two inflection points appear in the principal directions at the point where  $K = 0$  and  $H = 0$  for a slide-shaped patch. A convex curve and an inflection point appear in the principal directions at the point where  $K = 0$  for a bell-shaped patch.

## APPENDIX C

# GEOMETRICAL PROPERTIES IN BREWSTER SEGMENTATION

In this appendix, I will examine the geometrical property of Brewster segmentation (Section 4.3) in detail.

### C.1 Local and Global Folding Curve

The B-B region on a Gaussian sphere is always enclosed by a Brewster curve and other additional curves. We define such a curve, which is not a Brewster curve, as a “global folding curve” or briefly a “folding curve”.

Consider mapping a local part of a surface onto a Gaussian sphere; if points of the surface map only onto one side of a curve on the Gaussian sphere and do not map onto the other side of such curve, we define such curve as a “local folding curve” or briefly a “folding curve”. A global folding curve is also a local folding curve. Figure C.1 illustrates the Gaussian mapping of a part of a bell-shaped surface having a local folding curve.

“Brewster curve on Gaussian sphere” is an image mapped from “Brewster curve on object surface”, and “folding curve on Gaussian sphere” is an image mapped from “folding curve on object surface”. If there is no confusion, we briefly write both “Brewster curve on object surface” and “Brewster curve on Gaussian sphere” as “Brewster curve”, and both “folding curve on object surface” and “folding curve on Gaussian sphere” as “folding curve”.

### C.2 B-N Region

**Theorem** *If a region is enclosed only by one Brewster curve on an object’s surface, and the Brewster curve on a Gaussian sphere covers all the points of a circle on a Gaussian sphere,*

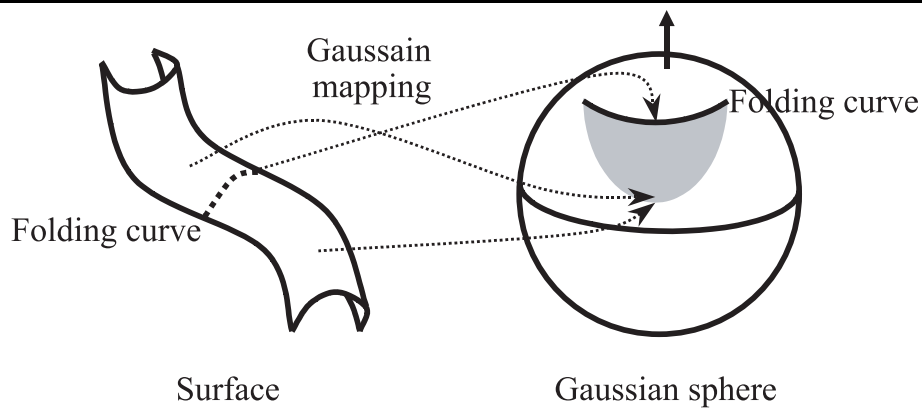


Figure C.1: Gaussian mapping of bell-shaped surface.

the region includes a point where  $\theta = 0$ .

**Proof.** A region on an object's surface enclosed by only one Brewster curve is homeomorphic (continuous, one-to-one, onto, and having a continuous inverse) to a disc. Assume the region on a Gaussian sphere mapped from such a region does not include a north pole. There is at least one hole in such a region  $R$ , hence  $\chi(R) \leq 0$ , where  $\chi(R)$  is the Euler number of  $R$ . On the other hand, the Euler number of a disc is 1. There is no continuous mapping between regions of different Euler numbers; thus, the assumption contradicts the existence of Gaussian mapping.  $\square$

The proof of theorem also proves that such a region covers the whole area of  $0 \leq \theta \leq \theta_B$ , and a region that covers the whole area of  $0 \leq \theta \leq \theta_B$  is always enclosed by only one Brewster curve.

**Theorem** *If a region enclosed only by Brewster curves on an object's surface does not include any global folding curves, the region includes a point where  $\theta = 0$ .*

**Proof.** Assume the region mapped onto the Gaussian sphere does not cover the whole area of  $0 \leq \theta \leq \theta_B$ ; thus, the region on the Gaussian sphere is enclosed both by Brewster curves and by at least one global folding curve. This assumption is contradictory to the condition where the region does not include any global folding curves. Therefore, the region on the Gaussian sphere covers the whole area of  $0 \leq \theta \leq \theta_B$ .

The proof implies that the region on the Gaussian sphere may possibly cover the whole area of  $\theta_B \leq \theta \leq 90^\circ$ ; however, the theorem does not allow the region to be enclosed by any

occluding boundaries (but allows the region to be enclosed only by Brewster curves); thus, the region is not a B-E region but a B-N region.  $\square$

Theorem holds not only for a global folding curve but also for a local folding curve, since if there are no local folding curves in the region, then also there are no global folding curves in the region.

From theorem , we can also adopt a definition of a B-B region and a B-N region as follows: a B-B region is a region that has global folding curves and a B-N region is a region that does not have any global folding curves. However, we adopt the definition described in Section 4.3 for simplicity.

### C.3 Integral Curvature

Section C.3.1 and Section C.3.2 explain the integral curvature of a B-B region and the northern hemisphere of a Gaussian sphere, respectively. We will list some of the information needed in these sections (see [Car76] for details):

1. If a vector  $\mathbf{a}$  and a vector  $\mathbf{b}$  are orthogonal(perpendicular), namely  $\mathbf{a} \cdot \mathbf{b} = 0$ , we represent as  $\mathbf{a} \perp \mathbf{b}$ , and if  $\mathbf{a}$  and  $\mathbf{b}$  is parallel, namely  $\mathbf{a} = w\mathbf{b}$  where  $w$  is a non-zero scalar, we represent as  $\mathbf{a} // \mathbf{b}$ .
2. We denote a curve as  $\mathbf{p}(s)$ , the unit tangent(velocity) vector of  $\mathbf{p}$  as  $\mathbf{r} = \mathbf{p}'$ , and the acceleration vector of  $\mathbf{p}$  as  $\mathbf{k} = \mathbf{r}' = \mathbf{p}''$ , where  $s$  represents the arc length. We use the notation, a curvature vector, instead of an acceleration vector in this paper.
3. We denote a geodesic curvature vector as  $\mathbf{k}_g$  and a geodesic curvature as  $\kappa_g = |\mathbf{k}_g|$ . We denote a normal curvature vector as  $\mathbf{k}_n$ .
4.  $\mathbf{r}$  and  $\mathbf{k}_g$  are tangent to the surface.  $\mathbf{k}_n$  is orthogonal to the surface.  $\mathbf{r} \perp \mathbf{k}_g$ ,  $\mathbf{r} \perp \mathbf{k}_n$ ,  $\mathbf{k}_g \perp \mathbf{k}_n$ , and  $\mathbf{k} = \mathbf{k}_n + \mathbf{k}_g$ .
5. If all points on a curve satisfy  $\mathbf{k}_g = 0$ , then such curve is called geodesic.
6. A level curve is defined in [Rah00]. This curve is a smooth closed curve that has an equal depth at all points on this curve. A level curve is not defined for  $\theta = 0$ .

**Theorem (Global Gauss-Bonnet theorem)**

$$\sum_{i=1}^n \int_{C_i} \kappa_g(s) ds + \iint_R K d\sigma + \sum_{l=1}^p \alpha_l = 2\pi\chi(R) \quad (\text{C.1})$$

holds, where  $R$  is a region and  $C_1, \dots, C_n$  are closed curves which is a component of the boundary of  $R$ .

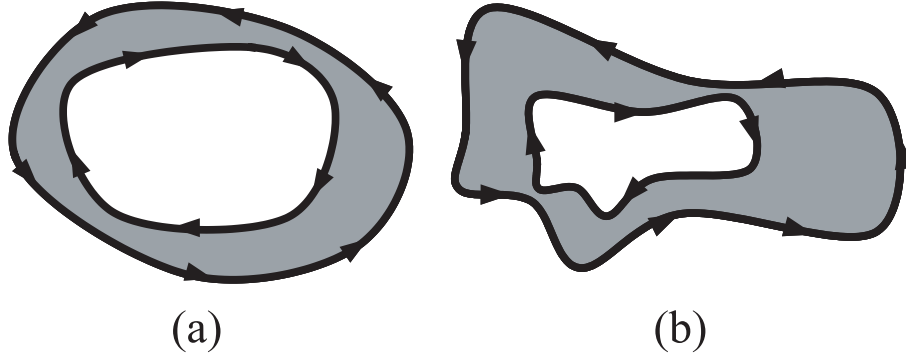


Figure C.2: The integration of the outer curve calculated in a counterclockwise trajectory, and the integral of the inner curve calculated in a clockwise trajectory: (a) a B-B region enclosed by two Brewster curves that are also ovals and level curves; (b) a B-B region enclosed by two Brewster curves that are also level curves and are in similarity.

$\iint K d\sigma$  is called an integral curvature. We use the notation, an integral geodesic curvature, for  $\int \kappa_g ds$  in this paper. In the following argument, we only deal with a smooth Brewster curve, thus,  $\sum \alpha_l = 0$ .

### C.3.1 B-B Region

If a level curve satisfies  $\theta = C$  in every point where  $C$  is constant and not 0, we call the curve a theta-depth constant curve. An image on a Gaussian sphere mapped from a theta-depth constant curve covers the whole points of a circle of  $\theta = C$  on a Gaussian sphere.

Suppose a B-B region on an object's surface is enclosed by two Brewster curves. We denote the two Brewster curves as  $\mathbf{p}(t)$  and  $\bar{\mathbf{p}}(\bar{t})$ , and denote those tangent vectors as  $\mathbf{r}(t)$  and  $\bar{\mathbf{r}}(\bar{t})$ , respectively. Take the domain of  $t$  and  $\bar{t}$  to be the same, and take  $\mathbf{R}$ ,  $t$  and  $\bar{t}$  to satisfy  $\bar{\mathbf{r}}(\bar{t}) = \mathbf{R}\mathbf{r}(t)$  for  $t = \bar{t}$  where  $\mathbf{R}$  is a  $t$ -independent rotation matrix whose rotation axis equals to the viewing direction. If two Brewster curves have above condition, we say those two Brewster curves are in tangent-correspondence.

Examples of such two Brewster curves are;

1. Two Brewster curves that are ovals (= convex closed curves) and level curves (figure C.2(a)).
2. Two Brewster curves that are level curves and in similarity (figure C.2(b)).

**Theorem** When a B-B region on an object's surface is enclosed by two Brewster curves, and both Brewster curves are level curves, and those two Brewster curves are in tangent-correspondence, the integral curvature of the B-B region will be 0.

**Proof.** Now briefly write  $\mathbf{R}\mathbf{r}$  as  $\mathbf{r}$ , thus,  $\mathbf{r}(t) = \bar{\mathbf{r}}(\bar{t})$ . We denote the curvature vector of  $\mathbf{p}(t)$  and  $\bar{\mathbf{p}}(\bar{t})$  as  $\mathbf{k}(t)$  and  $\bar{\mathbf{k}}(\bar{t})$ , respectively:  $\mathbf{r} \perp \mathbf{k}$  and  $\mathbf{r} \perp \bar{\mathbf{k}}$ . Since  $\mathbf{r}(t) = \bar{\mathbf{r}}(\bar{t})$ , we obtain  $\mathbf{k}(t)(dt/ds) = \bar{\mathbf{k}}(\bar{t})(d\bar{t}/ds)$ . Level curve is orthogonal to the viewing direction, thus,  $\mathbf{v} \perp \mathbf{r}$ ,  $\mathbf{v} \perp \bar{\mathbf{r}}$ ,  $\mathbf{v} \perp \mathbf{k}$ , and  $\mathbf{v} \perp \bar{\mathbf{k}}$ , where  $\mathbf{v}$  represent the viewing direction. Denote the normal curvature vector of  $\mathbf{p}(t)$  and  $\bar{\mathbf{p}}(\bar{t})$  as  $\mathbf{k}_n(t)$  and  $\bar{\mathbf{k}}_n(\bar{t})$ , respectively:  $\mathbf{r} \perp \mathbf{k}_n$  and  $\mathbf{r} \perp \bar{\mathbf{k}}_n$ . The angle between  $\mathbf{k}_n$  and  $\mathbf{v}$  is  $\theta_B$ :

$$\mathbf{v} \cdot \mathbf{k}_n = |\mathbf{v}||\mathbf{k}_n| \cos \theta_B, \quad (\text{C.2})$$

$$\mathbf{v} \cdot \bar{\mathbf{k}}_n = |\mathbf{v}||\bar{\mathbf{k}}_n| \cos \theta_B. \quad (\text{C.3})$$

As a result,  $\mathbf{k}_n$  and  $\bar{\mathbf{k}}_n$  is included in the plane consisted of  $\mathbf{k}$  and  $\mathbf{v}$  (figure C.3). Denote the geodesic curvature vector of  $\mathbf{p}(t)$  and  $\bar{\mathbf{p}}(\bar{t})$  as  $\mathbf{k}_g(t)$  and  $\bar{\mathbf{k}}_g(\bar{t})$ , respectively.  $\mathbf{k}(t)(dt/ds) = \bar{\mathbf{k}}(\bar{t})(d\bar{t}/ds)$  and  $\mathbf{k}_n/\bar{\mathbf{k}}_n$  have been derived, and from  $\bar{\mathbf{k}} = \bar{\mathbf{k}}_n + \bar{\mathbf{k}}_g$  and  $\bar{\mathbf{k}}_n \perp \bar{\mathbf{k}}_g$ , we derive  $\mathbf{k}_n(t)(dt/ds) = \bar{\mathbf{k}}_n(\bar{t})(d\bar{t}/ds)$  and  $\mathbf{k}_g(t)(dt/ds) = \bar{\mathbf{k}}_g(\bar{t})(d\bar{t}/ds)$ . Therefore;

$$\left| \int \kappa_g(t) \frac{dt}{ds} ds \right| = \left| \int \bar{\kappa}_g(\bar{t}) \frac{d\bar{t}}{ds} ds \right|. \quad (\text{C.4})$$

Sign of  $\int \kappa_g dt$  and  $\int \bar{\kappa}_g d\bar{t}$  is opposite (Figure C.2), namely  $\sum \int \kappa_g(s) ds = \int \kappa_g dt + \int \bar{\kappa}_g d\bar{t} = 0$ . Therefore, from Gauss-Bonett theorem, we can conclude that the integral curvature of this B-B region is 0.  $\square$

If an arc length of a curve becomes  $w$  times longer, a curvature becomes  $w$  times smaller, thus, the integral of the curve does not change before and after the scaling. Note that in most cases  $\mathbf{k}(s) \neq \bar{\mathbf{k}}(s)$ , even if  $\mathbf{k}(t) = \bar{\mathbf{k}}(\bar{t})$  and  $s$  represents the arc length corresponding to this  $t$  and  $\bar{t}$ .

If  $\mathbf{R}$  depends on  $t$ , namely  $\mathbf{R}(t)$ , the integral curvature of a B-B region enclosed by two Brewster curves that are also level curves will not always be 0.  $\mathbf{R}(t)$  can be defined as;

$$\mathbf{R}(t) = \begin{pmatrix} \cos \psi(t) & -\sin \psi(t) \\ \sin \psi(t) & \cos \psi(t) \end{pmatrix}, \quad (\text{C.5})$$

then  $d\mathbf{R}(t)/dt$  will be;

$$\begin{aligned} \frac{d\mathbf{R}(t)}{dt} &= \begin{pmatrix} -\sin \psi(t) & -\cos \psi(t) \\ \cos \psi(t) & -\sin \psi(t) \end{pmatrix} \frac{d\psi(t)}{dt} \\ &= \begin{pmatrix} \cos(\psi(t) + 90^\circ) & -\sin(\psi(t) + 90^\circ) \\ \sin(\psi(t) + 90^\circ) & \cos(\psi(t) + 90^\circ) \end{pmatrix} \frac{d\psi(t)}{dt}. \end{aligned} \quad (\text{C.6})$$

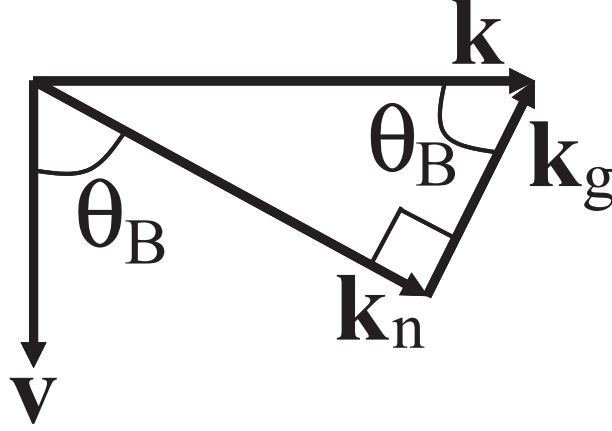


Figure C.3: Viewing vector  $\mathbf{v}$ , curvature(acceleration) vector  $\mathbf{k}$ , normal curvature vector  $\mathbf{k}_n$ , geodesic curvature vector  $\mathbf{k}_g$ , and Brewster angle  $\theta_B$ .

Differentiate  $\bar{\mathbf{r}}(\bar{t}) = \mathbf{R}(t)\mathbf{r}(t)$ , and obtain;

$$\bar{\mathbf{k}}(\bar{t}) \frac{d\bar{t}}{ds} = \frac{d\mathbf{R}(t)}{dt} \frac{dt}{ds} \mathbf{r}(t) + \mathbf{R}(t)\mathbf{k}(t) \frac{dt}{ds}. \quad (\text{C.7})$$

From  $\bar{\mathbf{r}} \perp \bar{\mathbf{k}}$ ;

$$\bar{\mathbf{k}}(\bar{t}) \frac{d\bar{t}}{ds} = (1 + w(t) \frac{d\psi}{dt}) \mathbf{R}(t)\mathbf{k}(t) \frac{dt}{ds}, \quad (\text{C.8})$$

where  $w(t)$  is a  $t$ -dependent scalar. If  $\mathbf{R}$  is constant, then  $d\psi/dt = 0$ , which is the case described in the above theorem .

### C.3.2 Northern Hemisphere

**Theorem** *If each occluding boundary is a level curve, the integral curvature of the region corresponding to the northern hemisphere of the Gaussian sphere will be  $2\pi\chi$ .*

**Proof.** A level curve is included in the plane orthogonal to the viewing direction, thus,  $\mathbf{k}$  will be included in that plane.  $\mathbf{k}_n$  is also orthogonal to the viewing direction for occluding boundaries. From  $\mathbf{r} \perp \mathbf{k}$  and  $\mathbf{r} \perp \mathbf{k}_n$ , we derive  $\mathbf{k} \parallel \mathbf{k}_n$ . From  $\mathbf{k} = \mathbf{k}_n + \mathbf{k}_g$  and  $\mathbf{k}_n \perp \mathbf{k}_g$ , we derive  $\mathbf{k} = \mathbf{k}_n$  and  $\mathbf{k}_g = 0$ . As a result, the occluding boundary will be a closed geodesic, and the integral geodesic curvature will be 0; thus, the integral curvature will be  $2\pi\chi$  from Gauss-Bonnet theorem .  $\square$

By calculating the integral curvature of a region, we can argue the measurement error of the proposed method, however, we did not calculate it, since theorem and can only be

applied to a limited case. Section C.3.1 and C.3.2 showed that the regions have an interesting property from an aspect of differential geometry; thus, we expect that our region segmentation method is appropriate to analyze the geometrical property of the object surface and potentially has a more important property of the regions.

## APPENDIX D

# ENGLISH-JAPANESE DICTIONARY OF TECHNICAL TERMS

absorbe	吸収する
absorptance	吸収率
acceleration vector	加速度ベクトル
acoustics	音響学
acrylic	アクリル
affine transformation	アフィン変換
alpha blending	アルファブレンディング
alpha estimation	アルファ推定
alternating-direction implicit method	交互方向陰的解法, ADI法
ambient light	環境光
ambiguity	曖昧性
amplitude	振幅
angular frequency	角周波数
anisotropic	異方性の
apical angle	頂角
arc length	弧長
autocollimation	オートコリメーション
azimuth angle	方位角

background radiation	背景放射
base angle	底角
B-B region (coined word)	B-B領域(造語)
B-E region (coined word)	B-E領域(造語)
bidirectional reflectance distribution function	双方向反射分布関数, BRDF
binocular stereo	二眼ステレオ
birefringent	複屈折性の
blackbody	黒体
B-N region (coined word)	B-N領域(造語)
body reflection	内部反射, ⇒diffuse reflection
Boltzmann constant	ボルツマン定数
BRDF	⇒bidirectional reflectance distribution function
Brent's method	ブレントの方法
Brewster angle	ブリュースタ角
Brewster curve (coined word)	ブリュースタ線(造語)
Brewster point (coined word)	ブリュースタ点(造語)
Brewster segmentation (coined word)	ブリュースタ分割(造語)
B-spline curve	Bスプライン曲線

charge density	電荷密度
Chebyshev approximation	チェビシェフ近似
circular polarization	円偏光
coagulation	凝固
coefficient	係数
coherence matrix	コヒーレンス行列
concave	凹
constraint	制約
coordinates	座標系
conservation	保存
convex	凸
corresponding point	対応点
critical angle	臨界角
crossing over	交叉
cross over	⇒crossing over
cross section	切断面
curvature vector	曲率ベクトル

degenerate	縮退する
degree of polarization	偏光度
DIC	⇒Nomarski differential interference contrast microscope
dielectric	誘電体
dielectric permittivity	誘電率
differential geometry	微分幾何学
diffuser	拡散板
diffuse reflection	拡散反射, ⇒body reflection
dimple	えくぼ
disambiguate	曖昧性を除去する
disc	円盤
DOP	⇒degree of polarization
dot product	内積

electric current density	電流密度
electric displacement	電束密度
electric field	電場
electric vector	電気ベクトル
electrolytic polarization	分極
electromagnetic	電磁の
electromagnetic wave	電磁波
elliptic	楕円の
emissivity	透過率
emitted	放射した
emitting angle	放射角
envrionment matting	環境マッティング
EPI	⇒epipolar plane image
epipolar plane image	エピポーラ平面画像, エピ極平面画像, EPI
epoxy	エポキシ樹脂
Euler equation	オイラー方程式
Euler-Lagrange differential equation	⇒Euler equation
extended light source	拡張光源
external interreflection (coined word)	外部相互反射(造語), ⇒internal interreflection
extremum	極値

folding point (coined word)	折り返し点(造語)
folding curve (coined word)	折り返し線(造語)
Fourier analysis	フーリエ解析
4-neighbor average	4近傍平均
frequency	周波数
Fresnel formula	フレネル関数
frontal surface (coined word)	正面形状(造語)
frosted glass	すりガラス

Gaussian curvature	ガウス曲率
Gaussian mapping	ガウス写像
Gaussian sphere	ガウス球
genetic algorithm	遺伝的アルゴリズム
geodesation	測地化
geodesic	測地線
geodesic curvature vector	測地的曲率ベクトル
geodesic dome	測地ドーム, ジオデジックドーム
geometrical calibration	幾何的校正
geometry	幾何, 幾何学
global folding curve (coined word)	大域的折り返し線(造語)
gradient	勾配
great circle	大円

haptic	触覚の
Hessian	ヘッセ行列
hexagon	六角形
hollow	中空の
homeomorphic	位相同形
hue	色相
hyperbolic	双曲の

ICA	⇒independent component analysis
icosahedron	二十面体
imaginary number	虚数
incandescent lamp	白熱電球
incident angle	入射角
incident light	入射光
independent component analysis	独立成分分析
infinitesimal	微小
inflection point	変曲点
infrared light	赤外光
ingredient	成分, 原料
insulator	絶縁体
integral curvature	総曲率
integral geodesic curvature (coined word)	総測地的曲率(造語)
intensity	強度
interface	界面, 境界面
interferometry	干渉法
internal reflection	内部反射, ⇒internal interreflection
internal interreflection (coined word)	内部相互反射(造語), ⇒internal reflection, interreflection
interreflection	相互反射, ⇒internal interreflection
isosceles triangle	二等辺三角形
isotropic	等方性の
iteration	反復

Jacobi method	ヤコビ法
Jones calculus	ジョーンズ計算法

Lagrange undetermined multiplier	ラグランジュの未定乗数
laser range sensor	レーザーレンジセンサー
least square method	最小二乗法
level curve	レベル曲線
linear polarizer	直線偏光板
liquid crystal	液晶
local folding curve (coined word)	局所的折り返し線(造語)

magnetic field	磁場
magnetic induction	磁気誘導
magnetic permeability	透磁率
magnetic vector	磁気ベクトル
magnetization	磁化
matting	マッティング
mean curvature	平均曲率
mean deviation	平均偏差
median filtering	メディアンフィルタリング
medium	媒質
moiré topography	モアレトポグラフィ
Mueller calculus	ミュラー計算法
Mueller matrix	ミュラー行列
mutation	突然変異

natural selection	自然淘汰, 自然選択
Nomarski differential interference contrast microscope	ノマルスキー微分干渉顕微鏡
normal curvature vector	法曲率ベクトル
normal section	法断面, 法断面

oblique	斜めの
occluding boundary	遮蔽境界, 遮蔽輪郭, 外縁線
opacity	不透明度
opaque	不透明な
optical flow	オプティカルフロー
optics	光学
orthogonal	直交の
oval	卵形線

parabolic	放物の
parallel	平行の
perpendicular	垂直の
phase	位相
phase shift	位相のずれ
photoelastic effect	光弾性効果
photometric stereo	照度差ステレオ
Planck constant	プランク定数
Planck radiation law	プランクの輻射式
plane of incidence	入射面
plane wave	平面波
PLZT	PLZT
POI	⇒plane of incidence
POI angle	入射面角度
polar coordinates	極座標系
polarization	偏光
polarization degree	⇒degree of polarization
polarization raytracing equation (coined word)	偏光レイトレーシング方程式(造語)
polarization raytracing method	偏光レイトレーシング法
polyhedron	多面体
polynomial	多項式
position vector	位置ベクトル
principal curvatures	主曲率
principal directions	主方向
principal planes	主平面
propagation vector	伝播ベクトル

radiate	放射する
raytracing method	レイトレーシング法, 光線追跡法, 視線探索法
rear surface (coined word)	背面形状(造語)
reflected light	反射光
reflecting angle	反射角
reflectivity	反射率
refractive index	屈折率
region growing method	領域拡張法
relaxation method	弛緩法, 緩和法
repulsive force	反発力
right circular polarization	右円偏光
RMS error	⇒root mean square error
root mean square error	RMS誤差, 平均二乗誤差, 二乗平均平方根誤差

scanning electron microscopy	走査型電子顕微鏡法
self-occlusion	自己遮蔽
SEM	⇒scanning electron microscopy
semicircle	半円
shape from silhouette	視体積交差法, 輪郭投影法, shape-from-silhouette, シルエット法
similarity	相似
sinusoidal function	サイン関数
small circle	小円
smoothing	スムージング, 平滑化
solid	固体
specular reflection	鏡面反射, ⇒surface reflection
spherical cap	球冠, 球面部分, 部分球
square pillar	四角柱
Stephan-Boltzmann constant	ステファン・ボルツマン定数
Stephan-Boltzmann law	ステファン・ボルツマンの法則
Stokes vector	ストークスベクトル
substitute	代入する
successive over-relaxation method	逐次過緩和法, SOR法
surface normal	表面法線
surface reflection	表面反射, ⇒specular reflection
system	システム, 機械装置, 系

tangent vector	接ベクトル
thermal equilibrium	熱平衡
thermal radiation	熱放射
thermodynamics	熱力学
theta-depth constant curve (coined word)	$\theta$ -デプス一定曲線(造語)
topology	トポロジー
toric	トーラスの
total reflection	全反射
trajectory	軌跡
translucent	半透明な
transmitted light	透過光
transmitting angle	透過角
transmissivity	透過率
transparent	透明な
transversal wave	横波
trapezoid	台形
trinocular	三眼の

ultrasonic waves	超音波
uniform	均一な
unit tangent vector	単位接ベクトル
unpolarized	非偏光の
umbilic	臍点

vacuum	真空
velocity vector	速度ベクトル
visible light	可視光
visual hull	⇒shape from silhouette

wavelength	波長
wavelet transformation	ウェーブレット変換
wave vector	波数ベクトル
zenith angle	天頂角

## BIBLIOGRAPHY

- [AM90] P. K. Allen and P. Michelman, "Acquisition and interpretation of 3-D sensor data from touch," *IEEE Transactions on Robotics and Automation*, vol. 6, no. 4, Aug. 1990.
- [BB82] D. H. Ballard and C.M. Brown, *Computer Vision*, p. 523, Englewood Cliffs, N.J.: Prentice Hall, 1982.
- [BN03] M. Ben-Ezra and S. K. Nayar, "What does motion reveal about transparency?," in *Proceedings of IEEE International Conference on Computer Vision*, pp. 1025–1032, Nice, France, Oct. 2003.
- [BN98] D. N. Bhat and S. K. Nayar, "Stereo and Specular Reflection," *International Journal of Computer Vision*, vol. 26, no. 2, pp. 91–106, 1998.
- [BW59] M. Born and E. Wolf, *Principles of optics*, Pergamon Press, London, 1959.
- [Car76] M. P. do Carmo, *Differential geometry of curves and surfaces*, Prentice-Hall, New Jersey, 1976.
- [CW98] H. Chen and L. B. Wolff, "Polarization phase-based method for material classification in computer vision," *International Journal of Computer Vision*, vol. 28, no. 1, pp. 73–83, 1998.
- [Chi95] R. A. Chipman, "Mechanics of polarizaiton ray tracing," *Optical Engineering*, vol. 34, no. 6, pp. 1636–1645, June 1995.
- [CZH+00] Y. Chuang, D. E. Zongker, J. Hindorff, B. Curless, D. H. Salesin, and R. Szeliski, "Environment matting extensions: towards higher accuracy and real-time capture," in *Proceedings of ACM SIGGRAPH 2000*, pp. 121–130, New Orleans, Louisiana USA, July 2000.
- [CTW97] J. Clark, E. Trucco, and L. B. Wolff, "Using light polarization in laser scanning," *Image and Vision Computing*, vol. 15, no. 2, pp. 107–117, Feb. 1997.

- [CH53] R. Courant and D. Hilbert, *Methods of mathematical physics*, Wiley, New York, 1953.
- [DHT+00] P. Debevec, T. Hawkins, C. Tchou, H.-P. Duiker, and W. Sarokin, “Acquiring the Reflectance Field of a Human Face,” in *Proceedings of ACM SIGGRAPH 2000*, pp. 145–156, New Orleans, Louisiana USA, July 2000.
- [DWT+02] P. Debevec, A. Wenger, C. Tchou, A. Gardner, J. Waese, and T. Hawkins, “A Lighting Reproduction Approach to Live-Action Compositing,” *ACM Transactions on Graphics (Proceedings of ACM SIGGRAPH 2002)*, vol. 21, no. 3, pp. 547–556, (San Antonio, Texas USA), July 2002.
- [DS01] O. Drbohlav and R. Šára, “Unambiguous determination of shape from photometric stereo with unknown light sources,” in *Proceedings of IEEE International Conference on Computer Vision*, pp. I:581–586, Vancouver, Canada, July 2001.
- [Exa] Exact Corporation, 3-1-15 Toyotama-minami, Nerima-ku, Tokyo 176-8502, Japan.
- [FA99] H. Farid and E. H. Adelson, “Separating reflections from images by use of independent component analysis,” *Journal of Optical Society of America, A*, vol. 16, no. 9, pp. 2136–2145, Sep. 1999.
- [FTA+98] H. Fujikake, K. Takizawa, T. Aida, H. Kikuchi, T. Fujii, and M. Kawakita, “Electrically-Controllable Liquid Crystal Polarizing Filter for Eliminating Reflected Light,” *Optical Review*, vol. 5, no. 2, pp. 93–98, 1998.
- [FKIS02] R. Furukawa, H. Kawasaki, K. Ikeuchi, and M. Sakauchi, “Appearance based object modeling using texture database: Acquisition compression and rendering,” in *Proceedings of the 13th Eurographics Workshop on Rendering*, June 2002.
- [Fur] Furuuchi Chemical Corporation, <http://www.furuchi.co.jp/>.
- [GW93] R. C. Gonzalez and R. E. Woods, *Digital Image Processing*, p. 716, Reading, Mass.: Addison Wesley, 1993.
- [GY93] C. Gu and P. Yeh, “Extended Jones matrix method. II,” *Journal of Optical Society of America, A*, vol. 10, no. 5, pp. 966–973, May 1993.
- [GS04] S. Guy and C. Soler, “Graphics Gems Revisited: Fast and Physically Based Rendering of Gemstones,” *ACM Transactions on Graphics (Proceedings of ACM SIGGRAPH 2004)*, vol. 23, no. 3, pp. 231–238, (Los Angeles, California USA), Aug. 2004.

- [HS01] Z. S. Hakura and J. M. Snyder, "Realistic reflections and refractions on graphics hardware with hybrid rendering and layered environment maps," in *Proceedings of Eurographics Workshop on Rendering*, pp. 289–300, London, United Kingdom, June 2001.
- [HNNI02] K. Hara, K. Nishino, A. Nakazawa, and K. Ikeuchi, "Estimating Light Position and Surface Reflectance from Specular Reflection under Perspective Projection," in *Proceedings of IAPR Workshop on Machine Vision Applications*, pp. 566–571, Nara, Japan, Dec. 2002.
- [HC02] C. K. Harnett and H. G. Craighead, "Liquid-crystal micropolarizer array for polarization-difference imaging," *Applied Optics*, vol. 41, no. 7, pp. 1291–1296, 2002.
- [Hat92] S. Hata, "Shape Detection of Small Specular Surface using Color Stripe Lighting," in *Proceedings of International Conference on Pattern Recognition*, pp. I:554–557, 1992.
- [HSKK96] S. Hata, Y. Saitoh, S. Kumamura, and K. Kaida, "Shape extraction of transparent object using genetic algorithm," in *Proceedings of International Conference on Pattern Recognition*, pp. 684–688, Vienna, Austria, Aug. 1996.
- [HCD01] T. Hawkins, J. Cohen, and P. Debevec, "A Photometric Approach to Digitizing Cultural Artifacts," in *Proceedings of 2nd International Symposium on Virtual Reality, Archaeology, and Cultural Heritage*, Glyfada, Greece, Nov. 2001.
- [Hec02] E. Hecht, *Optics*, Addison-Wesley, Reading, Mass., 2002.
- [Hor86] B. K. P. Horn, *Robot vision*, MIT Press, Cambridge, Mass., 1986.
- [Hor90] B. K. P. Horn, "Height and Gradient from Shading," *International Journal on Computer Vision*, vol. 5, no. 1, pp. 37–75, 1990.
- [IJ04] R. Ibrayev and Y.-B. Jia, "Tactile recognition of algebraic shapes using differential invariants," in *Proceedings of the IEEE International Conference on Robotics and Automation*, pp. 1548–1553, New Orleans, LA USA, Apr.–May 2004.
- [Ike81] K. Ikeuchi, "Determining Surface Orientations of Specular Surfaces by Using the Photometric Stereo Method," *IEEE Transactions on Pattern Analysis and Machine Intelligence*, vol. 3, no. 6, pp. 661–669, 1981.

- [Ike84] K. Ikeuchi, "Reconstructing a depth map from intensity maps," in *Proceedings of International Conference on Pattern Recognition*, pp. 736–738, Montreal, Canada, Aug. 1984.
- [IS01] K. Ikeuchi and Y. Sato, *Modeling from reality*, p. 199, Kluwer Academic Publishers, Dordrecht, The Netherlands, 2001.
- [JL94] D. L. Jordan and G. D. Lewis, "Measurements of the effect of surface roughness on the polarization state of thermally emitted radiation," *Optical Letters*, vol. 19, pp. 692–694, 1994.
- [JLJ96] D. L. Jordan, G. D. Lewis, and E. Jakeman, "Emission polarization of roughened glass and aluminum surfaces," *Applied Optics*, vol. 35, pp. 3583–3590, 1996.
- [KK98] F. Kagalwala and T. Kanade, "Computational model of image formation process in DIC microscopy," in *Proceedings of SPIE*, vol. 3261, pp. 193–204, San Jose, CA USA, Jan. 1998.
- [KI93] T. Kiuchi and K. Ikeuchi, "Roughness and shape of specular lobe surfaces using photometric sampling method," in *Proceedings of IEEE Conference of Computer Vision and Pattern Recognition*, pp. 765–766, New York, June 1993.
- [Koe90] J. J. Koenderink, *Solid Shape*, p. 699, The MIT Press, Cambridge, Massachusetts, 1990.
- [KS87] K. Koshikawa and Y. Shirai, "A model-based recognition of glossy objects using their polarimetric properties," *Advanced Robotics*, vol. 2, no. 2, pp. 137–147, 1987.
- [LZW04] A. Levin, A. Zomet, and T. Weiss, "Separating reflections from a single image using local features," in *Proceedings of IEEE Computer Society Conference on Computer Vision and Pattern Recognition*, pp. I:306–313, Washington, DC, USA, June–July 2004.
- [Lig] LightTools, <http://www.opticalres.com/>.
- [LL97] S. Lin and S. W. Lee, "Detection of Specularity Using Stereo in Color and Polarization Space," *Computer Vision and Image Understanding*, vol. 65, no. 2, pp. 336–346, Feb. 1997.
- [MTKO02] H. Matsuoka, T. Takeuchi, H. Kitazawa, and A. Onozawa, "Representation of pseudo inter-reflection and transparency by considering characteristics of human

- vision,” in *Proceedings of Eurographics*, pp. 503–510, Saarbrücken, Germany, Sep. 2002.
- [MPZ+02] W. Matusik, H. Pfister, R. Ziegler, A. Ngan, and L. McMillan, “Acquisition and rendering of transparent and refractive objects,” in *Proceedings of Eurographics Workshop on Rendering*, pp. 267–278, Pisa, Italy, June 2002.
- [MON+00] D. Miyazaki, T. Oishi, T. Nishikawa, R. Sagawa, K. Nishino, T. Tomomatsu, Y. Takase, and K. Ikeuchi, “The Great Buddha Project: Modeling Cultural Heritage through Observation,” in *Proceedings of International Conference on Virtual Systems and MultiMedia*, pp. 138–145, 2000.
- [MSSI02] D. Miyazaki, M. Saito, Y. Sato, and K. Ikeuchi, “Determining surface orientations of transparent objects based on polarization degrees in visible and infrared wavelengths,” *Journal of Optical Society of America, A*, vol. 19, no. 4, pp. 687–694, Apr. 2002.
- [MTHI03] D. Miyazaki, R. T. Tan, K. Hara, and K. Ikeuchi, “Polarization-based inverse rendering from a single view,” in *Proceedings of IEEE International Conference on Computer Vision*, pp. 982–987, Nice, France, Oct. 2003.
- [MKI04] D. Miyazaki, M. Kagesawa, and K. Ikeuchi, “Transparent surface modeling from a pair of polarization images,” *IEEE Transactions on Pattern Analysis and Machine Intelligence*, vol. 26, no. 1, pp. 73–82, Jan. 2004.
- [MI05] D. Miyazaki and K. Ikeuchi, “Inverse Polarization Ray-tracing: Estimating Surface Shape of Transparent Objects,” in *Proceedings of IEEE Computer Society International Conference on Computer Vision and Pattern Recognition*, San Diego, CA USA, June 2005.
- [Mur92] H. Murase, “Surface shape reconstruction of a nonrigid transparent object using refraction and motion,” *IEEE Transactions on Pattern Analysis and Machine Intelligence*, vol. 14, no. 10, pp. 1045–1052, Oct. 1992.
- [NWK88] K. Nakano, Y. Watanabe, and S. Kanno, “Extraction and recognition of 3-dimensional information by projecting a pair of slit-ray beams,” in *Proceedings of International Conference on Pattern Recognition*, pp. 736–738, Rome, Italy, Nov. 1988.
- [NSWS90] S. K. Nayar, A. C. Sanderson, L. E. Weiss, and D. A. Simon, “Specular Surface Inspection Using Structured Highlight and Gaussian Images,” *IEEE Transactions on Robotics and Automation*, vol. 6, no. 2, pp. 208–218, Apr. 1990.

- [NIK90] S. K. Nayar, K. Ikeuchi, and T. Kanade, "Determining Shape and Reflectance of Hybrid Surface by Photometric Sampling," *IEEE Transactions of Robotics and Automation*, vol. 6, no. 4, pp. 418–431, Aug. 1990.
- [Nay91] S. K. Nayar, "Shape Recovery using Physical Models of Reflection and Inter-reflection," *A Dissertation*, Carnegie Mellon University, May 1991.
- [NIK91a] S. K. Nayar, K. Ikeuchi, and T. Kanade, "Surface reflection: Physical and geometrical perspectives," *IEEE Transactions on Pattern Analysis and Machine Intelligence*, vol. 13, pp. 611, 1991.
- [NIK91b] S. K. Nayar, K. Ikeuchi, and T. Kanade, "Shape from interreflections," *International Journal of Computer Vision*, vol. 6, no. 3, pp. 173–195, Aug. 1991.
- [NFB97] S. K. Nayar, X.-S. Fang, and T. Boult, "Separation of Reflection Components Using Color and Polarization," *International Journal of Computer Vision*, vol. 21, no. 3, pp. 163–186, 1997.
- [Nic65] F. E. Nicodemus, "Directional reflectance and emissivity of an opaque surface," *Applied Optics*, vol. 4, pp. 767–773, 1965.
- [Nic70] F. E. Nicodemus, "Reflectance nomenclature and directional reflectance and emissivity," *Applied Optics*, vol. 9, pp. 1474–1475, 1970.
- [NN96] A. Nikolaev and S. K. Nayar, "Transparent grippers: seeing while grasping," in *Proceedings of Image Understanding Workshop*, pp. 1333–1338, Palm Springs, Feb. 1996.
- [OMOT03] K. Ohara, M. Mizukawa, K. Ohba, and K. Taki, "3D modeling of micro transparent object with integrated vision," in *Proceedings of IEEE Conference on Multisensor Fusion and Integration for Intelligent Systems*, pp. 107–112, Tokyo, Japan, July–Aug. 2003.
- [Opt] OptiCAD, <http://www.opticad.com/>.
- [ON97] M. Oren and S. K. Nayar, "A Theory of Specular Surface Geometry," *International Journal of Computer Vision*, vol. 24, no. 2, pp. 105–124, Sep. 1997.
- [OJR03] M. Osadchy, D. Jacobs, and R. Ramamoorthi, "Using specularities for recognition," in *Proceedings of IEEE International Conference on Computer Vision*, pp. 1512–1519, Nice, France, Oct. 2003.

- [PK04] J. Park and A. C. Kak, "Multi-peak range imaging for accurate 3d reconstruction of specular objects," in *Proceedings of Asian Conference on Computer Vision*, pp. 764–769, Jeju Island, Korea, Jan. 2004.
- [PD03] P. Peers and P. Dutré, "Wavelet environment matting," in *Proceedings of Eurographics Workshop on Rendering*, pp. 157–166, Leuven, Belgium, June 2003.
- [PTVF92] W. H. Press, S. A. Teukolsky, W. T. Vetterling, and B. P. Flannery, *Numerical recipes in C: the art of scientific computing*, Cambridge University Press, Cambridge, England, 1992.
- [Rah99] S. Rahmann, "Inferring 3D Scene Structure from a Single Polarization Image," in *SPIE Proceedings of Conference on Polarization and Color Techniques in Industrial Inspection*, vol. 3826, pp. 22–33, Munich, Germany, June 1999.
- [Rah00] S. Rahmann, "Polarization images: a geometric interpretation of shape analysis," in *Proceedings of International Conference on Pattern Recognition*, pp. 542–546, 2000.
- [RC01] S. Rahmann and N. Canterakis, "Reconstruction of specular surfaces using polarization imaging," in *Proceedings of IEEE Conference on Computer Vision and Pattern Recognition*, pp. 149–155, Kauai Marriott, Hawaii, Dec. 2001.
- [Rah03] S. Rahmann, "Reconstruction of quadrics from two polarization views," in *Iberian Conference on Pattern Recognition and Image Analysis*, pp. 810–820, Mallorca, Spain, June 2003.
- [SSIK99] M. Saito, Y. Sato, K. Ikeuchi, and H. Kashiwagi, "Measurement of surface orientations of transparent objects by use of polarization in highlight," *Journal of Optical Society of America, A*, vol. 16, no. 9, pp. 2286–2293, Sep. 1999.
- [SWN88] A. C. Sanderson, L. E. Weiss, and S. K. Nayar, "Structured Highlight Inspection of Specular Surfaces," *IEEE Transactions on Pattern Analysis and Machine Intelligence*, vol. 10, no. 1, pp. 44–55, Jan. 1988.
- [San65] O. Sandus, "A review of emission polarization," *Applied Optics*, vol. 4, no. 12, pp. 1634–1642, 1965.
- [SNI90] H. Sato, S. K. Nayar, and K. Ikeuchi, "Implementation and Evaluation of a Three-Dimensional Photometric Sampler," in *CMU-RI-TR*, 1990.

- [SOSI03] I. Sato, T. Okabe, Y. Sato, and K. Ikeuchi, "Appearance sampling for obtaining a set of basis images for variable illumination," in *Proceedings of IEEE International Conference on Computer Vision*, pp. 800–807, Nice, France, Oct. 2003.
- [SI94] Y. Sato and K. Ikeuchi, "Temporal-Color Space Analysis of Reflection," *Journal of Optical Society of America, A*, vol. 11, no. 11, pp. 2990–3002, Nov. 1994.
- [SWI97] Y. Sato, M. D. Wheeler, and K. Ikeuchi, "Object shape and reflectance modeling from observation," in *Proceedings of ACM SIGGRAPH 97*, pp. 379–387, 1997.
- [SSK00] Y. Y. Schechner, J. Shamir, and N. Kiryati, "Polarization and statistical analysis of scenes containing a semireflector," *Journal of Optical Society of America, A*, vol. 17, no. 2, pp. 276–284, Feb. 2000.
- [SKB00] Y. Y. Schechner, N. Kiryati, and R. Basri, "Separation of transparent layers using focus," *International Journal of Computer Vision*, vol. 39, no. 1, pp. 25–39, Aug. 2000.
- [SNN03] Y. Y. Schechner, S. G. Narashimhan, and S. K. Nayar, "Polarization-based vision through haze," *Applied Optics*, vol. 42, no. 3, pp. 511–525, Jan. 2003.
- [Sch79] F. Schneider, *Sugar Analysis-ICUMSA Methods*, International Commission for Uniform Methods of Sugar Analysis, 1979.
- [SAP94] J. F. Shackelford, W. Alexander, and J. S. Park, *CRC Materials Science and Engineering Handbook*, p. 883. Boca Raton, Fla.: CRC Press, 1994.
- [Sha85] S. Shafer, "Using color to separate reflection components," *COLOR Research and Application*, vol. 10, pp. 210, 1985.
- [Shu62] W. A. Shurcliff, *Polarized light: production and use*, Harvard University Press, Cambridge, Mass., 1962.
- [SB96] A. R. Smith and J. F. Blinn, "Blue screen matting," in *Proceedings of ACM SIGGRAPH 96*, pp. 259–268, New Orleans, Louisiana USA, Aug. 1996.
- [SRS] SR Sampler, <http://td21.jp/>.
- [SG98] R. Szeliski and P. Golland, "Stereo matching with transparency and matting," in *Proceedings of IEEE International Conference on Computer Vision*, pp. 517–526, Bombay, India, Jan. 1998.

- [SAA00] R. Szeliski, S. Avidan, and P. Anandan, "Layer extraction from multiple images containing reflections and transparency," in *Proceedings of IEEE Conference on Computer Vision and Pattern Recognition*, pp. 246–253, Hilton Head Island, South Carolina, June 2000.
- [Tak02] T. Takahashi, "Creating Photorealistic Virtual Model with Polarization Based Vision System," *Master Thesis*, The University of Tokyo, Feb. 2002.
- [TS67] K. E. Torrance and E. M. Sparrow, "Theory for off-specular reflection from roughened surfaces," *Journal of Optical Society of America*, vol. 57, no. 9, pp. 1105–1114, 1967.
- [TOS+03] N. Tsumura, N. Ojima, K. Sato, M. Shiraishi, H. Shimizu, H. Nabeshima, S. Akazaki, K. Hori, and Y. Miyake, "Image-Based Skin Color and Texture Analysis/Synthesis by Extracting Hemoglobin and Melanin Information in the Skin," *ACM Transactions on Graphics (Proceedings of ACM SIGGRAPH 2003)*, vol. 22, no. 3, pp. 770–779, (San Diego, California USA), July 2003.
- [UG04] S. Umeyama and G. Godin, "Separation of Diffuse and Specular Components of Surface Reflection by Use of Polarization and Statistical Analysis of Images," *IEEE Transactions on Pattern Analysis and Machine Intelligence*, vol. 26, no. 5, May 2004.
- [WUM97] T. Wada, H. Ukida, and T. Matsuyama, "Shape from shading with interreflections under a proximal light source: distortion-free copying of an unfolded book," *International Journal of Computer Vision*, vol. 24, no. 2, pp. 125–135, Sep. 1997.
- [WLTC99] A. M. Wallace, B. Liang, E. Trucco, and J. Clark, "Improving Depth Image Acquisition Using Polarized Light," *International Journal of Computer Vision*, vol. 32, no. 2, pp. 87–109, Sep. 1999.
- [WFZ02] Y. Wexler, A. W. Fitzgibbon, and A. Zisserman, "Image-based environment matting," in *Proceedings of Eurographics Workshop on Rendering*, pp. 279–290, Pisa, Italy, June 2002.
- [Wol90] L. B. Wolff, "Polarization-based material classification from specular reflection," *IEEE Transactions on Pattern Analysis and Machine Intelligence*, vol. 12, no. 11, pp. 1059–1071, Nov. 1990.
- [WK90] L. B. Wolff and D. J. Kurlander, "Ray tracing with polarization parameters," *IEEE Computer Graphics and Applications*, vol. 10, no. 6, pp. 44–55, Nov. 1990.

- [WB91] L. B. Wolff and T. E. Boulton, "Constraining object features using a polarization reflectance model," *IEEE Transactions on Pattern Analysis and Machine Intelligence*, vol. 13, no. 7, pp. 635–657, July 1991.
- [WMPA97] L. B. Wolff, T. A. Mancini, P. Pouliquen, and A. G. Andreou, "Liquid Crystal Polarization Camera," *IEEE Transactions on Robotics and Automations*, vol. 13, no. 2, pp. 195–203, 1997.
- [WLT98] L. B. Wolff, A. Lundberg, and R. Tang, "Image understanding from thermal emission polarization," in *Proceedings of IEEE Conference on Computer Vision and Pattern Recognition*, pp. 625–631, 1998.
- [Yam04] S. Yamazaki, "Photo-realistic rendering of real-world objects based on insufficient measurement," *Ph.D. Thesis*, The University of Tokyo, Mar. 2004.
- [YZOS97] J. Yang, D. Zhang, N. Ohnishi, and N. Sugie, "Determining a polyhedral shape using interreflections," in *Proceedings of IEEE Conference on Computer Vision and Pattern Recognition*, pp. 110–115, San Juan, Puerto Rico, June 1997.
- [ZEM] ZEMAX, <http://www.zemax.com/>.
- [ZFA97] J. Y. Zheng, Y. Fukagawa, and N. Abe, "3D Surface Estimation and Model Construction From Specular Motion in Image Sequences," *IEEE Transactions on Pattern Analysis and Machine Intelligence*, vol. 19, no. 5, pp. 513–518, May 1997.
- [ZWCS99] D. E. Zongker, D. M. Warner, B. Curless, and D. H. Salesin, "Environmental matting and compositing," in *Proceedings of ACM SIGGRAPH 99*, pp. 205–214, Los Angeles, California, Aug. 1999.